ABSTRACT

ANDERSON, ALIESHA D. Finite Element Formulation for Self-Writing of Polymer Optical Fiber Sensors. (Under the direction of Professor Kara J. Peters).

This thesis presents a multi-physics finite element model of the self-writing process of photopolymerization in photosensitive gels in order to better predict the self-generation of polymer optical fiber sensors. The finite element model incorporates the electromagnetic, chemical and mechanical physics of this photonic reaction. The output of the model is thus the dynamics of photopolymerization and self-focusing including densification and the induced index of refraction change. An experimentally verifiable benchmark trial of a UV light source focused into UV curable resin was modeled using COMSOL Multiphysics, to develop a basis for calibration of different photosensitive gels. This model was then extrapolated to demonstrate the effects of photopolymerization when a single fiber is focused into an epoxy resin as well as the effects of curing an epoxy-filled gap between two aligned fibers.

Results were obtained for linear and saturation models of the change in the index of refraction. These models are applied to single and two fiber benchmark examples. The saturating effects are consistent with previous experimental research showing a 2% change in refractive index with similar lightwave confinement within the cured portion of the resin. The confinement achieved with this model has also verified the ability to predict self-focusing and tapering effects that are also seen in previous experimental studies. The effect of densification within the sample and how this is affected by the geometric constraints on the system are demonstrated as well. This thesis provides a versatile finite element model for predicting the dynamics of the photopolymerization process for a variety of resins and experimental geometries and has presented an effective tool for use in determining the response of a polymer sensing element cured using the photopolymerization process.

Finite Element Formulation for Self-Writing of Polymer Optical Fiber Sensors

by
Aliesha D. Anderson

A thesis submitted to the Graduate Faculty of
North Carolina State University
in partial fullfillment of the
requirements for the Degree of
Master of Science

Mechanical Engineering

Raleigh, North Carolina

2008

APPROVED BY:

Dr. Mohammed A. Zikry	Dr. Greg D. Buckner

Dr. Kara J. Peters
Chair of Advisory Committee

DEDICATION

I think a hero is an ordinary individual who finds strength to persevere and endure in spite of overwhelming obstacles.

– Christopher Reeve –

This thesis is dedicated to the extraordinary heroes in my life who have given me the strength and support to endure the trials that life continually sends our way.

BIOGRAPHY

Aliesha D. Anderson was born in Northfield, MN to parents Karen and James Anderson. She grew up in Pennock, Minnesota graduating from Willmar Senior High School in 2002. She went to Hamline University in St. Paul, MN for her undergraduate degree majoring in Physics and Forensic Science and minoring in Mathematics. She graduated with her Bachelor's Degree in 2006. She started her graduate career at North Carolina State University in the fall of 2006 pursuing a masters of science in mechanical engineering.

ACKNOWLEDGMENTS

First I would like to thank my advisor, Dr. Kara Peters, for her guidance and support throughout the last two years of research. She has been an incredible help and inspiration for completion of this thesis. I would also like to express my gratitude to Dr. Greg Buckner and Dr. Mohammed Zikry for their knowledge and for serving on my defense committee.

This thesis would not have been possible without the unconditional love and support from my family. I would like to thank my parents for their amazing understanding and encouragement in the pursuit of my graduate degree.

TABLE OF CONTENTS

LIST OF TABLES

LIST OF FIGURES

Chapter 1

Introduction

An important aspect of aircraft design, functionability and safety comes from the information gathered through structural health monitoring (SHM). Numerous sensors can be placed throughout the airframe of the aircraft to measure and test for possible issues and failures at susceptible points within the structure. The field of SHM is continually looking for new, more advanced sensors that are small, unobtrusive, lightweight, and robust enough to survive general wear. In the past, the sensors being used had been primarily electrical until the last couple decades when the idea of using fiber optics was presented as an alternative to purely electrical sensors. The introduction of fiber optic sensors allowed for much greater flexibility in sensing different properties and greater flexibility in placement and design. The development of sensors using fiber optics has not only brought about some of the most non-invasive and lightweight sensors, it has also brought the ability to measure quantities that were previously not feasible. One of the greatest advantages for using fiber optic sensors is their size and the ability to embed such sensors in composites and other materials without decreasing the structural integrity of the system [1].

Within the last few years, there has been a shift in the focus of the fiber optic community from using silica fibers to incorporating the use of polymers as optical fiber sensors. One of the most recent discoveries in novel fiber manufacturing techniques is a process called photopolymerization. This process brought about a wave of research into self-writing waveguides [2, 3, 4, 5, 6, 7]. When a focused beam of light impinges upon a

photo-curable resin, only the region directly in the focus of the beam is cured while the rest of the resin remains liquid. In the curing process, the index of refraction is increased slightly, enough to create an index-guiding relationship between the cured and uncured resin respectively. As this process continues, the light guides itself down this new core region curing as it goes, creating a self-writing waveguide [5, 7]. Photopolymerization has presented a new avenue for developing micrometer-scale optical devices due to the self-writing/self-guiding nature of the curing process.

The mechanisms at work in photopolymerization are still being studied intensely due to the nonlinear nature of the process and the innumerable device and sensor design capabilities. This research seeks to add to the prediction and design capabilities of the photopolymerization process and incorporate the chemical and physical relationships at work within this reaction. The purpose of this work was to develop a finite element model of photopolymerization in a UV-curable epoxy resin. This model takes into account two important factors that occur simultaneously in this process, an increase in the index of refraction of the resin as well as a change in the density of the sample being irradiated [7]. In doing so we have developed a model that incorporates the electromagnetic, chemical and mechanical effects occurring throughout the reaction.

The following chapter presents a review of the literature within the field of photopolymerization, both experimental and theoretical work, as well as the context of this thesis. Chapter 3 discusses the finite element model development including a detailed examination of the electromagnetic aspects of the reaction, how these affect the polymerization process and in turn how the polymerization reaction changes the refractive index and density. We present a theoretical benchmark case that is easily replicable in a laboratory setting to be modeled and extrapolate the basic model to two real world situations. Chapter 4 presents a discussion and the results from the different case studies presented in Chapter 3. Chapter 5 discusses the findings from this research and proposes recommendations for future work.

The simulations presented in this work demonstrate that the finite element method can accurately predict features commonly seen in self-writing waveguides. This new model could be easily extended to design sensors and other micro-optical devices using the pho-

topolymerization fabrication technique.

Chapter 2

Background

2.1 Photopolymerization

Photopolymerization is a process that has been well understood for quite some time, but its uses and applications in fields outside the realm of chemistry have been newly revealed only within the last few decades. This process has been found to have unique properties for many different uses in optical applications. The early research into photopolymerization used a process known as single photon absorption (SPA) to cure a portion of an ultra-violet (UV) curable resin. The resins used are initially made up of monomers and initiator molecules. When the resin is exposed to a UV light source, the initiator molecules in the monomer bath are excited to a higher state by absorbing a single photon from the incident light [8]. In this higher energy state, the monomers can then connect with one another creating polymer chains within the resin material. This polymerization occurs only along the focal path of the light as it travels through the epoxy resin, while the rest of the resin remains uncured. In single photon absorption the light absorbed by the resin is linearly related to the intensity of the light source being introduced [8]. This *process*, however, is nonlinear and creates a permanent effect in curing the irradiated portion of the photosensitive material.

A second photopolymerization process has been discovered more recently, called two photon absorption (TPA). In this process, the initiator molecules in the resin absorb

two photons simultaneously. TPA can only be initiated through high intensity light sources such as femtosecond pulse lasers. Unlike SPA, the light absorbed by TPA is nonlinear in nature and the energy absorbed is proportional to the square of the incoming light intensity [9]. Thus in TPA the energy from the source is only deposited at the very focal *point* of the laser beam [8, 9]. This higher resolution allows for the fabrication of polymer structures from the millimeter scale all the way down to a nanometer-scale precision. The discovery of the TPA process has brought about a new wave of research to utilize this process for writing small scale structures to be used as micro-optical and opto-electrical devices.

2.2 Early Research

There are two groups of study found in the literature that investigate photopolymerization and its uses: experimental studies and theoretical development and modeling. In 1993 Frisken *et al.* [2] published one of the first papers demonstrating how the SPA process can be used experimentally. The purpose of this research was to propose a way to eliminate the use of bulk optics in communication and sensor applications, which are large and cumbersome. The authors were able to create light-induced optical waveguide uptapers (self-writing waveguide with a diameter that is expanding as it is cured). They demonstrated that if one can create an increase in the refractive index of the material greater than 2% through irradiation, it is possible to create a self-writing waveguide. The properties of standard UV-curable epoxies fit well within this requirement. The experiments demonstrated that this process can take anywhere from several seconds to several hours depending on the setup and thickness of the sample. Temperature testing was also performed and it was found that the fabricated waveguides remained stable and could withstand temperatures up to 150°C without side effects. At temperatures above 150°C the uptapers became discolored and finally at temperatures greater than 200°C failure occurred [2].

Another group studying the evolution of self-writing waveguides and the increase in the index of refraction in photosensitive resins was Kewitsch and Yariv [3]. Their paper focused on understanding the reaction process better and wherein the dependencies

of this interaction lie. It was found that the change in the index of refraction was not instantaneous, instead it was dependent on the optical electric field interactions throughout the curing process with respect to time. The authors suggested that a new form of the nonlinear wave equation could account for these changes and predict the self-guided and time-dependent properties of this reaction [3].

Kewitsch and Yariv determined that there are three stages to the self-writing process. In the first stage, small polymerized elements are created causing very small changes in the bulk index and density. This stage is dependent on the amount of oxygen present in the sample which determines the threshold intensity before curing begins. In the second stage of this reaction, larger polymer chains are created and there is enough energy to allow for cross-linking of these chains. This part of the reaction takes place very quickly in comparison to stage one. The third and final stage is the point of saturation for the photosensitive resin. The available monomer molecules within the focal region are dramatically decreased due to the earlier part of the reaction which slows the process, bringing it to completion or full cure [3]. Figure 2.1 shows the self-writing waveguide growth demonstrated by Kewitsch and Yariv for time $t = 0$ to $t = 30s$. The leftmost picture shows the beam profile within the resin at time $t = 0$. As time continues from left to right, it can be seen that the beam waist moves closer to the input plane while the polymerization continues. This effect is indicative of the self-focusing nature of this reaction.

One of the issues with early waveguides fabricated through photopolymerization is that many were not uniform throughout the length of the growth [2, 3, 10]. To create a more uniform waveguide, Kagami *et al.* [5] grew a self-writing waveguide using a graded index multimode fiber (GI-MMF) to guide the incident light source into the resin. For a graded index fiber, the index of refraction of the core is highest along the propagation axis at the center of the core and decreases out radially towards the core-cladding boundary. This index distribution minimizes the differences in propagation rates for different wavelengths, thus reducing modal dispersion. Kagami *et al.* were thus able to symmetrically expose the resin creating uniformly cured sections with a completely homogeneous polymer core. Figure 2.2 shows a typical example of these waveguides with a uniform diameter along the

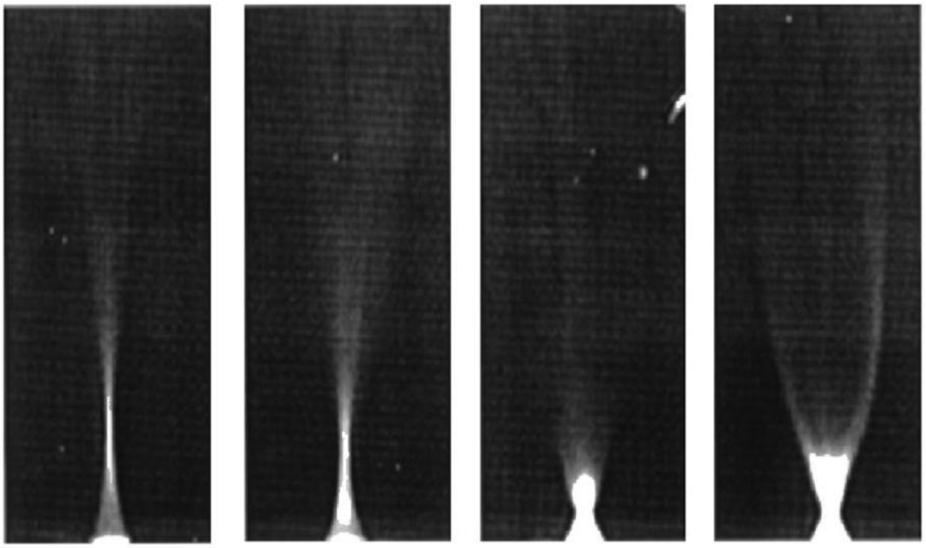

Figure 2.1: Photograph of self-writing waveguide growth from time $t = 0$ to $t = 30s$ [3].

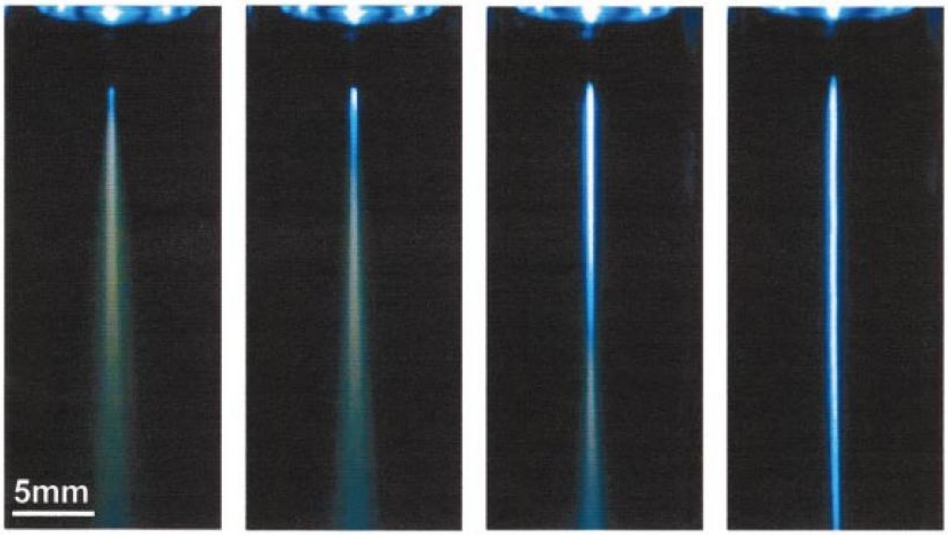

Figure 2.2: Time-step process of writing a uniform self-writing waveguide [5]. Images read from left to right, with GI-MMF fiber seen at the top of each subfigure.

length. In the first section of the figure, the light can be seen dispersing slightly in the material, while the early portion of the resin directly in the light path is cured. As time passes, the light progressively cures more of the resin and a cured channel is formed within the resin which allows the light to self-propagate along its own cured path, creating a self-writing waveguide. The second part of [5] demonstrated the ability to use this type of setup to create self-writing uniform waveguides at an angle of 45 degrees within a photosensitive resin, as shown in figure 2.3.

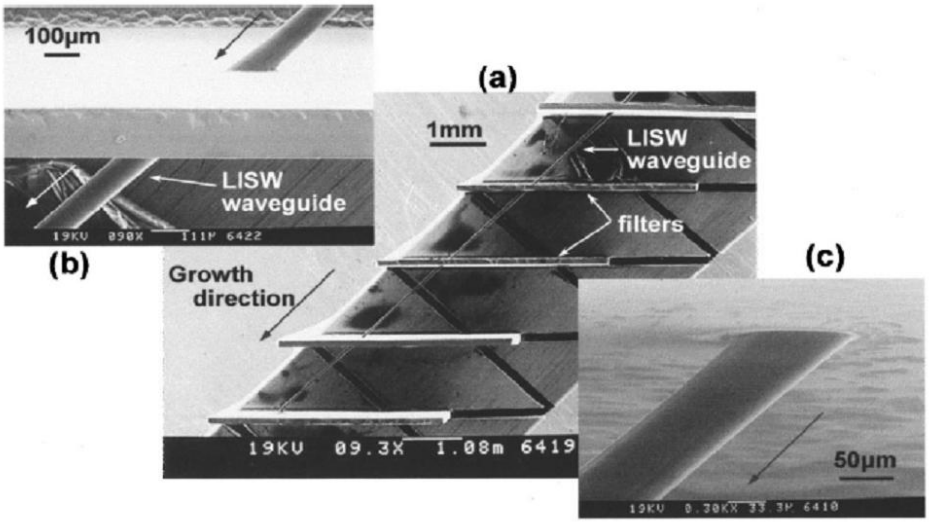

Figure 2.3: (a)Self-writing waveguide grown at an angle of 45 degrees using photo filters, (b) shows the uniformity in passing through a photo filter and (c) shows close up of fiber growth after passing through the filter [5].

Much of the focus of this early research was to experimentally demonstrate the self-writing capabilities of photopolymerizable resins. However, not much quantitative data has been produced on the optical and chemical properties of the photopolymerizable materials themselves and their relationship to the final constructed micro-structure. An important paper in the field addressing these topics is Dorkenoo *et al.*[7], which demonstrated the two competing properties that affect the optical thickness of a polymer. The optical thickness of a material is defined as $\delta = nd$, where n is the refractive index and d is the sample thickness. During the photopolymerization process, the index of refraction is

increased by approximately 2%, while simultaneously the sample thickness is decreased by 4% [7]. Since these two properties are changing on the same order of magnitude, neither property can be neglected when predicting the interactions involved in this process. The authors also proposed a differential rate equation which accounts for both of these changing properties by relating them to the polymer concentration within the resin sample. The derivation of this equation will be discussed in greater detail in section 2.4.

2.3 High Resolution Photopolymerization

As of 1997, the physics of the photopolymerization process were still unknown, but the potential of this process continued to intrigue researchers. Maruo *et al.* then introduced the use of two photon absorption (TPA) to write structures in UV-curable resins [9]. Since the spatial density of photons is very high at the focal point of the light source, it causes a chain reaction within the material creating polymer elements at specified points in the resin. The speed of this reaction is proportional to the square of the photon density at each point in the resin [9]. Unlike the single photon process, whose precision is hindered by the attenuation in the laser beam and the distorted wavefront, TPA allows for much higher precision and higher resolution. Figure 2.4 shows a spiral structure created by Maruo *et al.* using the TPA process. This seminal paper triggered a series of studies by various researchers to fabricate increasingly complex micro-structures through TPA. Figure 2.5 show a sample of some of these three-dimensional structures.

One of the disadvantages of using TPA is that it is a more complicated process than SPA and as such is more expensive to use. It requires the use of a femtosecond laser and a more complex experimental setup than single photon absorption. The single photon absorption process is thus a better choice for a much simpler and cost-effective setup for self-writing waveguide applications where intricate 3D structures are not needed.

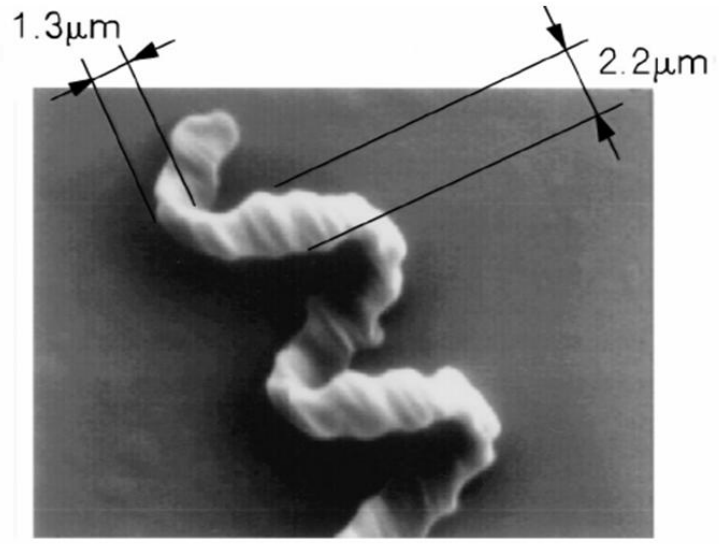

Figure 2.4: Three-dimensional spiral structure created using TPA in photo sensitive resin [9].

(a) Movable micro-gear [11].

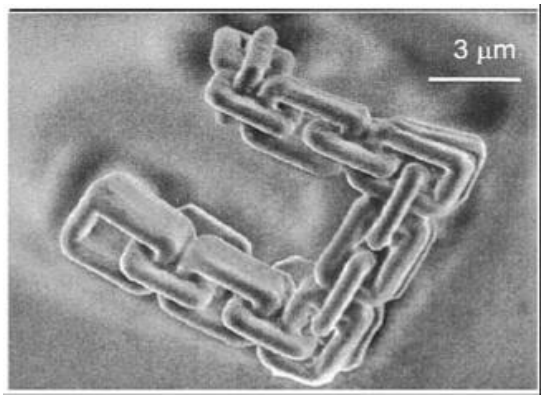

(b) Micro-chain [12].

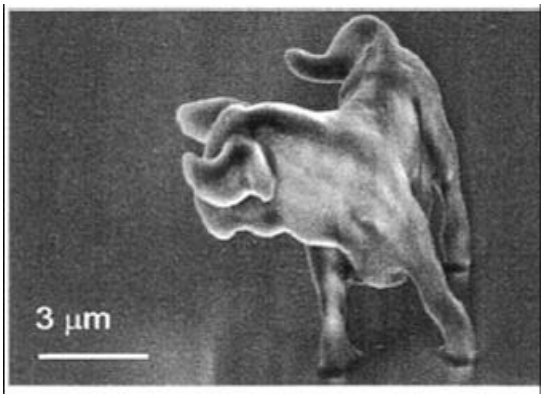

(c) Micro-bull [12].

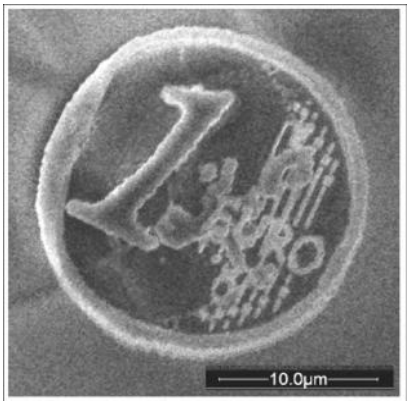

(d) Euro coin replication [13].

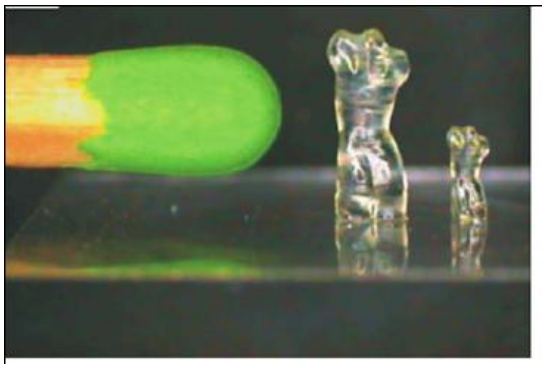

(e) Venus statue on mm and μm scale compared to the tip of a matchstick [14].

Figure 2.5: The above figures demonstrate the versatility of the TPA process in creating 3D structures.

2.4 Theoretical Modeling

In the first theoretical modeling of self-focusing through photopolymerization, Monro *et al.* [15] derived a two-dimensional theory using modal decomposition along with the beam propagation method to describe the interactions between the incident light and the response of the UV-curable epoxy. In a second paper, Monro *et al.* [16] extrapolated the first approach to three-dimensional geometries using a series expansion technique. These two techniques account for the reactions seen with both single and two photon absorption. After the early works of Monro *et al.*, more emphasis was placed on numerical modeling and simulation of the photopolymerization and self-writing processes. For example, a series of three papers looked at writing a polymer micro-tip on the end of silica fibers [10, 17, 18]. Beginning with an empirical approach, this set of studies built up experimental research on tip growth and then developed a model based on the beam propagation method in two [10] and three dimensions [17, 18]. These studies also looked at the effects of oxygen on the photopolymerization process and found that higher concentrations of oxygen hindered the reaction and either caused a delay in polymerization or did not allow the reaction to initiate if the concentration was too high. The authors proposed that the role of the oxygen level may account for some differences in the theoretical predictions and experimental measurements.

To model the process of self-focusing of lightwaves through photopolymerization, some researchers have focused on the physics aspects of the interactions [15, 16, 6], while others have focused on the chemical interactions [7]. As both of these aspects are important to predict this process, it is necessary to look at how these two groups of study work together to fully define this process.

Monro *et al.* [15, 16] described the propagation of light in a photopolymerizable resin using the paraxial wave equation approximation,

$$ik_0 n_0 \frac{dE}{dz} + \frac{1}{2}\Delta_t E + k_0^2 n_0 \Delta n E + \frac{i}{2} k_0 n_0 \alpha E = 0. \tag{2.1}$$

The constant k_0 is the free space wave number, n_0 is the initial index of refraction, $\Delta n(x, y, z, t) = n - n_0$ where n is the current refractive index, α is the attenuation co-

efficient and $E(x, y, z, t)$ is the electric field envelope amplitude. For a planar lightwave $E(x, y, z, t)$ can be expressed as,

$$E(x, y, z, t) = E_0(x, y)e^{i(k_0 z - \omega t)}. \tag{2.2}$$

To describe the photopolymerization, Monro *et al.* [15] applied a phenomenological model of the form,

$$\frac{\partial \Delta n}{\partial t} = A(EE^*)^p(1 - \frac{\Delta n}{\Delta n_s}). \tag{2.3}$$

where Δn_s is the fixed saturation value for the index of refraction change, p defines the photon absorption process ($p = 1$ for single photon absorption and $p = 2$ for two photon absorption) and A is a coefficient that is dependent on the material properties such as the wavelength and the number of photons (p). Monro *et al.* then expanded equation (2.1) as a modal series to solve numerically.

On the other hand, Dorkenoo *et al.* focused on incorporating the chemistry of photopolymerization to describe this process. For an uncured resin, at time $t = 0$, it is a liquid bath of monomers at which point there are no polymers within the sample. As time progresses, the monomers are excited and combine to create polymer chains in the focal region of the light source. The concentration of polymers within the sample is defined as $(P(t))$ where the initial polymer concentration can then be defined as $P(0) = 0$. The other necessary material chemical properties are the molar concentration $(M(t))$, the volume of the sample $(V(t))$, and the concentration of dye or initiator molecules $(A(t))$, all of which are changing with respect to time. All of the above quantities must satisfy the conservation laws [7],

$$[M(t) + qP(t)]V(t) = M(0)V(0) = [M(\infty) + qP(\infty)]V(\infty) \tag{2.4}$$

$$[A(t) + P(t)]V(t) = A(0)V(0) = [A(\infty) + P(\infty)]V(\infty). \tag{2.5}$$

In order to properly define the two simultaneous changes in the index of refraction and the thickness of the material, an equation for a common variable affecting both needs to be determined. It was found that the concentration of polymers $(P(t))$ within the resin

can be directly related to both of these properties [7]. We now present the derivation of the differential equation with respect to $(P(t))$ from Dorkenoo *et al.* [7].

First we define the relationship $\tilde{P}(t) = P(t)/P(\infty)$, where $\tilde{P}(t)$ is the normalized polymer concentration. From experimental data, it is apparent that there is a decrease in the normalized sample thickness, $\tilde{d}(t)$,

$$\tilde{d}(t) = \frac{d(t)}{d(0)} = [1 + \kappa\tilde{P}(t)]^{-\frac{1}{3}}. \tag{2.6}$$

The constant κ is thus defined in terms of the thickness $d(t)$ as $\kappa = vP(\infty) = d^3(0)/d^3(\infty) - 1$. The equation for the concentration of the initiator molecule is defined as,

$$\frac{d}{dt}A(t) = -\frac{\phi I}{d(t)}[1 - e^{-\epsilon d(t)A(t)}] \tag{2.7}$$

where $\phi(\lambda)$ is the quantum yield, which measures the probability that this molecule will react after the single photon absorption, $\epsilon(\lambda)$ is the molar absorption coefficient and I is the intensity of the incident light. Solving equation (2.6) for $d(t)$ and substituting into equation (2.7) we obtain,

$$\frac{d}{dt}A(t) = -\frac{\phi I}{d(0)[1 + \kappa\tilde{P}(t)]^{-\frac{1}{3}}}[1 - e^{-\epsilon d(0)[1+\kappa\tilde{P}(t)]^{-\frac{1}{3}}A(t)}]. \tag{2.8}$$

A quick simplification gives,

$$\frac{d}{dt}A(t) = -\frac{\phi I}{d(0)}[1 + \kappa\tilde{P}(t)]^{\frac{1}{3}}[1 - e^{-\epsilon d(0)[1+\kappa\tilde{P}(t)]^{-\frac{1}{3}}A(t)}]. \tag{2.9}$$

Similar to the definition for $\tilde{P}(t)$, we normalize $\tilde{A}(t) = A(t)/A(0)$ and relate $\tilde{A}(t)$ to $\tilde{P}(t)$, $\tilde{A}(t) = 1 - \tilde{P}(t)$. Substituting this into equation (2.9) we obtain,

$$\frac{d}{dt}(1 - \tilde{P})A(0) = -\frac{\phi I}{d(0)}[1 + \kappa\tilde{P}(t)]^{\frac{1}{3}}[1 - e^{-\epsilon d(0)A(0)[1+\kappa\tilde{P}(t)]^{-\frac{1}{3}}(1-\tilde{P}(t))}]. \tag{2.10}$$

Finally, by solving equation (2.10) for $d\tilde{P}/dt$,

$$\frac{d}{dt}\tilde{P} = \frac{\phi I}{d(0)A(0)}[1 + \kappa\tilde{P}(t)]^{\frac{1}{3}}[1 - e^{-\epsilon d(0)A(0)[1+\kappa\tilde{P}(t)]^{-\frac{1}{3}}(1-\tilde{P}(t))}]. \tag{2.11}$$

Defining $\gamma = \phi I/d(0)A(0)$ and $\zeta = \epsilon d(0)A(0)$, equation (2.11) simplifies to the final polymerization concentration derived by Dorkenoo *et al.* [7],

$$\frac{d}{dt}\tilde{P} = \gamma[1 + \kappa\tilde{P}(t)]^{\frac{1}{3}}[1 - e^{-\zeta[1+\kappa\tilde{P}(t)]^{-\frac{1}{3}}(1-\tilde{P}(t))}]. \tag{2.12}$$

Equation (2.12) thus defines a rate equation for the concentration of polymers created in the resin through the photopolymerization process. Similarly, this equation can be used to describe the changes that are occurring to the refractive index and the thickness of the material by relating them to the polymer concentration $P(t)$.

2.5 Sensor Applications

One of the most recent applications of photopolymerization fabrication is that of micro-sensors. There are a number of commercially available epoxy resins that can be tailored to specific applications, allowing for extreme versatility. One of the first sensor demonstrations was fabricated and implemented by Lin *et al.* [19]. Using the two-photon polymerization process, Lin *et al.* wrote a 3D micro-fluid sensor which measured the velocity of fluid passing by the sensor, which is controlled by optical tweezers. Figure 2.6 shows a picture of the flag-shaped sensor for use in bio-sensing applications.

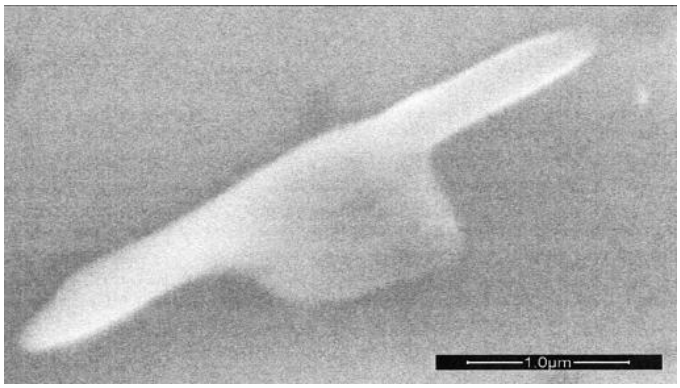

Figure 2.6: Micro-fluid sensor for velocity measurements [19].

A more recent sensor design, applicable to structural health monitoring appli-

cations, was developed by Huang [20]. Huang grew a polymer sensing element between two multimode silica fibers for use as an intensity-based strain sensor. This particular fabrication technique was demonstrated in a paper by Dorkenoo *et al.* [6], where it was shown that a polymer element could be cured between two fibers with the correct amount of lightwave input power, as shown in figure 2.7. It was demonstrated that coherent and

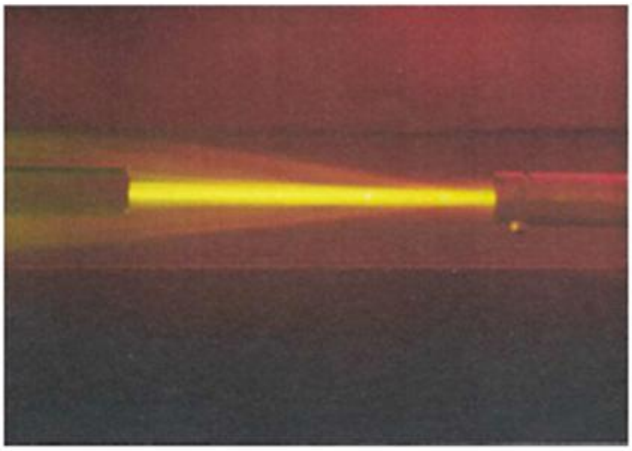

Figure 2.7: Cured resin between two silica fibers [6].

non-chaotic waveguide formation can be created at low input powers, up to approximately $8\mu W$, though periodic behavior was seen at powers close to the upper bound [6]. Extrapolating from this previous work, Huang grew the polymer element as seen in figure 2.8. The strain sensor works on the principle that the intensity of the propagated light changes with elongation of the polymer waveguide. The sensor was able to sustain up to a 5% strain before failure at the silica/polymer interface. Huang speculated that by creating a stronger bond at the silica/polymer interface the possible strain measurement could be increased to a much greater percentage.

It can be seen that there are a number of promising applications for utilizing the photopolymerization process in many different fields. One of the most exciting applications is the use of this process for the fabrication of new sensors for structural health monitoring, since the fabrication of such sensors is relatively simple and cost-effective.

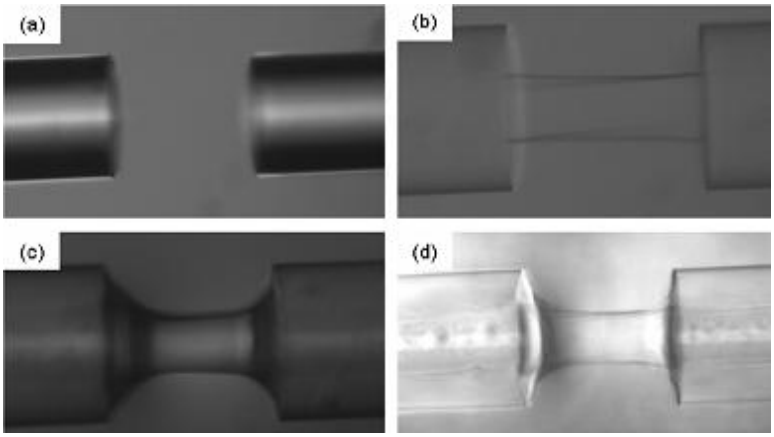

Figure 2.8: Growth of polymer sensing element using photopolymerization, (a) alignment of fibers, (b) initial growth of the polymer sensing element (c) polymer element, (d) final sensor element with cladding [20].

2.6 Goals of this work

The purpose of this research is to develop a finite element model that takes into account the two competing factors that define the optical properties within a photo-sensitive resin: the change in index of refraction and the change in the density of the material, as defined by [7]. This model should analytically reproduce previous experimental research and provide a versatile foundation for the calibration of photo-sensitive resin with variable input parameters. Finally, the model would allow extrapolation to predict outcomes for more complicated input conditions. In this study, the model is developed in a commercially available code, COMSOL Multiphysics, allowing for easy accessibility for researchers to utilize the code.

The following chapter will present the theory behind the model development based on the optical, chemical and mechanical processes. Chapter 4 will present the simulation results, their comparison with previous experimental data and an extrapolation of the original model to demonstrate the curing process of a polymer sensing element between two silica fibers similar to the sensor developed by [20]. Finally, Chapter 5 will summarize the results and propose future directions for the model.

Chapter 3

Numerical Modeling

To compute the opto-mechanical interactions within a resin undergoing photopolymerization, an epoxy resin bath made of a UV-curable epoxy was modeled using COMSOL Multiphysics, taking into account the properties of photopolymerization as described in the previous chapter. This model will predict the dynamic interactions between the incident lightwave and the reacting resin bath through a time-dependent model based on the polymer concentration ordinary differential equation (ODE) of equation (2.12). This chapter presents the analytical basis for this model, as well as its implementation in the finite element environment. The specific goal of this chapter is to develop a versatile COMSOL model of a benchmark experiment that is easily replicable in a lab setting and allows for calibration of the photopolymerization process for a specific resin. The results of this model will be presented in the following chapter.

The the paper by Dorkenoo *et al.* [7], a double interferometer configuration was applied to measure the dynamics of the photopolymerization process as a function of time. The uncured resin and a reference drop of pre-cured sol-gel polymer were simultaneously illuminated with UV and visible light to independently measure the index and thickness of the exposed resin over time. This experiment provides an accurate characterization of the photopolymerization process, however it is expensive and complex to recreate. The COMSOL model generated in this thesis provides an alternative method to calibrate the parameters of the photopolymerization process without the need for a separate, complex

interferometer system.

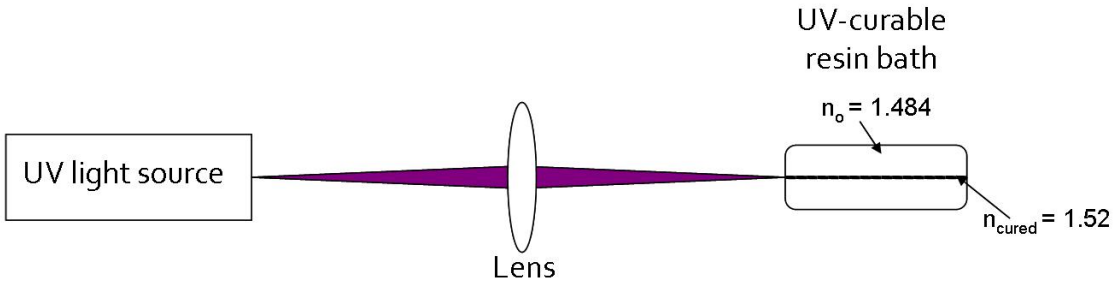

Figure 3.1: Experimental benchmark case for model definition

Figure 3.1 depicts the benchmark experiment to be modeled, where an ultra-violet light source is focused into a UV-curable epoxy resin. As the resin is exposed, the portion directly in the focal region of the beam is cured increasing the local refractive index and density of the resin [7]. In the COMSOL model, only the UV-curable resin bath will be modeled. The dynamics of the photopolymerization process (i.e. the rate of refractive index and density change as a function of polymerization state and input intensity) could then be fit to match easily measurable parameters such as: the time required to grow the waveguide a fixed distance, the final width of the waveguide, and the taper angle.

There are a number of input parameters that are considered known for the experiment of figure 3.1. These include the initial values of the index of refraction (n_0) and density (ρ_0) for the uncured polymer resin and their saturation values for the fully cured polymer. Other known input values are the wavelength and power output of the laser source. From these values, the wave number (k_0), Gaussian waist (w_0) and the peak electric field values can be calculated.

The basic computational outline for the finite element model is shown in figure 3.2. The initial conditions are a uniform resin bath with uniform refractive index $n(r, \theta, z, 0) = n_0$ and concentration of polymers $\tilde{P}(r, \theta, z, 0) = 0$. For each time step, the electric ($\mathbf{E}$) and magnetic ($\mathbf{H}$) fields are computed and from these the power flow (S_z) is determined. The intensity from the light source, I_z, (which is linearly related to the power flow) is the driving

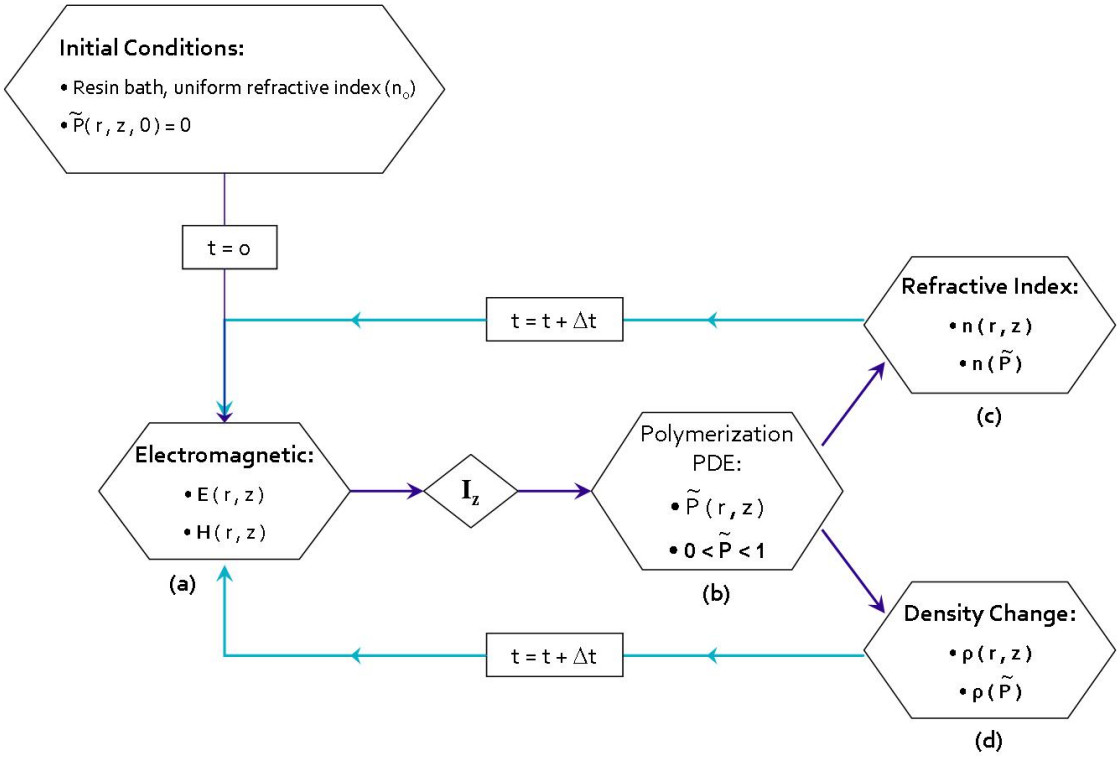

Figure 3.2: Outline of modeling process. (a) Electro-magnetic properties discussed in section 3.1, (b) Polymerization properties detailed in section 3.2, (c) Refractive Index formulation discussed in section 3.3 and (d) Change in density discussed in section 3.4

force for the polymerization reaction and excites the monomers in the resin allowing them to polymerize. The change in polymerization state $\Delta\tilde{P}(r, \theta, z, t)$ for the time interval Δt is calculated based on the polymerization rate equation of equation (2.11). The index of refraction and the density are then updated based on $\tilde{P}(r, z, t)$ and the process is continued for each subsequent time step.

Given the input parameters described above, the model will calculate the index of refraction $n(r, \theta, z, t)$ for the material and the material thickness $d(r, \theta, z, t)$ as a function of time. The model can also output other important properties such as intensity, energy, and electric field properties at each time step and show the mechanical deformation in the

resin due to the density change.

It is important to note that this model combines three different physical mechanisms: electromagnetics (optics), chemistry (polymerization rate equation) and the mechanical changes in the resin (density). These reactions occur on very different time scales which posed a significant challenge in modeling this process. The electromagnetic propagation occurs on a time scale of femto- to pico-seconds, whereas the polymerization of the resin is on the order of seconds to minutes, sometimes up to hours to fully cure depending on the sample size [2]. The specifics of the solution to this problem will be discussed in detail in section 3.1.

Finally, in this model, we consider a uniform resin bath with an incident plane Gaussian wave. This process can thus be modeled as an axisymmetric problem assuming rotational symmetry (θ). The model of the epoxy resin bath is reduced to a rectangular cross-section where the width is the radial coordinate (r) from 0 to $6\mu m$ and the length of the rectangle is the z-coordinate from 0 to 20μm, as shown in figure 3.3. The following sections present the details of each of the steps outlined in figure 3.2.

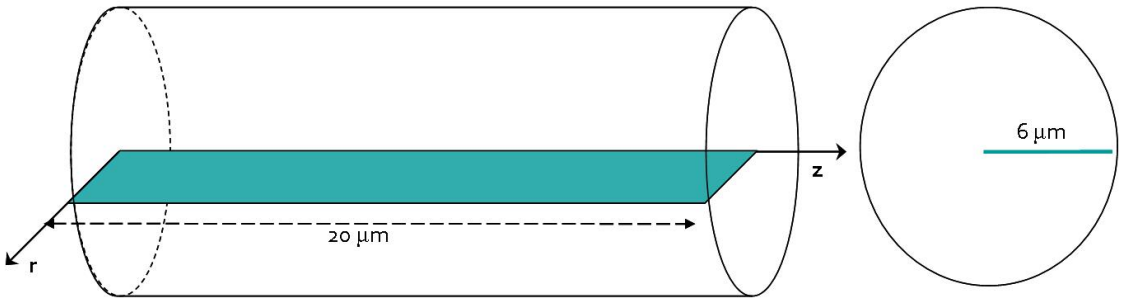

Figure 3.3: Model simplification assuming rotational symmetry

3.1 Electromagnetics

The UV lightwave is incident at the $z = 0$ boundary and is defined in cylindrical coordinates with a Gaussian distribution such that,

$$E(r,z,t) = E_0\, exp[-r^2/w_0^2]\, Cos(\omega t - k_0 z) \tag{3.1}$$

and

$$H(r,z,t) = H_0\, exp[-r^2/w_0^2]\, Cos(\omega t - k_0 z) \tag{3.2}$$

where E_0 is perpendicular to H_0 and the wave is propagating along the z-axis. Figure 3.4 depicts the rectangular cross-section being used for modeling purposes, where each of the boundaries is labeled as $b1$ through $b4$. In order to properly define the system, each

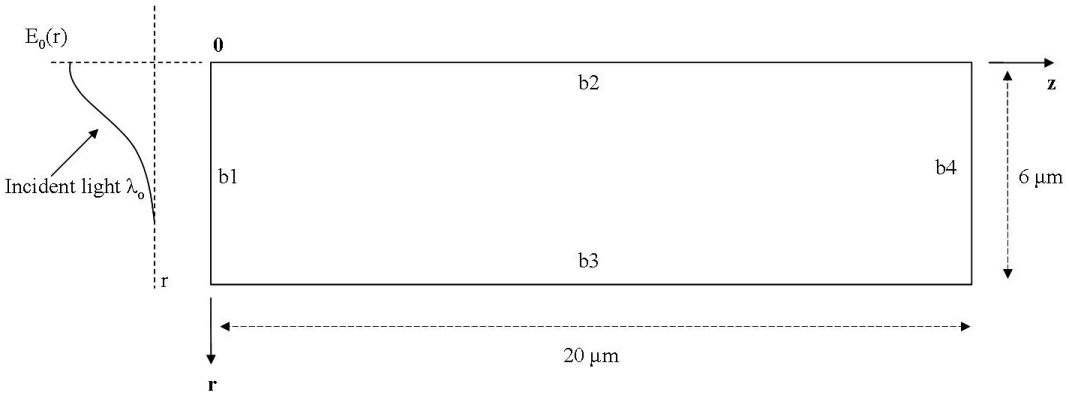

Figure 3.4: Diagram of model setup.

of the boundaries must be defined by their input electromagnetic properties. The applied boundary definitions for $b1$ through $b4$ are given in table 3.1. The choice of perfect electric and perfect magnetic conditions on boundaries $b2$ and $b3$ enforce the rotational symmetry of the model.

In this case we are computing the electric and magnetic fields. Since this is not a weakly guiding problem, we will need to solve for both fields. From Maxwell's equations, we have the following wave equations for propagation through a medium,

$$\nabla \times \mathbf{E} = -\mu_0 \frac{\partial \mathbf{H}}{\partial t} \tag{3.3}$$

Table 3.1: Boundary Conditions

Boundary Number	**Boundary Condition**	**Expression**
b1	Scattering	equation (3.1) at z = 0
b2	Perfect Electric	–
b3	Perfect Magnetic	–
b4	Scattering	0

$$\nabla \times \mathbf{H} = -\epsilon_0 \, n(r, \theta, z, t)^2 \, \frac{\partial \mathbf{E}}{\partial t} \tag{3.4}$$

where μ_0 is the permeability of a vacuum ($\mu_0 = 4\pi$x10^{-7}(H/m)) and ϵ_0 is the permittivity of a vacuum ($\epsilon_0 = 8.854$x10^{-12}(F/m)). For this problem, n is spatially varying, therefore the electric and magnetic waves cannot be decoupled.

The power flow of the incident light is defined as the Poynting vector **S**, which is the cross product of the electric and magnetic fields,

$$\mathbf{S} = \mathbf{E} \times \mathbf{H}. \tag{3.5}$$

The power flow in the direction of propagation is the z component of **S**, S_z. From the power flow we can calculate the intensity, which is defined as the average energy through a unit area perpendicular to the propagation direction,

$$I_z = < S_z > = < E_0 \times H_0 \, Cos^2(\omega t - kz) > \tag{3.6}$$

and simplifying the time average of the cosine,

$$< Cos^2(\omega t - kz) > = \frac{1}{T} \int_0^T Cos^2(\omega t - kz) dt = \frac{1}{2} \tag{3.7}$$

we find,

$$I_z = \frac{1}{2} {E_0}^2 (\frac{\epsilon_0}{\mu_0})^{1/2}. \tag{3.8}$$

Thus the intensity is proportional to the amplitude of the electric field squared, ${E_0}^2$.

The reactions in the process of figure 3.2 are occurring on extremely different time scales, which causes problems computing these properties. In order to accurately

compute wave propagation through a medium, the time steps must be on the same order as the period of the wave to prevent numerically induced attenuation of the wave. We determined that with a length of $20\mu m$ for the sample size, a time step of $2\text{x}10^{-17}$ seconds was needed to obtain full lightwave propagation through the resin for a wavelength of $\lambda = 514nm$ and this was run for $50\text{x}10^{-14}$ seconds.

There are, however, two issues that have posed a significant challenge in this research. First, it is not realistic to compute such small time steps throughout the full length of the time it takes to complete the polymerization process (on the order of seconds). The polymerization is linearly related to the intensity, which is the average of one period (in this case $\sim 250\text{x}10^{-17}$s), but due to modeling constraints the power flow is calculated for each time step ($2\text{x}10^{-17}$s) at a single moment in time. If the polymerization process was occurring on a similar time scale, this would cause a problem in the computations, however, polymerization occurs extremely slowly in comparison. Thus when $\Delta\tilde{P}$ values calculated from S_z are summed over 125 time steps, the effect is the same as averaging as long as $\tilde{P}$ has not significantly changed.

The second issue in this model, due to the wave propagation constraints, is that the lightwave has not fully propagated across the resin before photopolymerization begins. In this *ideal* model with perfect conditions and no material loss, this does not reflect the real situation. However, in the real problem, the lightwave attenuates as it travels through the resin, so the lightwave does not actually traverse the entire length of the sample, which gives us the correlation between the model and a real world example, validifying this model.

3.2 Polymerization Rate Equation

The photopolymerization rate equation was previously derived in section 2.4. Recall equation (2.11),

$$\frac{d}{dt}\tilde{P} = \frac{\phi I}{d(0)A(0)}[1+\kappa\tilde{P}(t)]^{\frac{1}{3}}[1-e^{-\epsilon d(0)A(0)[1+\kappa\tilde{P}(t)]^{-\frac{1}{3}}(1-\tilde{P}(t))}]. \tag{3.9}$$

There are a number of parameters within this equation defined by [7], which are difficult to measure for a given resin system. Also, in order to account for the electromagnetic aspects

of this reaction and the polymerization, it is necessary to scale down the rate equation to the time scale of the wave propagation. Therefore, in this thesis, we propose a simplified polymerization concentration equation of the form,

$$\tilde{P}(s) = e^{-\beta/s} \tag{3.10}$$

which results in the rate equation defined as,

$$\frac{d\tilde{P}}{ds} = \frac{\beta}{s^2} e^{-\beta/s}. \tag{3.11}$$

In these two equations, we have defined a new variable s, which is referred to as the local time. The variable t is the actual (global) time that is divided into time steps Δt in the flowchart of figure 3.2. On the other hand, $s(r, z)$ at any time step is related to the state of polymerization throughout the resin, $s(r, z) = -\beta / ln[\tilde{P}(r, z)]$ and is updated for each time step. Additionally, s can be scaled according to the saturation time required. Figure 3.5 is a pictoral representation of including the local time, $s(r, z)$, into these computations. Figure 3.5 (a) shows a resin bath at global time $t = 0$ with zero percent polymerization. At some time t, figure 3.5 (b) shows the state of polymerization where point a and point b within the resin are at different polymerization states which correlate to where on the polymerization curve they fall as a function of $s(r, z)$, as shown in figure 3.5 (c).

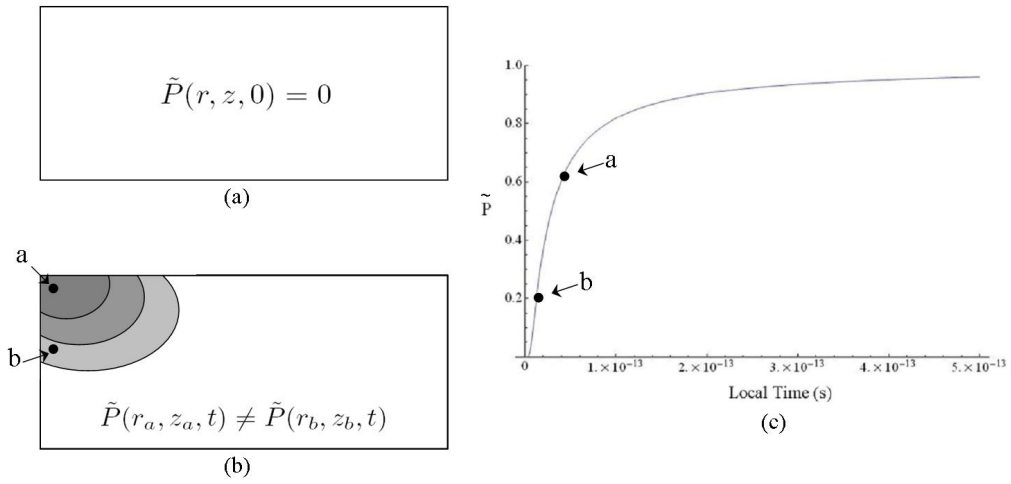

Figure 3.5: Explanation of local time variable, (a) polymerization at time $t = 0$, (b) polymerization at time t, (c) polymer concentration curve showing spatial dependence.

Figure 3.6 shows a comparison of the two different polymerization curves. The first graph plots the polymer concentration equation proposed by Dorkenoo *et al.* (based off of equation (2.12)). The second graph shows the simplified polymerization curve (equation (3.10)). Both curves are plotted with respect to the local time of the reaction and the constant β has been adjusted to account for the time discrepancy between the electromagnetic interactions and the rate of polymerization. We found that a β value of $1\text{x}10^{-14}$ optimized equation (3.10) to obtain a similar polymerization curve on the desired time scale. It can be seen that the two curves are very similar in the rate of polymerization, although not identical. This simplification allows for a simpler computation and makes scaling the equation to a particular time scale more straightforward by adjusting only one parameter as opposed to changing two parameters that are nonlinearly related. Due to the obvious benefits of this simplified equation, we have used this as the basis for the rate of polymerization within a resin undergoing photopolymerization and in the following sections we define the change in index of refraction and the change in density in relation to this chemical property. In future studies, the actual polymerization rate equation 3.9 could be similarly scaled.

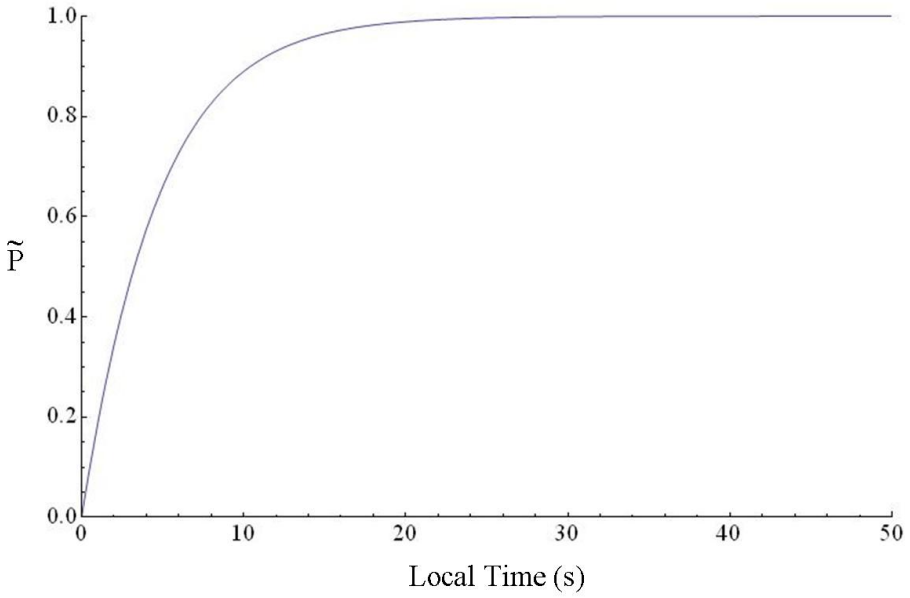

(a)

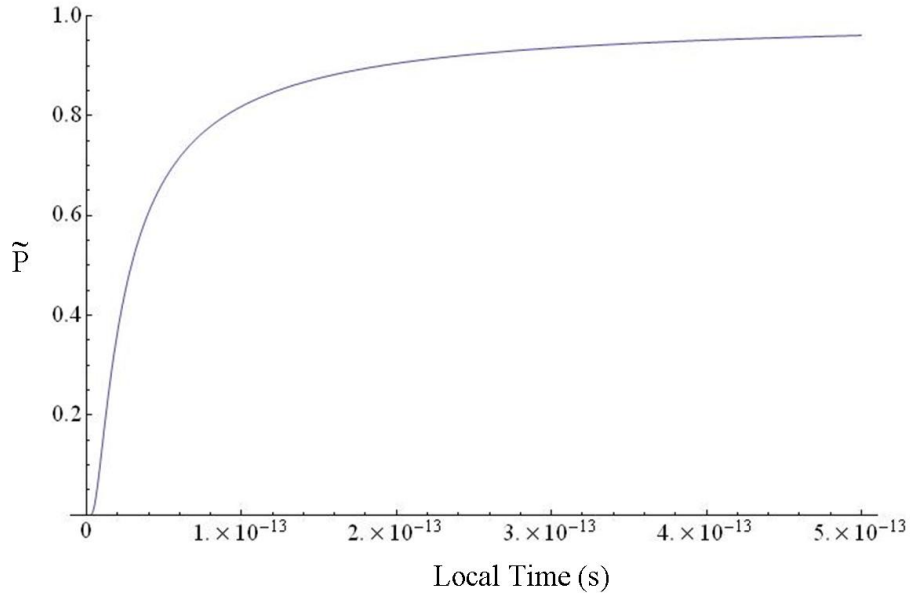

(b)

Figure 3.6: Polymerization rate equations. (a) the original polymerization rate equation from [7] and (b) simplified rate equation for the adjusted time scale of equation (3.11).

3.3 Refractive Index

The next step in the process from figure 3.2 is to relate the refractive index change to the polymerization concentration. The index of refraction can be defined as an initial index (n_0) that changes with each time step (Δn). Since this is a time dependent process, we update the refractive index as,

$$n_t = n_{t-1} + \Delta n_t \tag{3.12}$$

The following sections discuss the development of the equation for Δn beginning with a linear relationship and then incorporating equation (3.11) to include a saturation effect. For all examples in this thesis we apply the SPA polymerization process, however, the model can be easily extended to apply the TPA process as well.

3.3.1 Linear Model

In order to gain a better understanding of the COMSOL model, we began by modeling the change in refractive index with a linear equation defined as,

$$\Delta n(r, z) = \alpha S_z(r, z)\Delta t \tag{3.13}$$

where α is a scaling constant and S_z is the power flow. This model does not include saturation effects, therefore we do not expect to see full self-writing phenomena.

3.3.2 Saturation Model

The next step was to create a more realistic representation of the photopolymerization process, adding in the saturation of the polymerization equation. The change in index is related to the polymerization equation defined as,

$$\Delta n(r, \theta, z, t) = \alpha S_z(r, \theta, z, t)\frac{d\tilde{P}(r, \theta, z, t)}{dt}\Delta t. \tag{3.14}$$

This can be simplified slightly with our assumption that there is rotational symmetry within the resin, giving the following relationship,

$$\Delta n(r,z,t) = \alpha S_z(r,z,t)\frac{d\tilde{P}(r,z,t)}{dt}\Delta t. \tag{3.15}$$

Recall the simplified polymerization concentration equation (3.10), from which the rate is defined by equation (3.11). Substituting equation (3.11) into equation (3.15), our equation for Δn now becomes,

$$\Delta n(r,z,t) = \alpha S_z(r,z,t)\frac{\beta}{s^2}e^{-\beta/s}\Delta t. \tag{3.16}$$

3.4 Density

The final step to accurately model the photopolymerization process comes through adding in the change in density of the resin as it polymerizes. As mentioned, this is not a trivial change and can significantly affect the desired outcome in the writing process if not properly accounted for. Figure 3.7 demonstrates the importance of this effect through a micro-woodpile structure created using TPA by Houbertz [14]. In the first photo the

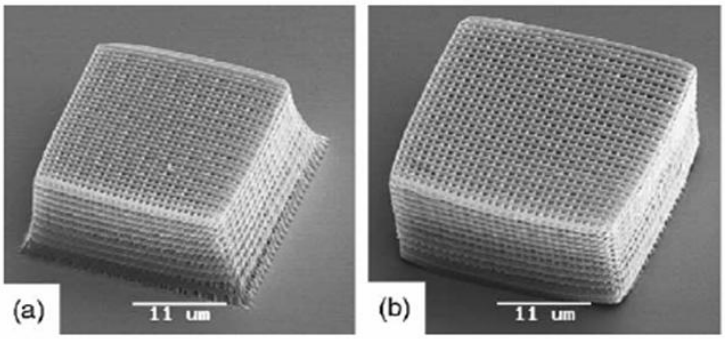

Figure 3.7: SEM photo of a micro woodpile written using TPA, (a) shows the deformation from the density change during the curing process, (b) depicts the woodpile with included deformation to correct for density change [14].

change in density was not included when designing the micro-structure and it can be seen that there is significant deformation at the base of the structure due to the change in density. The second photo is the same woodpile stacking design, but with a pre-defined

distortion to compensate for the change in density. This example illustrates the significance of including this change when designing a system using the photopolymerization process for fabrication.

Modeling this effect would ideally be done by adding a dummy temperature load to the subdomain in the model, however, due to licensing constraints this option was not available to us. Instead a body force was applied to the subdomain that would simulate the change in density to obtain the same type of deformation observed in the study by Dorkenoo *et al.* [7].

We define a dummy body force on the volume (F_v) as,

$$\mathbf{F_v}(r, z, t) = F_0 \, \tilde{P}(r, z, s) \tag{3.17}$$

where F_0 has units of force per unit area. Consider the unit cube with the uniform compressive force, F_0, applied to the cube as shown in figure 3.8. The change in volume can then be written as,

$$\Delta V = (1 + \epsilon_1)(1 + \epsilon_2)(1 + \epsilon_3) - 1 \tag{3.18}$$

Equation (3.18) can be simplified assuming small strains and neglecting higher order terms,

$$\Delta V \cong \epsilon_1 + \epsilon_2 + \epsilon_3 = -3(1 - 2\nu)\frac{F_0}{E}. \tag{3.19}$$

where E is the Young's modulus of the resin and ν is the Poisson's ratio for the resin. Using the fact the the overall desired density change is approximately 4%, when $P(t_f) \cong 1$ at the final time step, F_0 can be solved for using the relationship,

$$\frac{\Delta V}{V} = 0.04 = -3(1 - 2\nu)\frac{F_0}{E}. \tag{3.20}$$

Therefore F_0 is defined as,

$$F_0 = -\frac{0.04E}{3(1 - 2\nu)}. \tag{3.21}$$

Since this is a dummy body force imposed on the resin, we set $\nu = 0$ to eliminate unrealistic outcomes caused by the Poisson effect. Additionally, we also set the stress-optic effect to zero to remove any effects that may be generated from applying this force. Thus the

force constant can be computed and used to predicted the change in density as defined by equation (3.17).

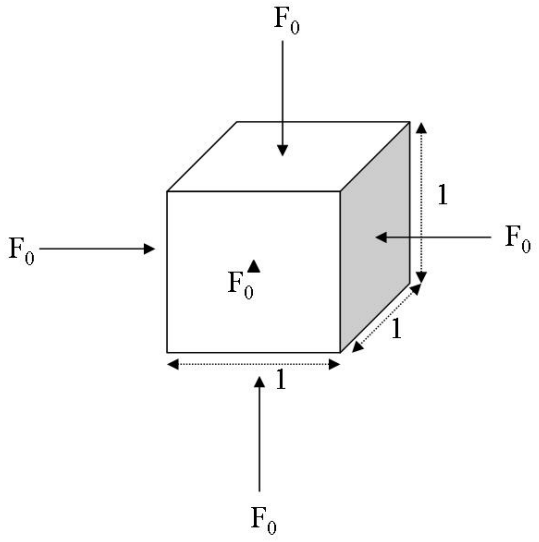

Figure 3.8: Unit cube with a uniform compressive force applied.

3.5 Case Studies

Now that the photopolymerization process has been fully defined accounting for the two critical changing properties, we look at how this model can be applied to two applications. We will examine the case of a single fiber focused into a photosensitive resin bath as well as two fibers aligned with a small separation distance where a drop of resin is placed in the gap between them.

3.5.1 Case 1: Single Fiber into Resin Bath

The first case that is modeled is a single fiber focused into an epoxy resin. Figure 3.9 shows a diagram of the setup for this case study. The output of the optical fiber is a Gaussian distribution whose waist, w_0, is defined by the mode distribution at the

propagating wavelength. We use this as the incident lightwave boundary condition for both cases. The displacement boundary conditions that were placed on the model are specified in figure 3.9 (b). For this case, the incident boundary is constrained in the z-direction because as soon as the light impinges upon the epoxy along this surface, the cured resin bonds with the fiber and as such will not move. The second boundary condition is along the propagation axis (z). Since this is the center of the region being cured and we have assumed rotational symmetry, we constrain this boundary such that it cannot move in the r-direction, only allowing shrinkage in the z-direction along this boundary.

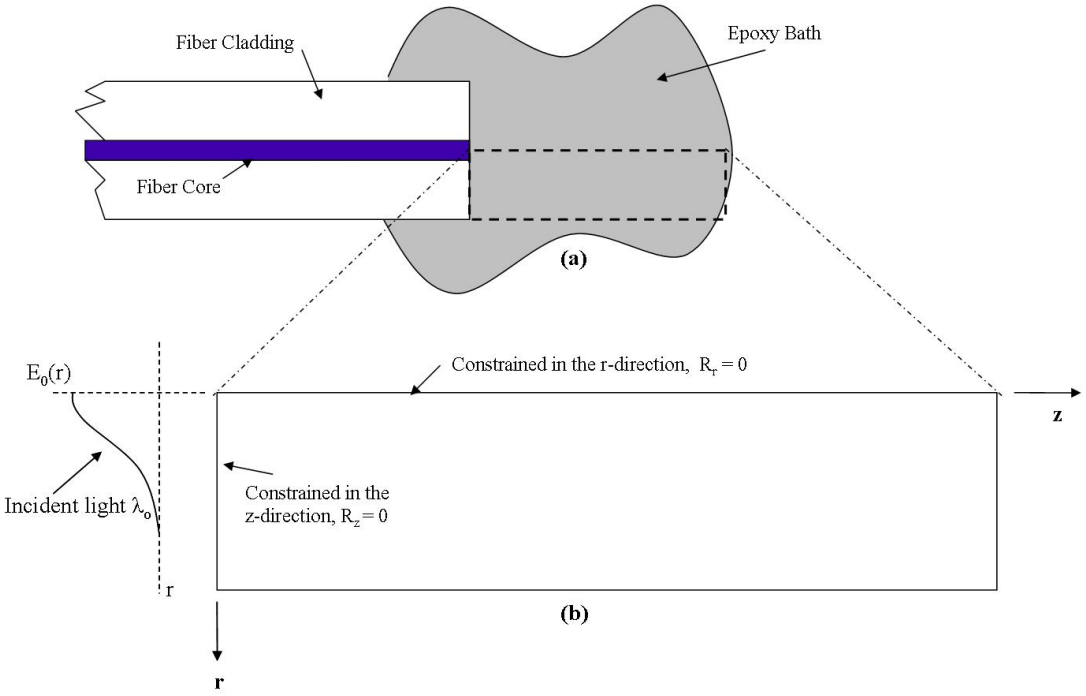

Figure 3.9: Diagram of model for single fiber case study, (a) lab setup and (b) closeup of epoxy section to be modeled.

3.5.2 Case 2: Dual Fibers within Resin Bath

The second case studied includes two fibers aligned with a small gap between them. In the gap, a drop of resin is placed for curing a polymer sensing element. Figure 3.10 shows a diagram of this case. The only difference between case 1 and this case is the inclusion of one more constraint on the displacement boundaries in this case. A constraint in the z-direction has also been added to the $b4$ boundary on the right edge of the model, not allowing it to contract due to the bond formed with the second fiber.

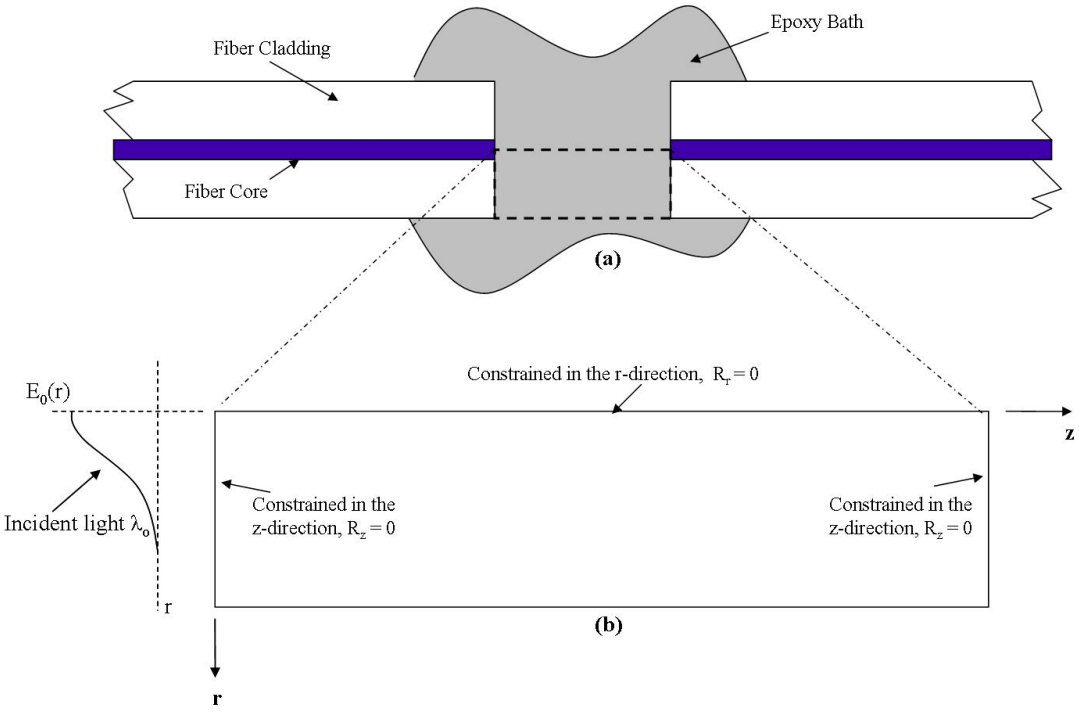

Figure 3.10: Diagram of model for double fiber case study, (a) lab setup and (b) closeup of epoxy section to be modeled.

The next chapter presents the results from the four different cases run with this model. Each of the above cases is presented in order of model development, beginning with the linear change in the index of refraction.

Chapter 4

Results and Discussion

4.1 Linear Polymerization

The results for the linear case are based on the definition of Δn as given by equation (3.13) for the values given in table 4.1. The goal of this case was to verify that the electromagnetic propagation was correct and that the time scaling discussed in the previous chapter produced realistic index of refraction distributions. For this simulation, the change in the density of the resin is not included.

Table 4.1: Parameters for linear change in index

Variable	**Value**	**Units**
w_0	$2\text{x}10^{-6}$	m
λ	$514\text{x}10^{-9}$	m
E_0	$3\text{x}10^{4}$	V/m
n_0	1.484	–
α	$2\text{x}10^{4}$	–

Figures 4.1 (a)-(l) show the results for the power flow, S_z, for the linear Δn equation. Looking at figures 4.1 (a)-(f), it can be seen that full propagation through the sample was achieved. As time progresses, there is an interesting change that can be seen in the power flow. Beginning in figure 4.1 (h) at time $t = 17\text{x}10^{-14}$s, a slight tapering

can be seen. This effect becomes much more apparent in figures 4.1 (i)-(l). In figures 4.1 (k) and (l), the power flow is still approximately Gaussian, but has become more focused with a narrower waist. This result is indicative of the self-focusing/self-trapping nature of photopolymerization and will later be seen to be due to the tapered polymerized region.

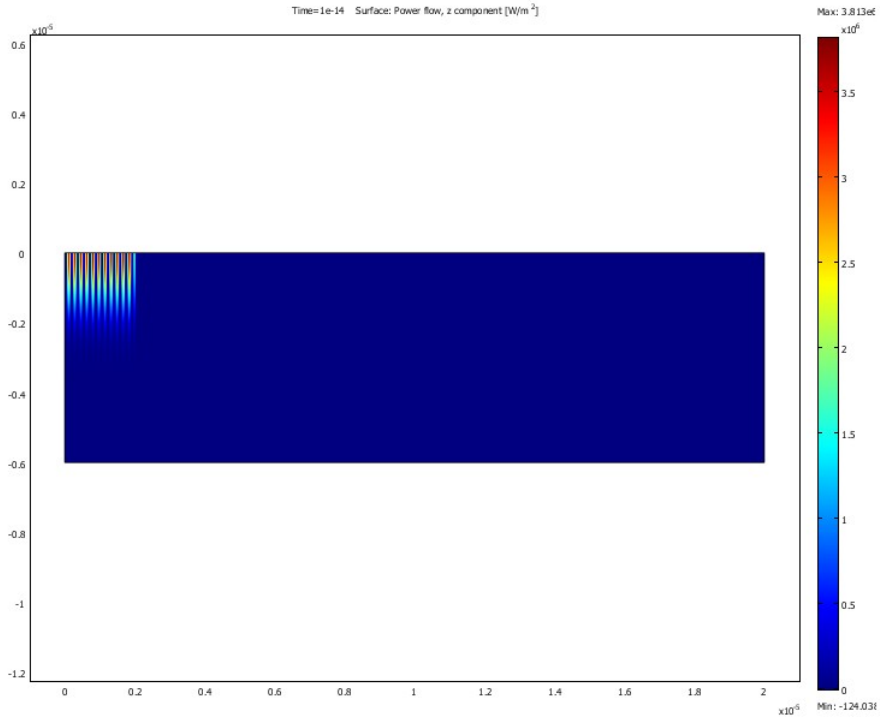

(a) $1\text{x}10^{-14}s$

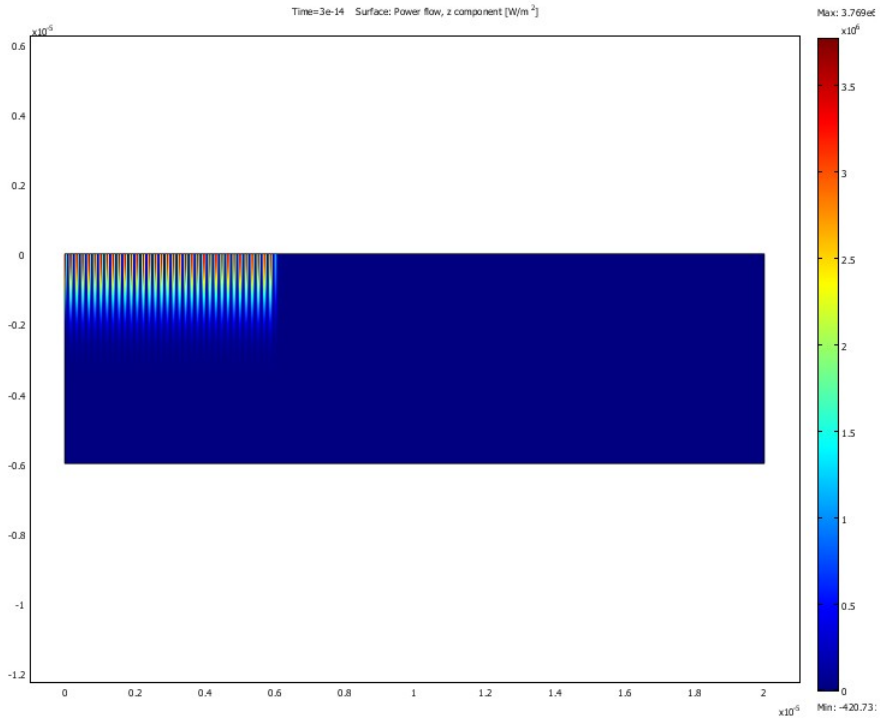

(b) $3\text{x}10^{-14}s$

Figure 4.1: Linear power flow.

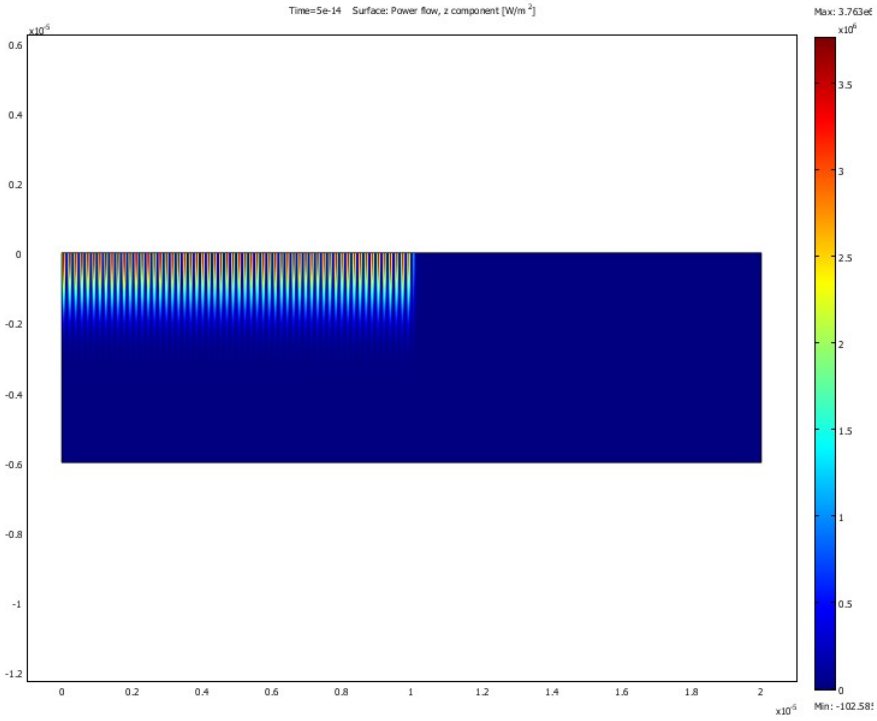

(c) $5\text{x}10^{-14}s$

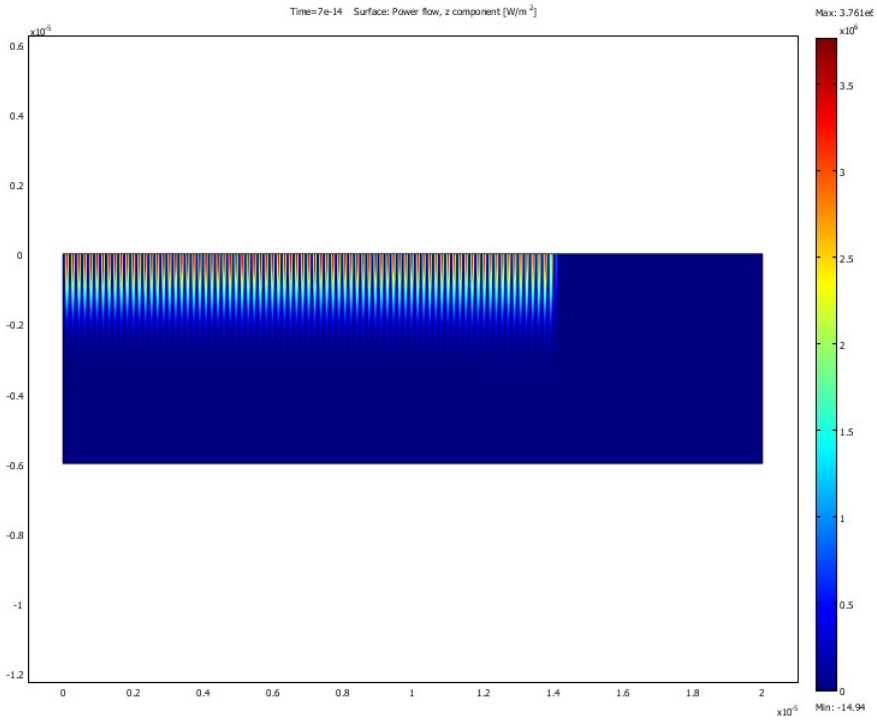

(d) $7\text{x}10^{-14}s$

Figure 4.1: Linear power flow.

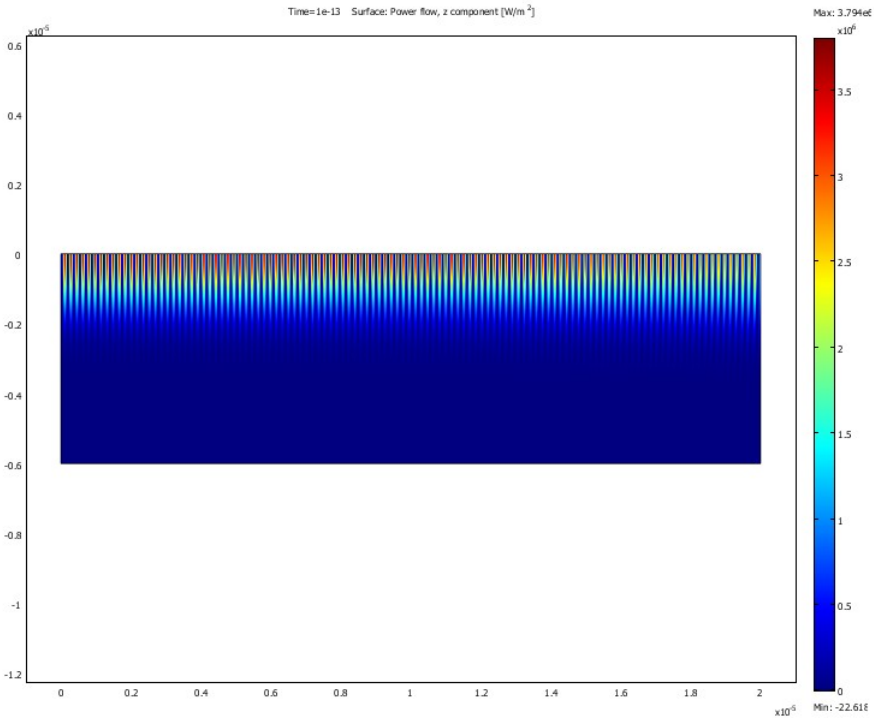

(e) $10\text{x}10^{-14}s$

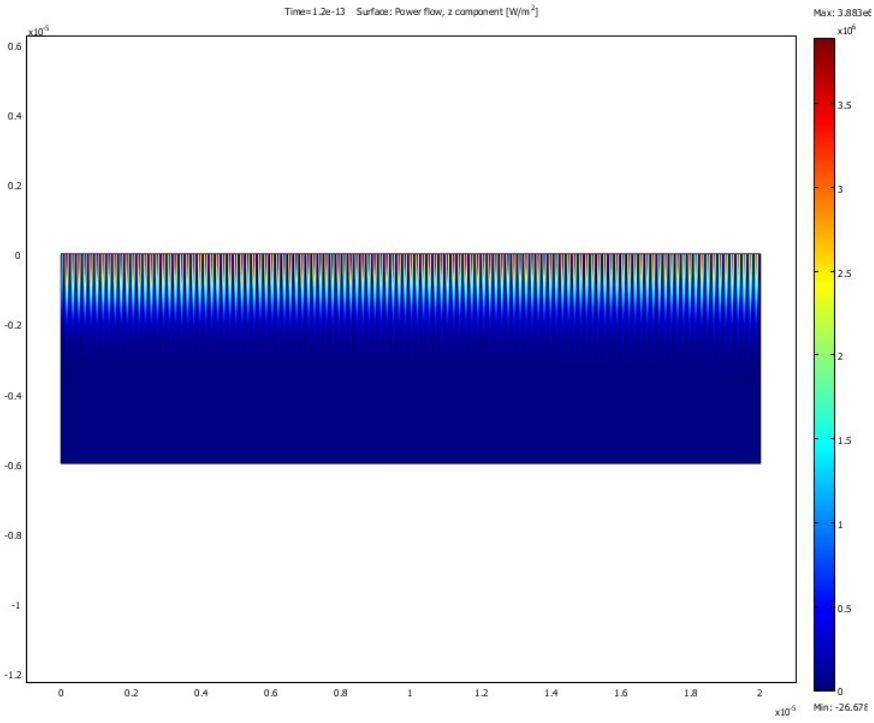

(f) $12\text{x}10^{-14}s$

Figure 4.1: Linear power flow.

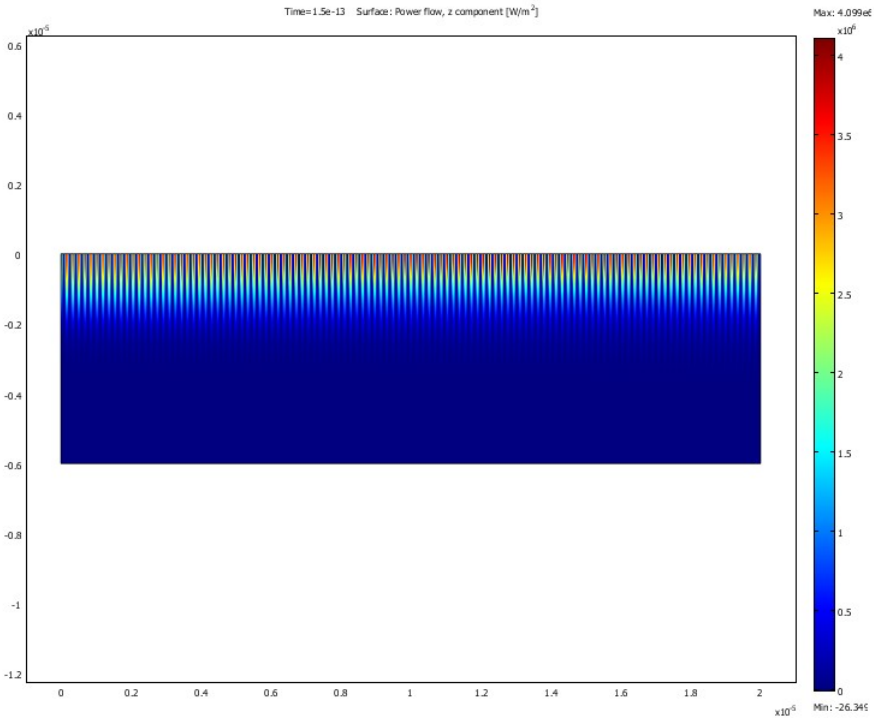

(g) $15\text{x}10^{-14}s$

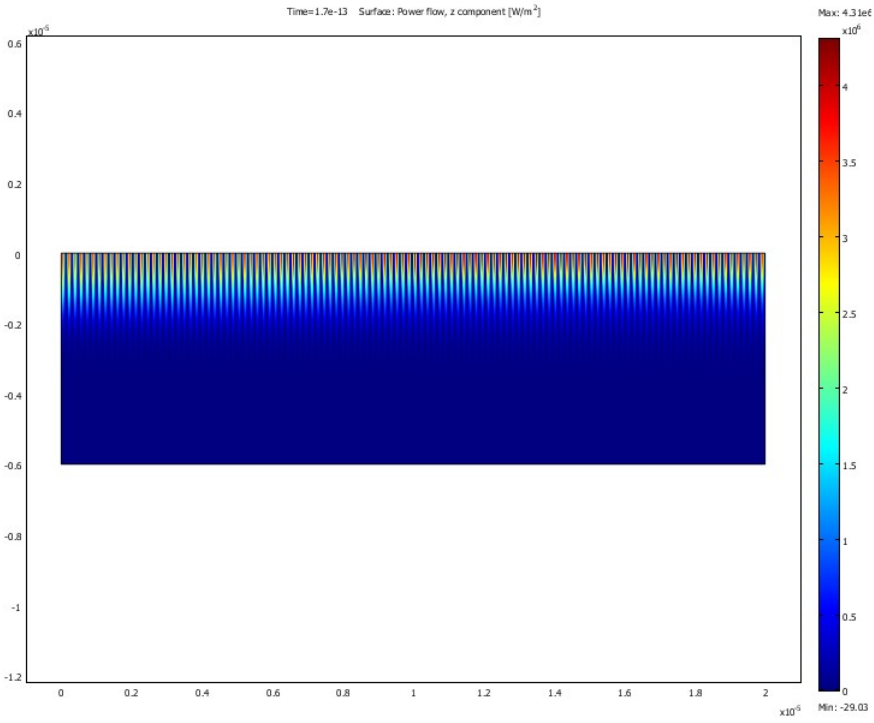

(h) $17\text{x}10^{-14}s$

Figure 4.1: Linear power flow.

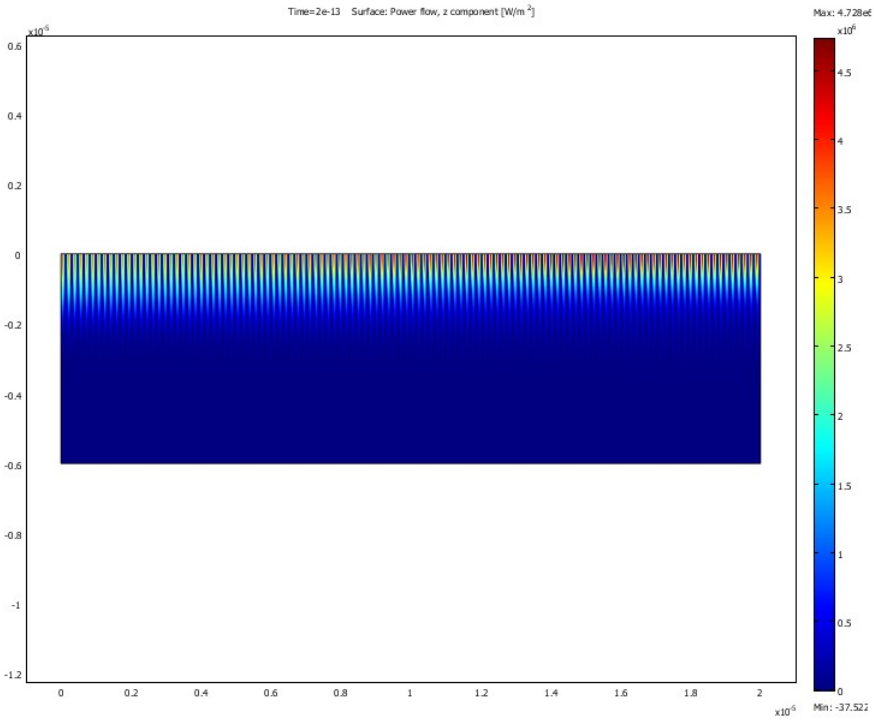

(i) $20\text{x}10^{-14}s$

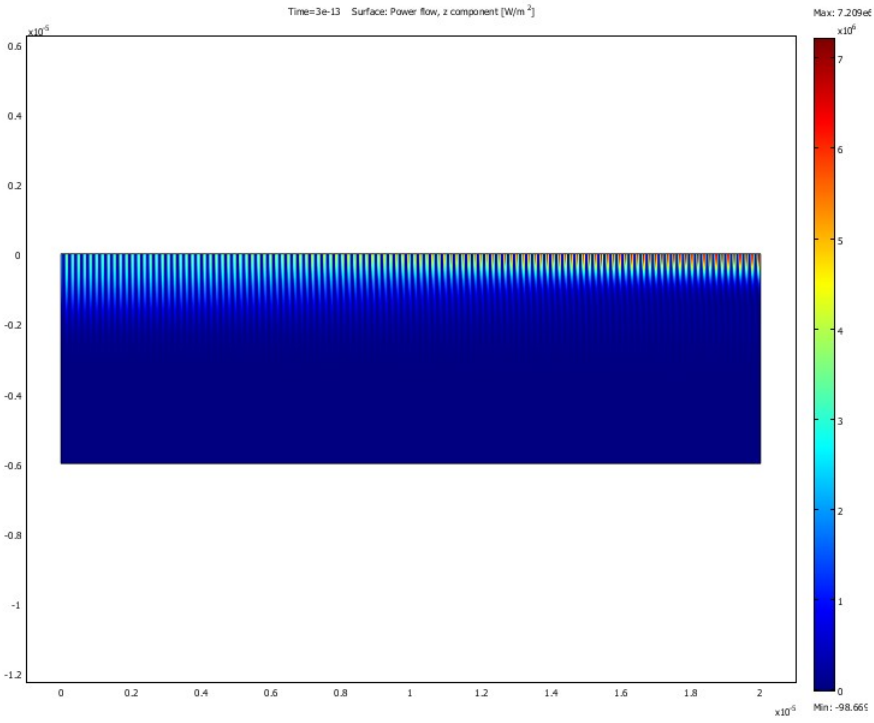

(j) $30\text{x}10^{-14}s$

Figure 4.1: Linear power flow.

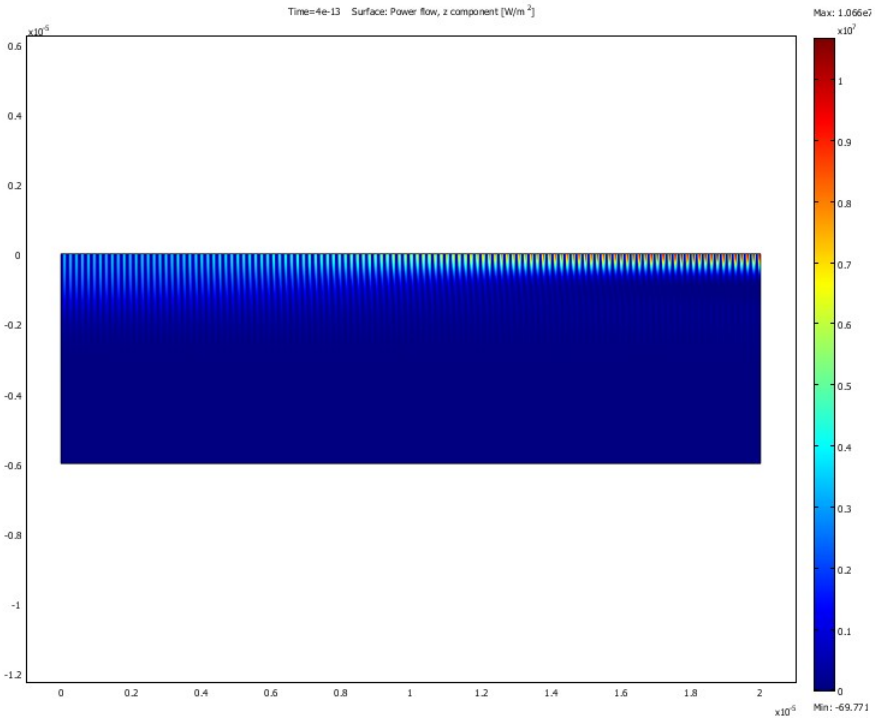

(k) $40\text{x}10^{-14}s$

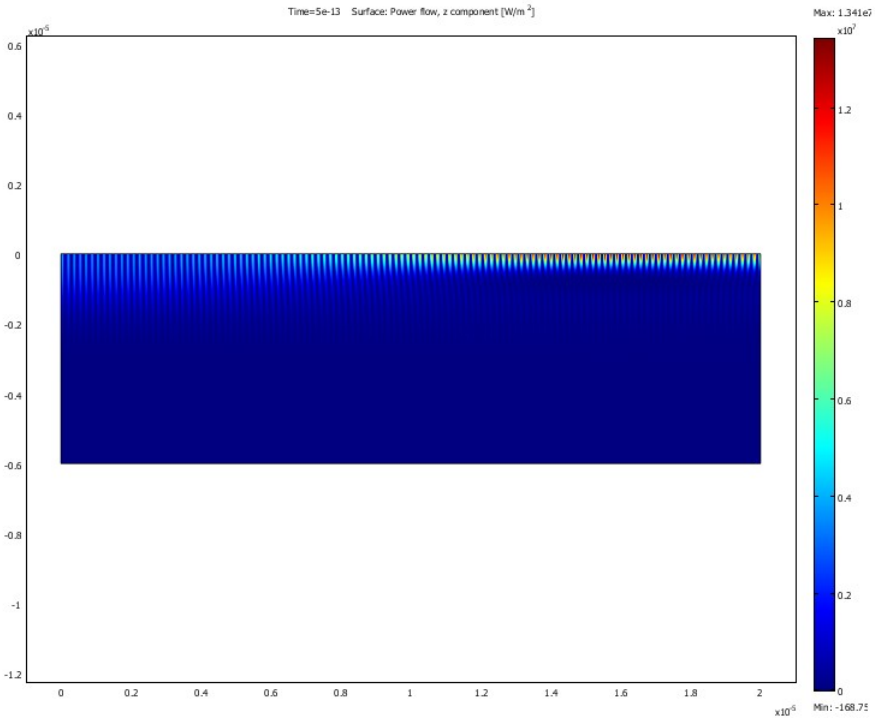

(l) $50\text{x}10^{-14}s$

Figure 4.1: Linear power flow.

Figures 4.2 (a)-(l) depict the refractive index distribution with respect to time for the linear Δn relation for the same time steps as seen in the power flow results of figures 4.1. Looking at figure 4.2 (a) a very slight increase in the refractive index can be seen, but it is localized to the beginning of the sample. Looking at each of the subsequent time steps the progression of the change in the index of refraction can be seen. It is important to note that the scale on each of the figures varies slightly since each graph is a snapshot in time and the index of refraction continues to increase in the linear case. By time $t = 15\text{x}10^{-14}$s, the refractive index has been increased along the entire length of the sample and is relatively confined. In figure 4.2 (h), we see the same tapering effect evident in the power flow from figure 4.1 (h). By time $t = 50\text{x}10^{-14}$s (figure 4.2 (l)), the tapering/self-focusing aspect of this reaction can be seen very well. At the incident boundary there is some dispersion initially, but the increase in the index creates a core/cladding relationship within the resin, allowing for self-trapping which is seen quite clearly at the end of the sample where the resin is being cured more quickly due to the smaller region cured by self-focusing.

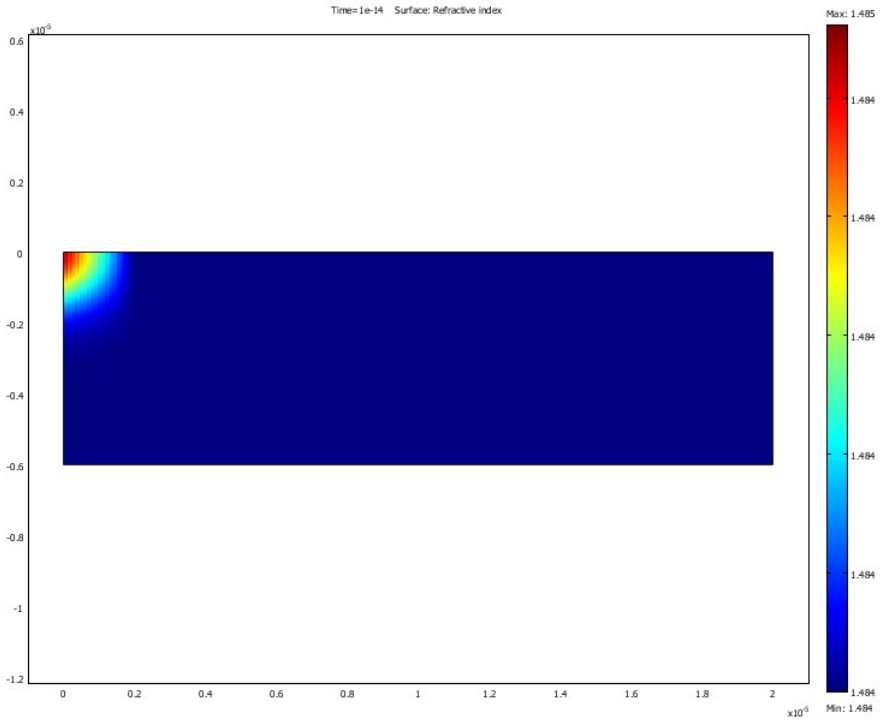

(a) $1\text{x}10^{-14}s$

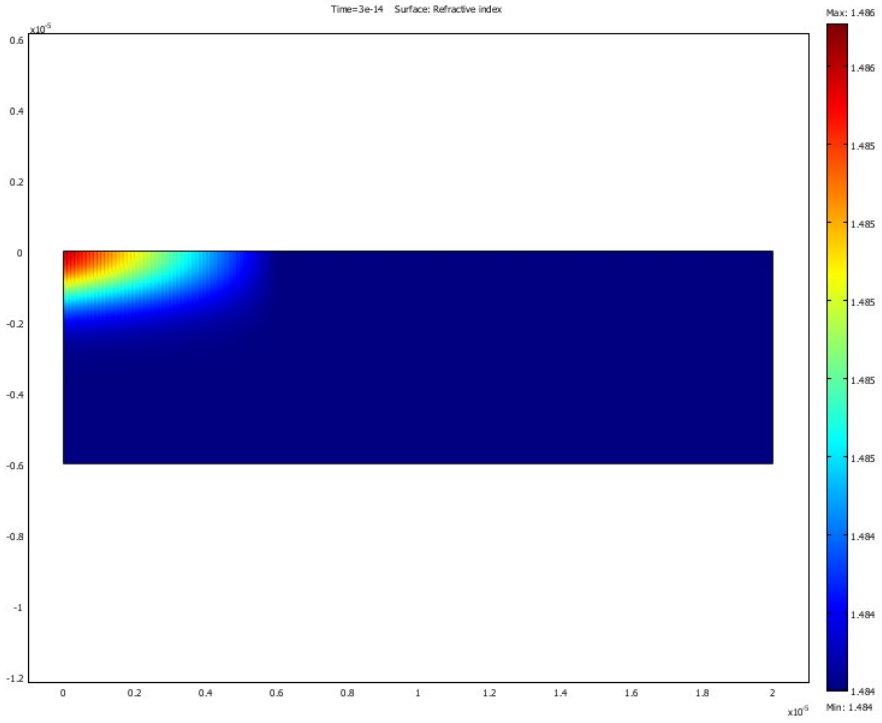

(b) $3\text{x}10^{-14}s$

Figure 4.2: Change in refractive index for linear Δn.

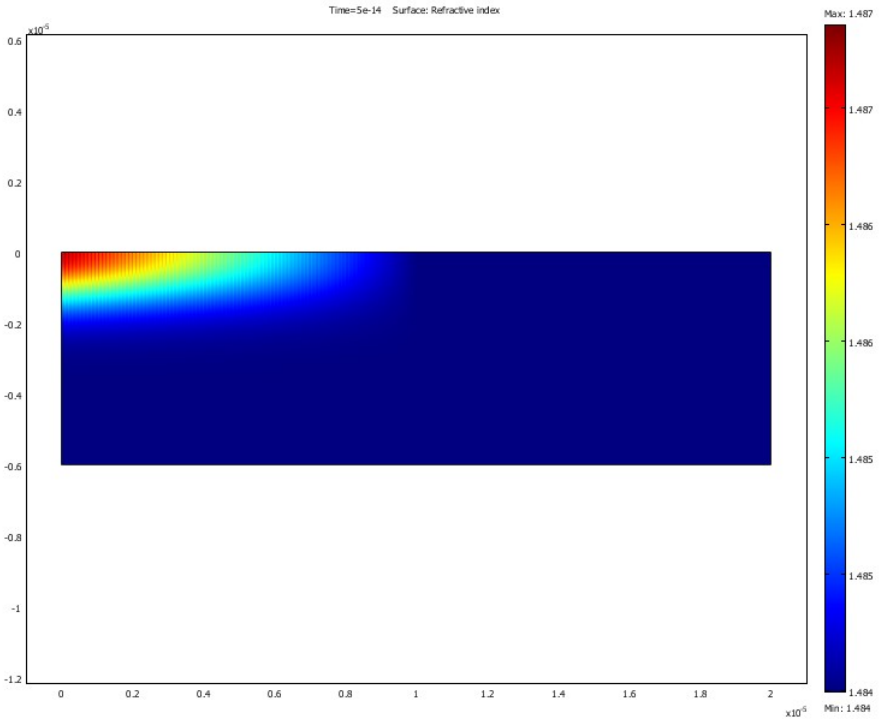

(c) $5\text{x}10^{-14}s$

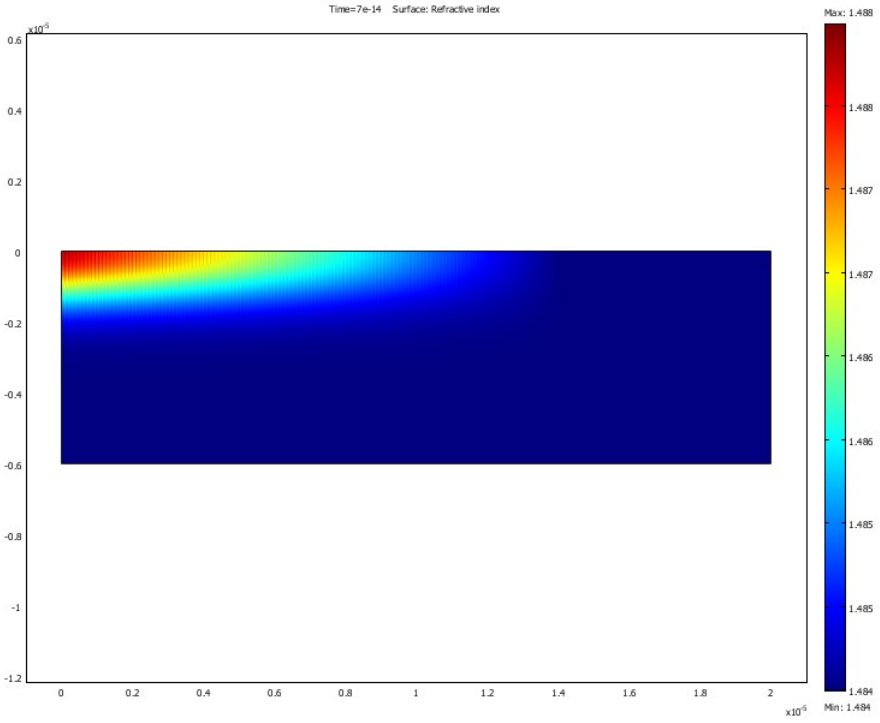

(d) $7\text{x}10^{-14}s$

Figure 4.2: Change in refractive index for linear Δn.

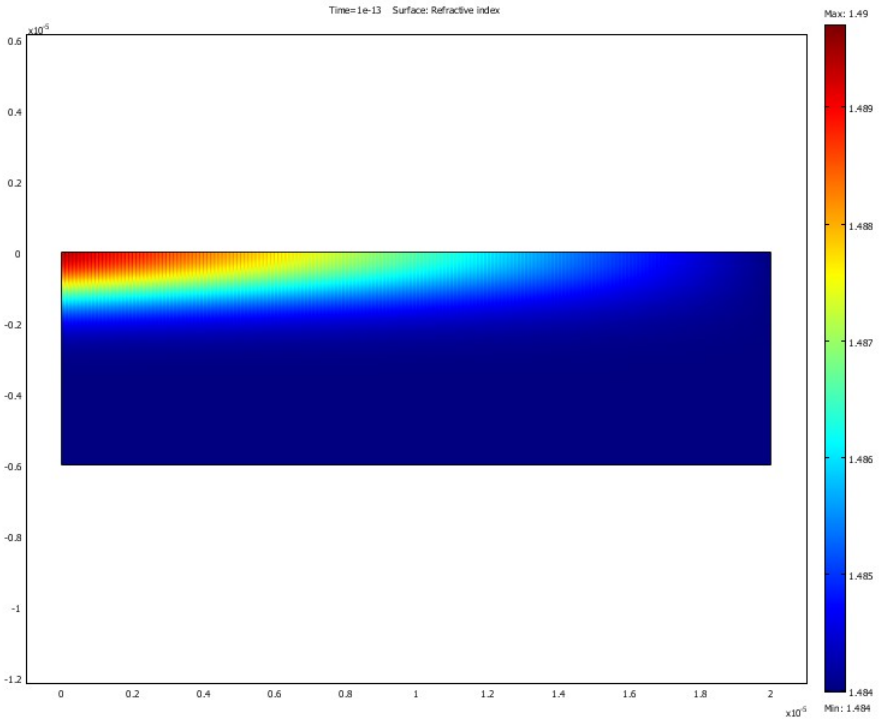

(e) $10\text{x}10^{-14}s$

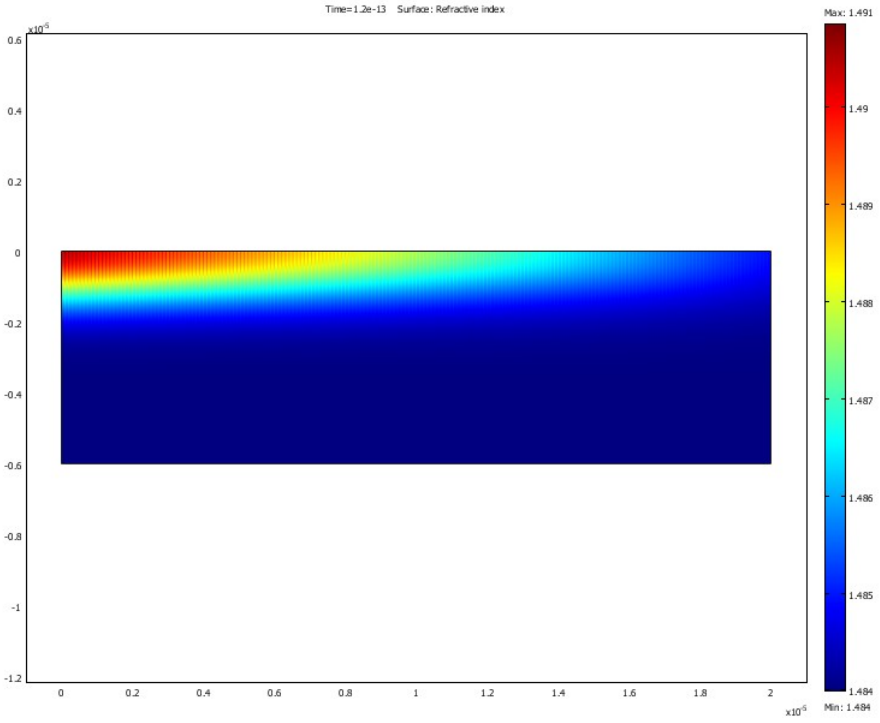

(f) $12\text{x}10^{-14}s$

Figure 4.2: Change in refractive index for linear Δn.

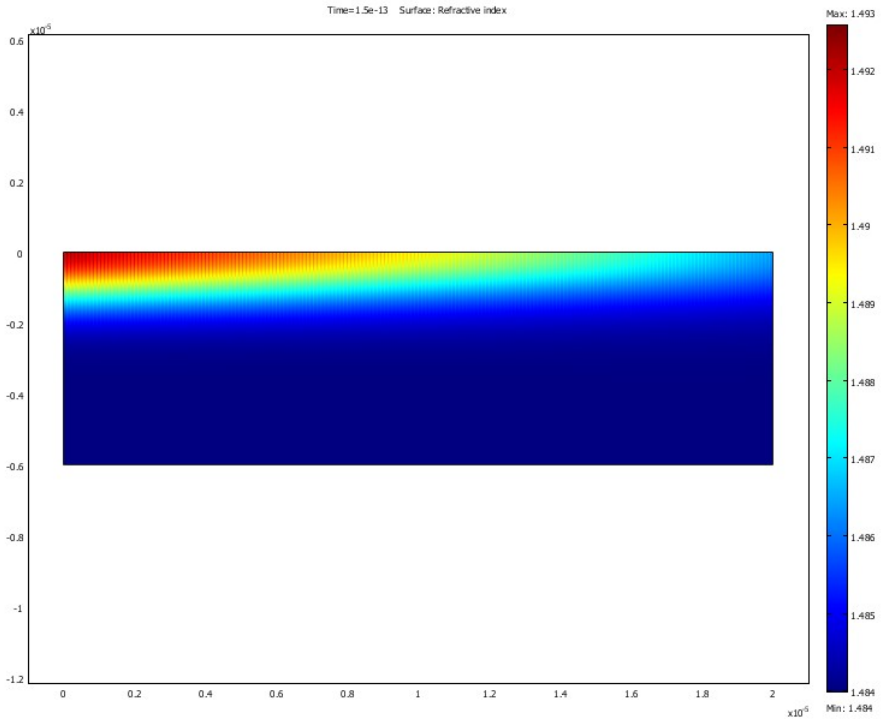

(g) $15\text{x}10^{-14}s$

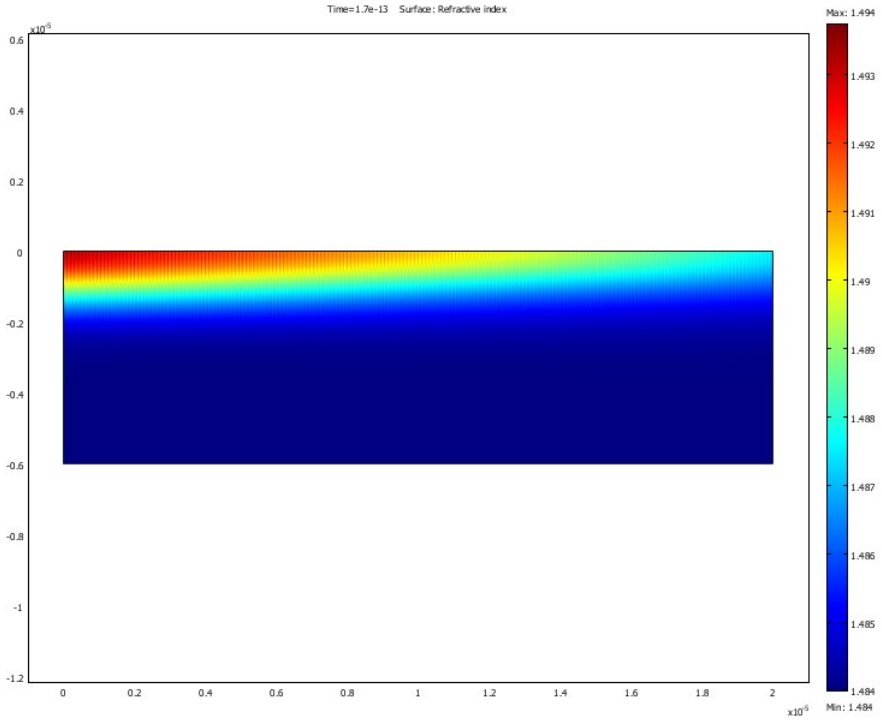

(h) $17\text{x}10^{-14}s$

Figure 4.2: Change in refractive index for linear Δn.

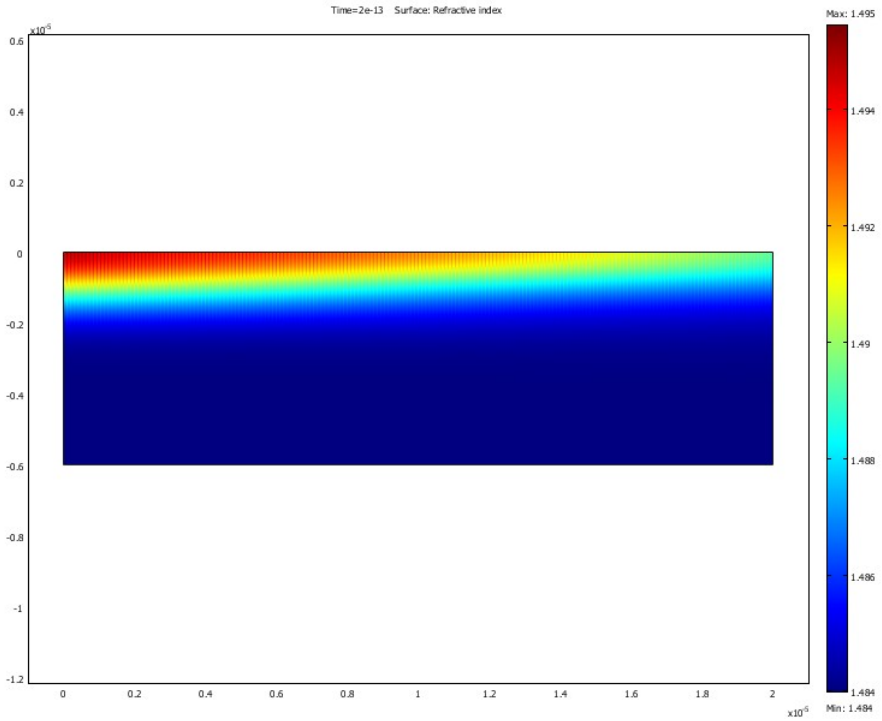

(i) $20\text{x}10^{-14}s$

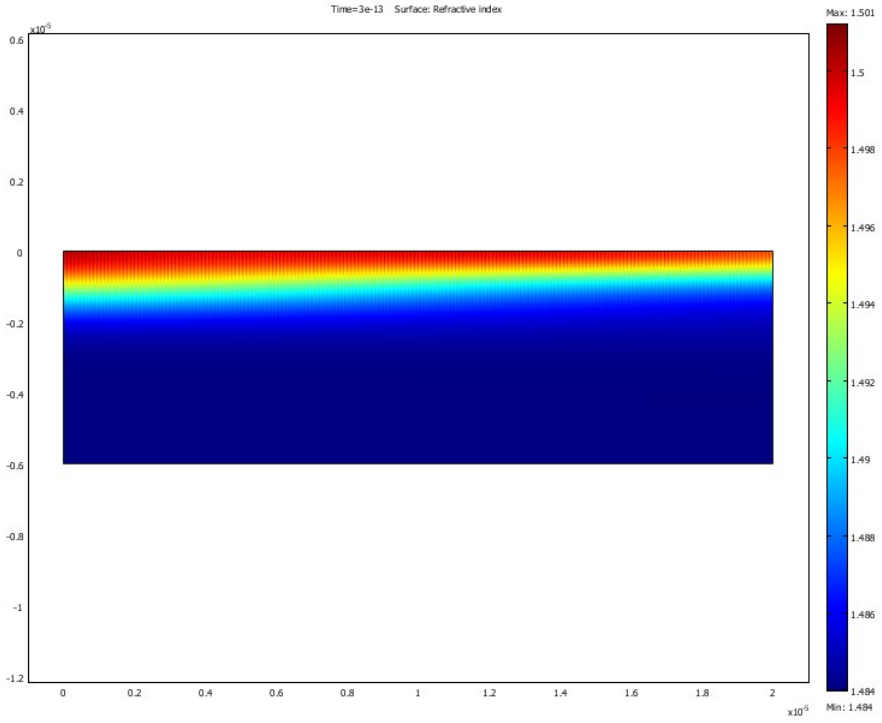

(j) $30\text{x}10^{-14}s$

Figure 4.2: Change in refractive index for linear Δn.

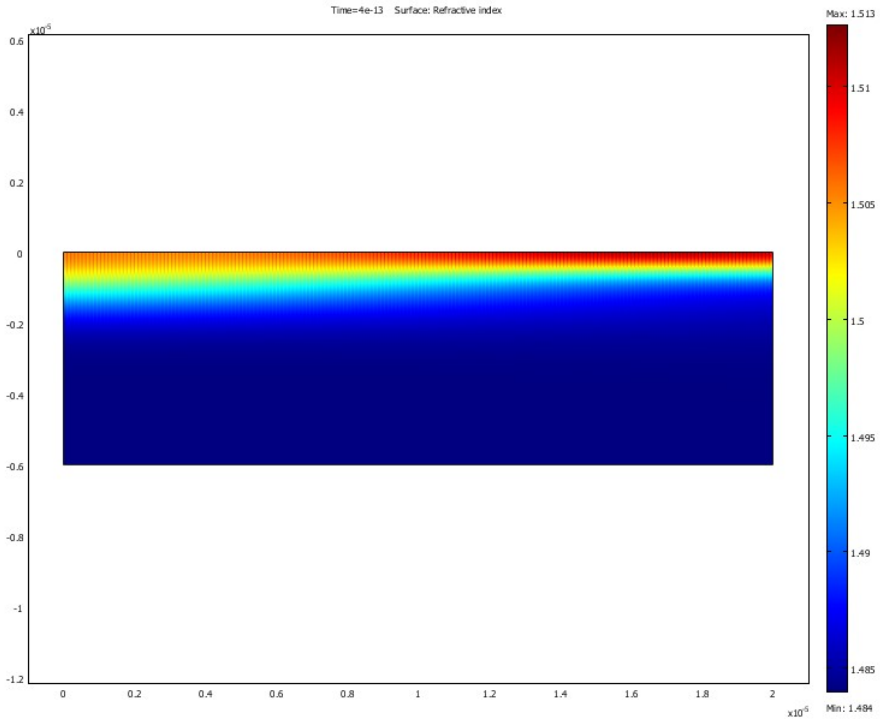

(k) $40\text{x}10^{-14}s$

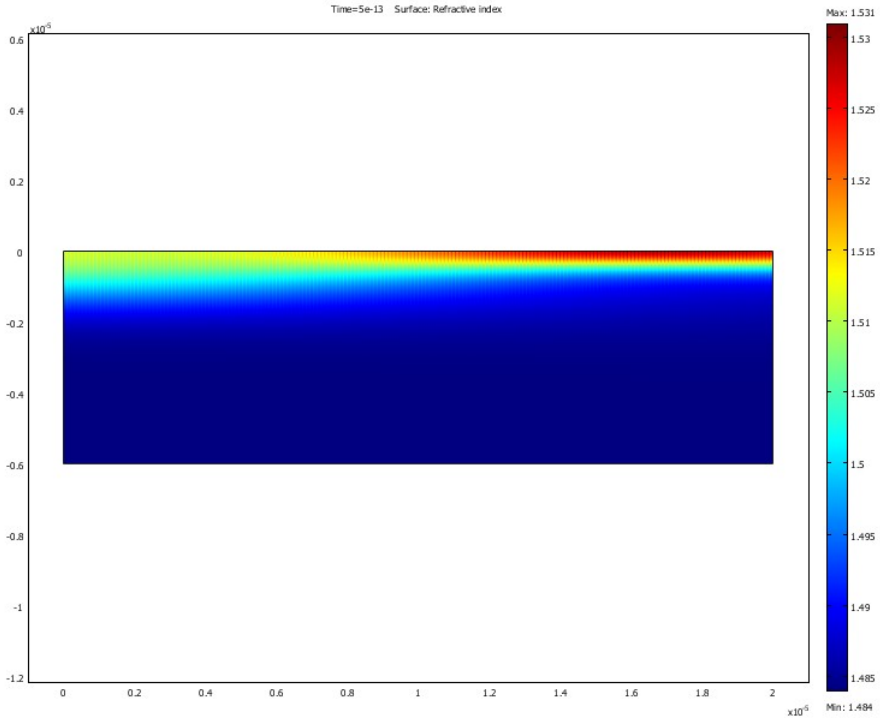

(l) $50\text{x}10^{-14}s$

Figure 4.2: Change in refractive index for linear Δn.

These results demonstrate the various calculations outlined in the flowchart of figure 3.2 work correctly together (other than the density change). However, now we need to include saturation of the refractive index of the cured resin to accurately predict the final geometry of the polymerized waveguide. The next section show the results of including this updated model.

4.2 Saturation Polymerization

In order to more accurately model photopolymerization, we defined the change in index including the saturation effect defined in section 3.3.2, as given by equation (3.16). This model was run for the parameters defined in table 4.2.

Table 4.2: Parameters for saturating change in index

Variable	**Value**	**Units**
w_0	$2\text{x}10^{-6}$	m
λ	$514\text{x}10^{-9}$	m
E_0	$3\text{x}10^{4}$	V/m
n_0	1.482	–
n_{max}	1.52	–
α_s	$1\text{x}10^{-7}$	–
β	$1\text{x}10^{-14}$	–

Looking at the power flow results plotted in figures 4.3 (a)-(l), there is a significant difference between these results and those shown for the previous linear case. The self-focusing aspect of this reaction occurs much earlier than in the linear case. At time $t = 5\text{x}10^{-14}$s (figure 4.3 (c)) we see the first evidence of this property. The self-focusing continues and is dramatically seen through figure 4.3 (f). Once the wave has fully propagated the sample and cured an initial waveguide, we see the power flow spread back out slightly. This is an adjustment of the waveguide which occurs due to the fact that the waist of the propagating mode (determined by the wavelength and index of refraction distribution) is larger than the initial waveguide created. This effect will be shown further with

the results for the change in index below.

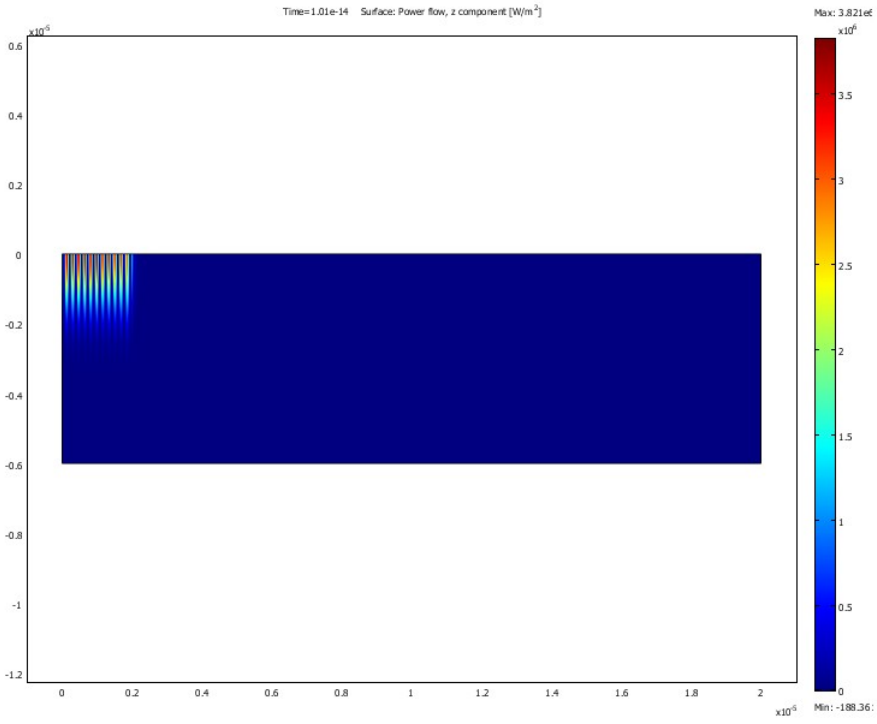

(a) $1x10^{-14}s$

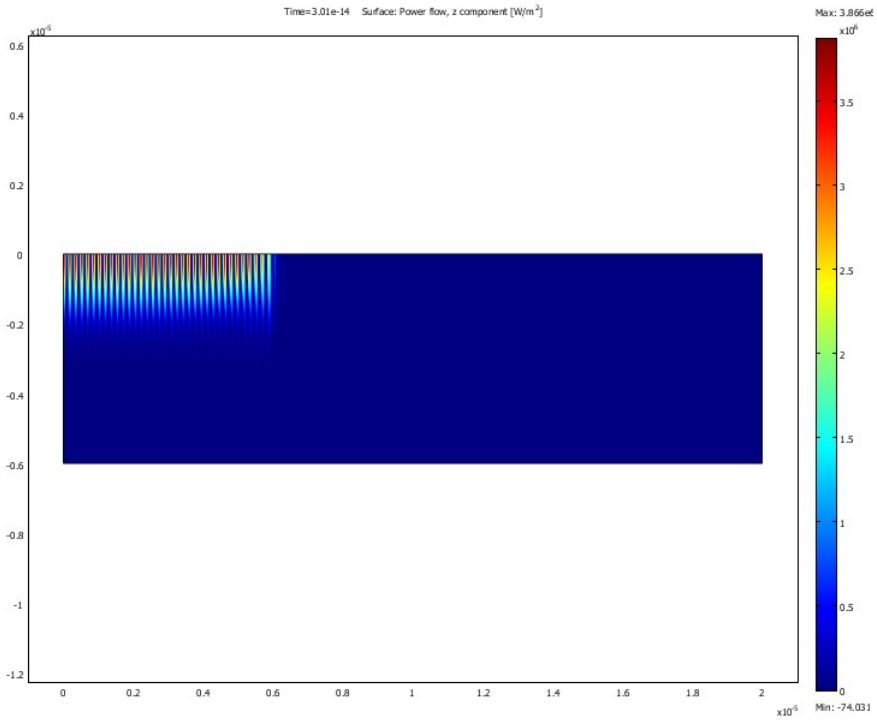

(b) $3x10^{-14}s$

Figure 4.3: Saturation power flow.

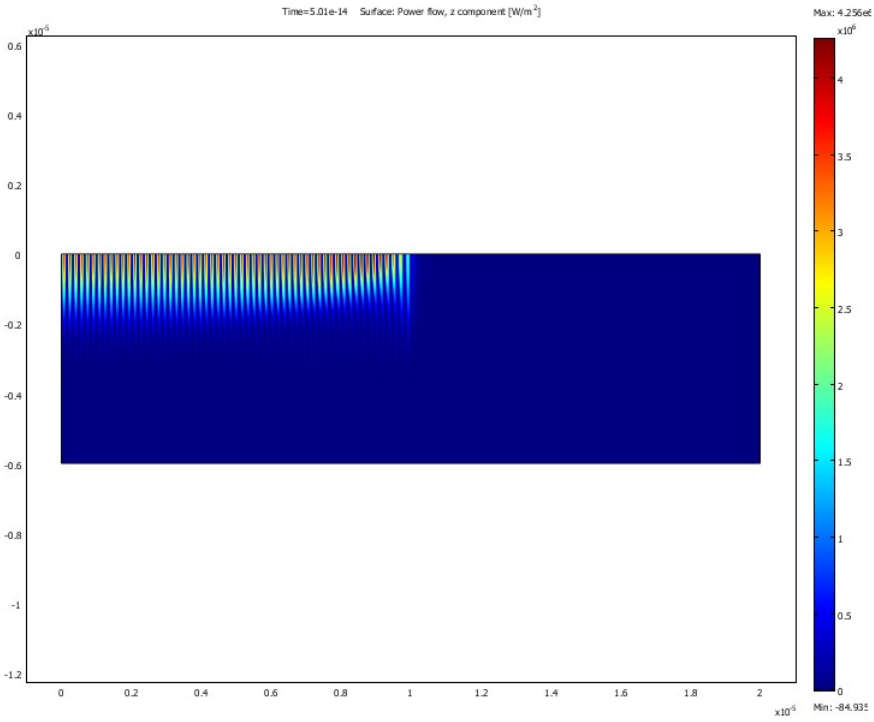

(c) $5\text{x}10^{-14}s$

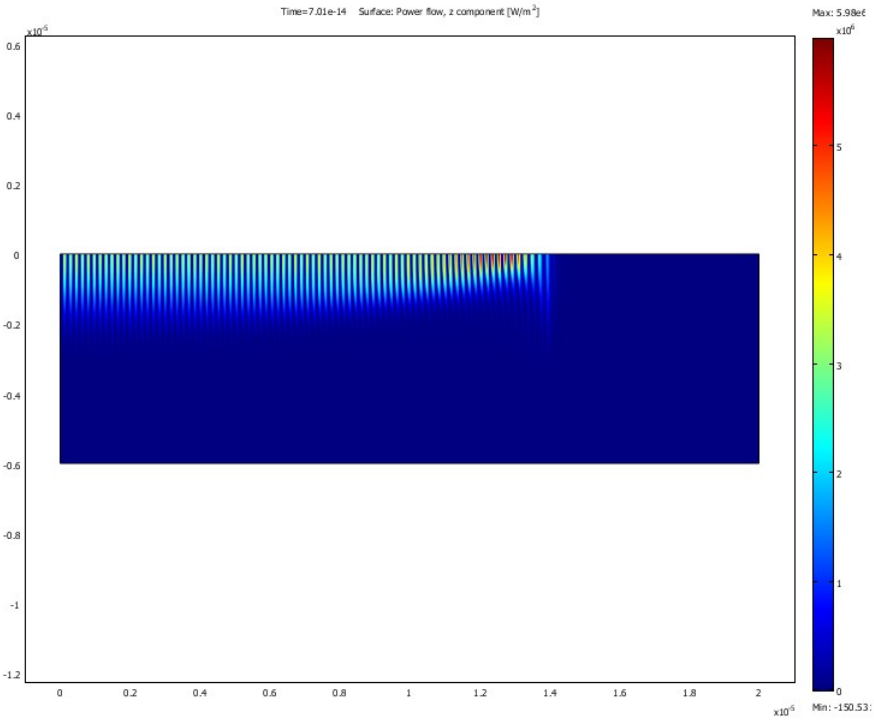

(d) $7\text{x}10^{-14}s$

Figure 4.3: Saturation power flow.

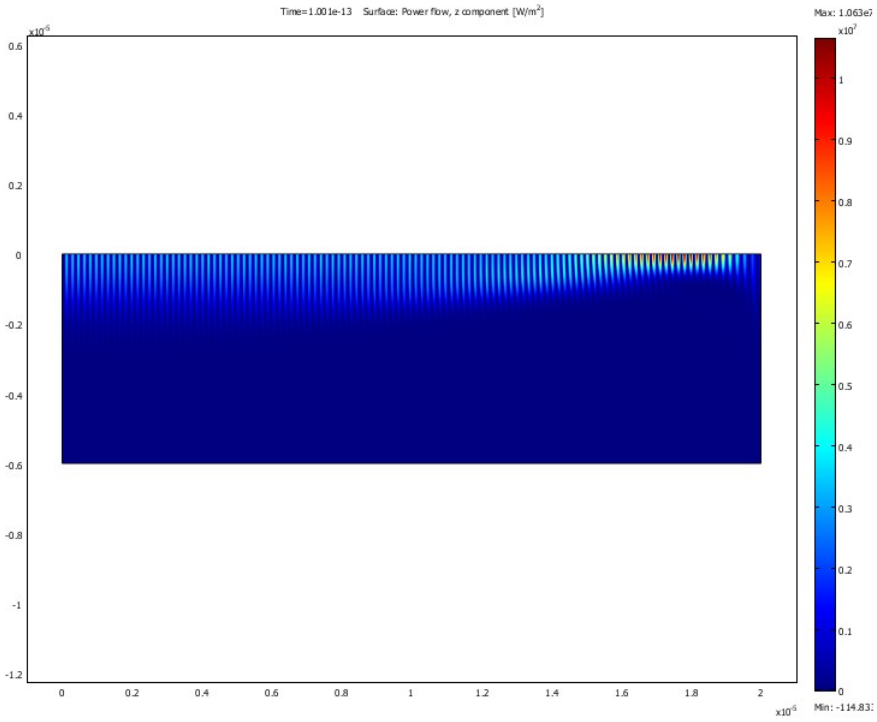

(e) $10\text{x}10^{-14}s$

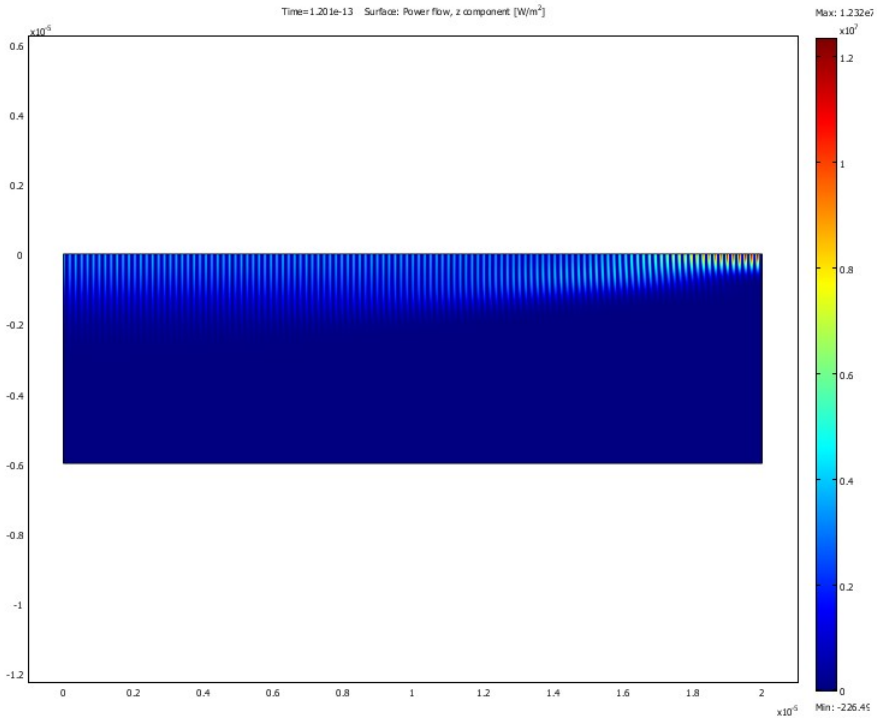

(f) $12\text{x}10^{-14}s$

Figure 4.3: Saturation power flow.

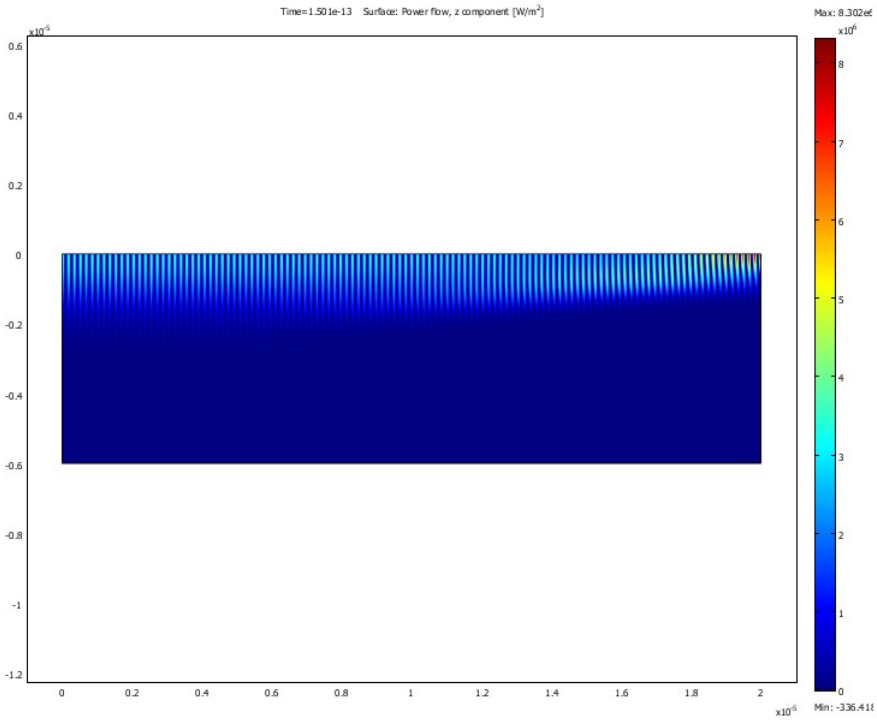

(g) $15\text{x}10^{-14}s$

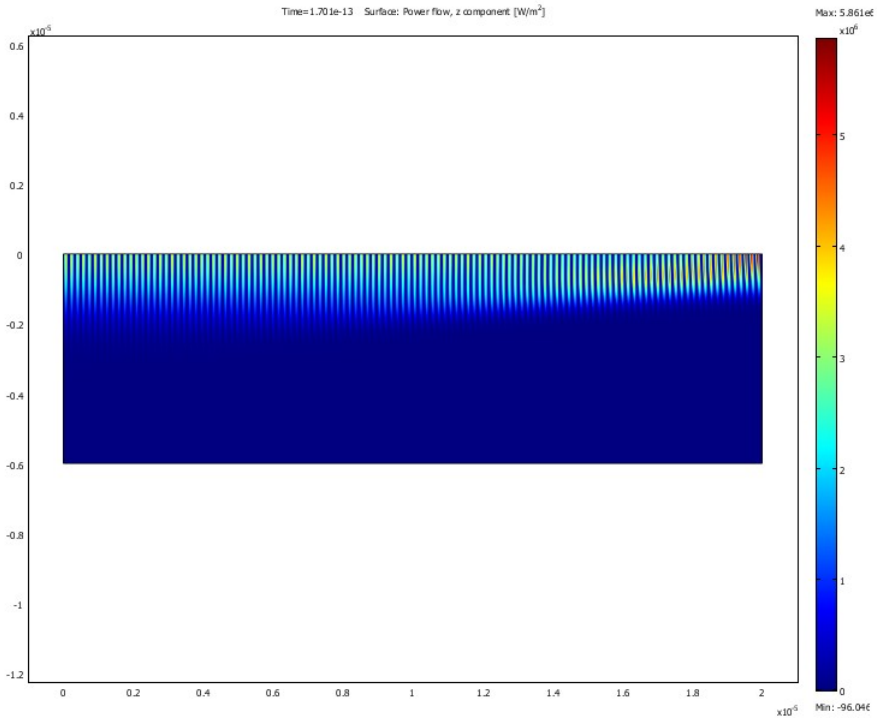

(h) $17\text{x}10^{-14}s$

Figure 4.3: Saturation power flow.

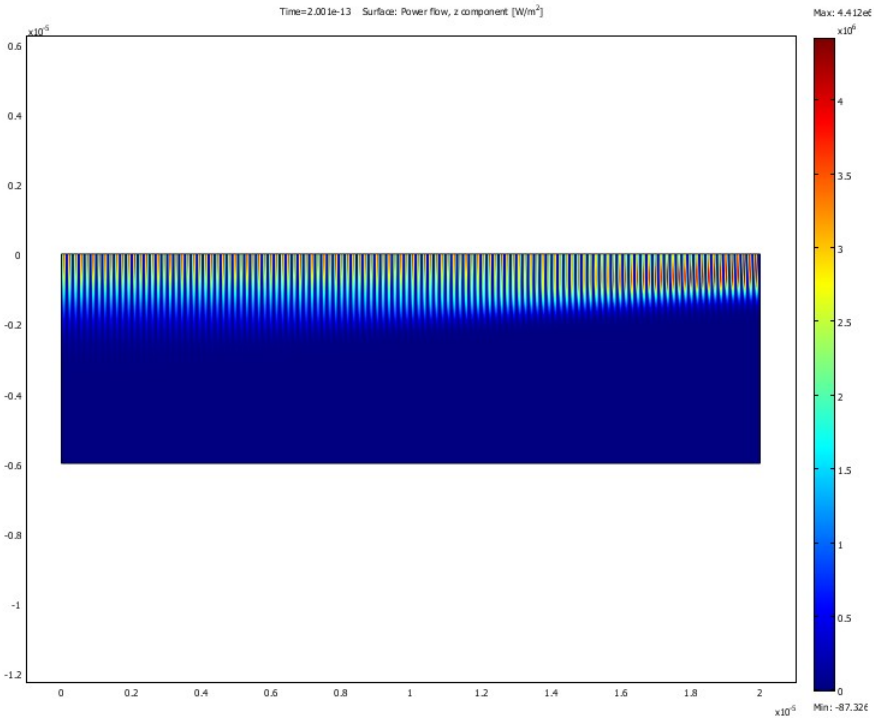

(i) $20\text{x}10^{-14}s$

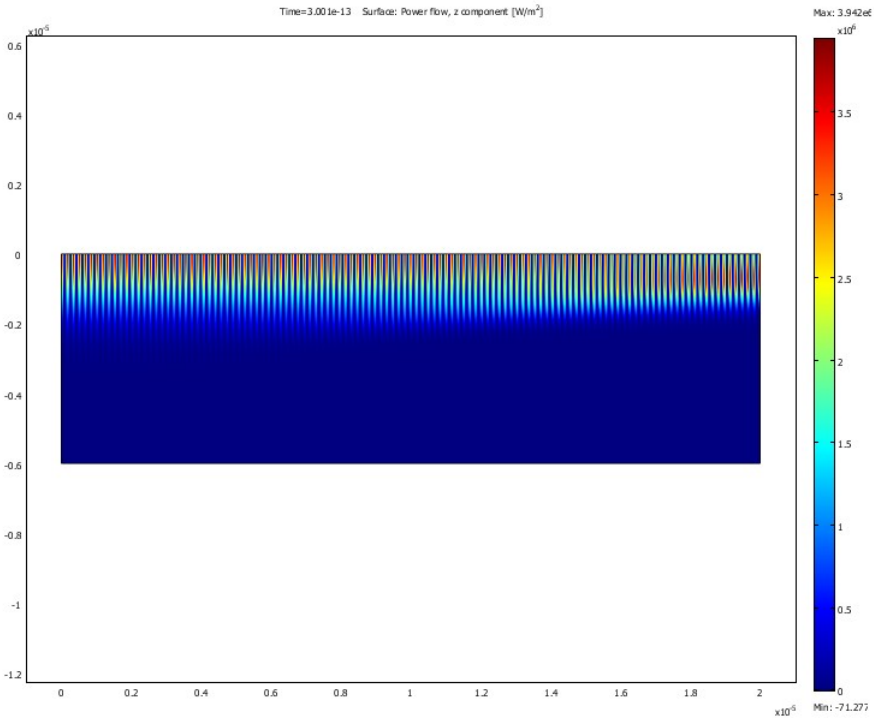

(j) $30\text{x}10^{-14}s$

Figure 4.3: Saturation power flow.

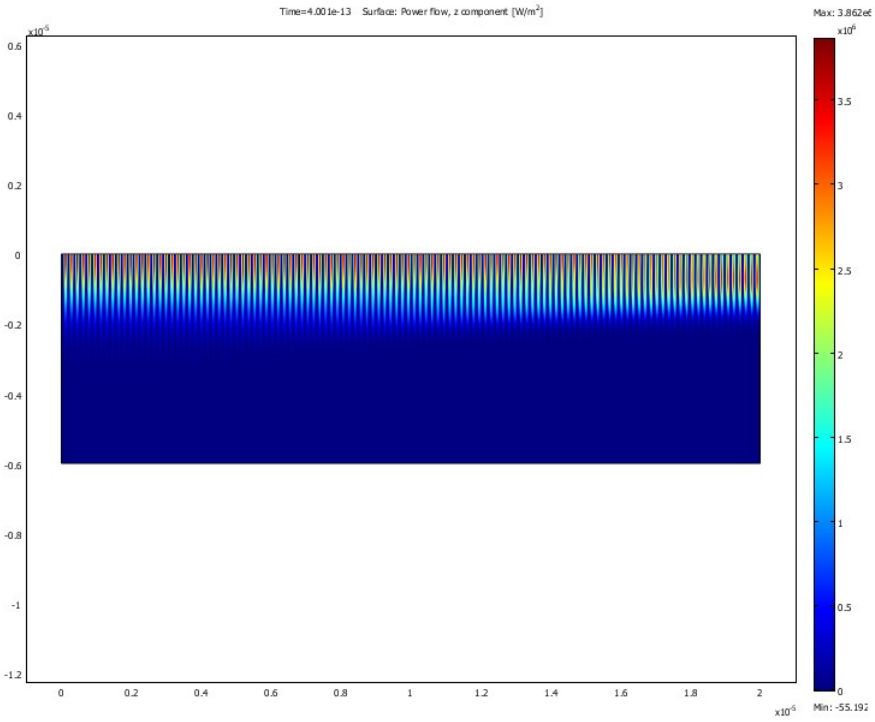

(k) $40\text{x}10^{-14}s$

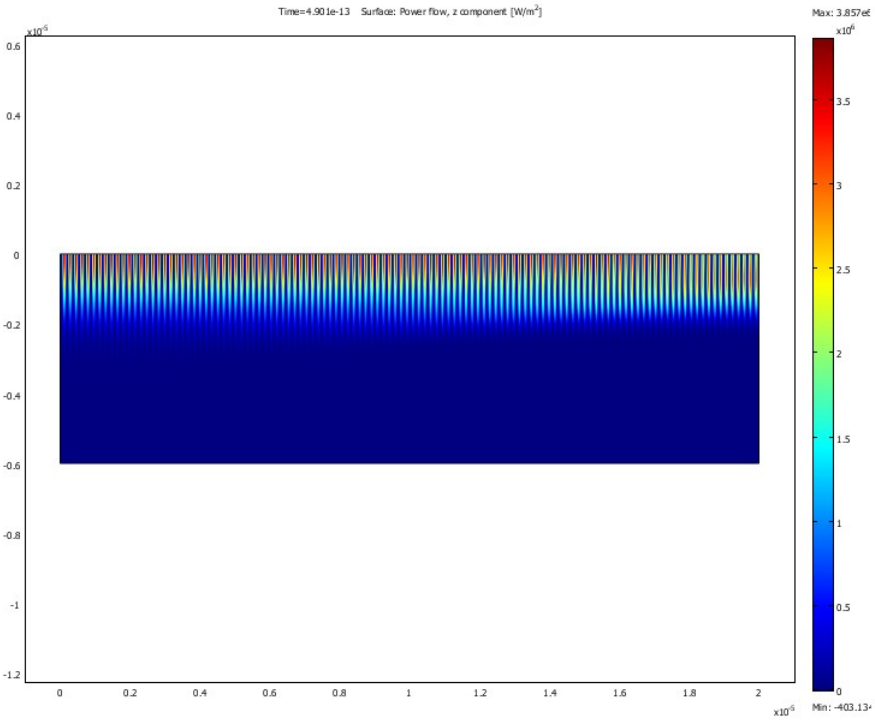

(l) $50\text{x}10^{-14}s$

Figure 4.3: Saturation power flow.

It can be seen that the self-focusing/self-trapping effect occurring in photopolymerization occurs on a much quicker time scale than the linear results, which is to be expected. Recall the saturation curves (figures **??**) from section 3.2 and the fact that there are three stages in this process. First there is the slow start to photopolymerization, this can be seen in figures 4.4 (a) and (b). The second stage is a rapid increase in refractive index due to a large amount of polymer chains being created from the light excitation. This second stage is seen in the results in figures 4.4 (c)-(f) where there is rapid propagation and increase in the index. Finally the third stage is the saturation stage, where the index of refraction is saturating and becoming uniform throughout the cured portion of the sample. Figures 4.4 (g)-(l) are indicative of this last stage of the photopolymerization process.

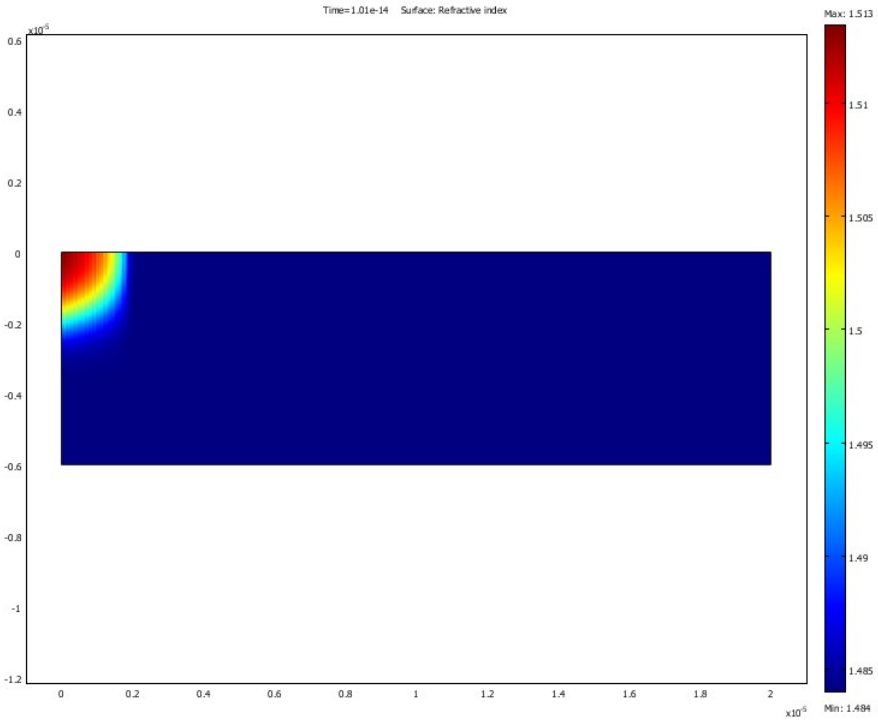

(a) $1\text{x}10^{-14}s$

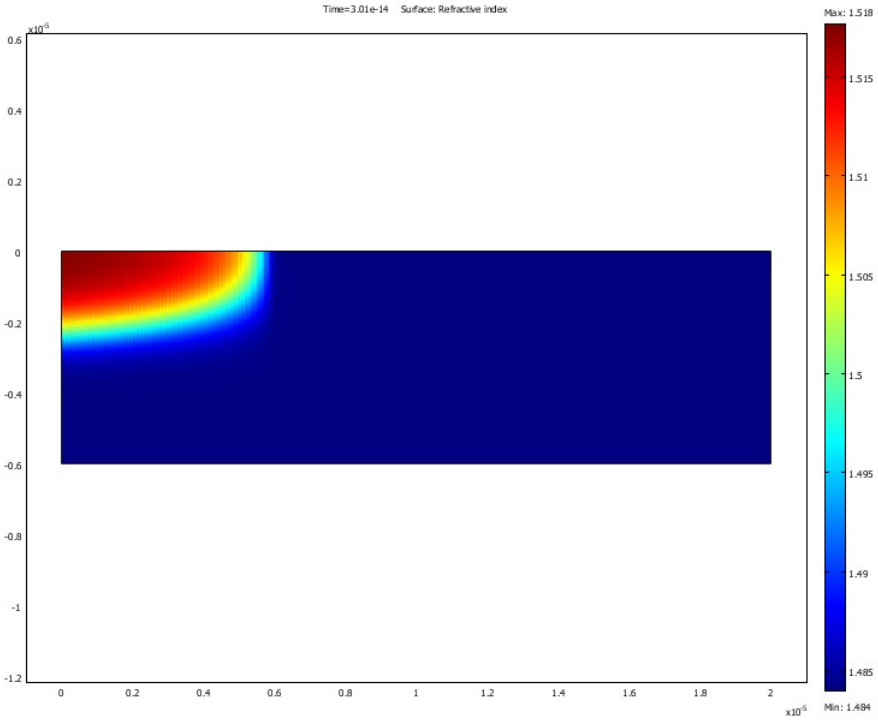

(b) $3\text{x}10^{-14}s$

Figure 4.4: Change in refractive index for saturation Δn.

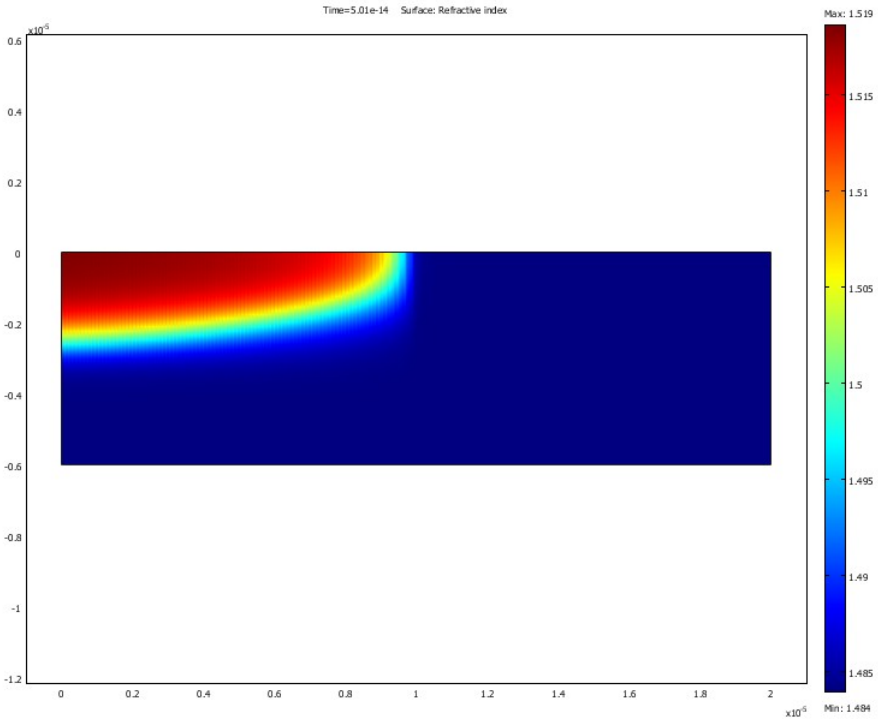

(c) $5\text{x}10^{-14}s$

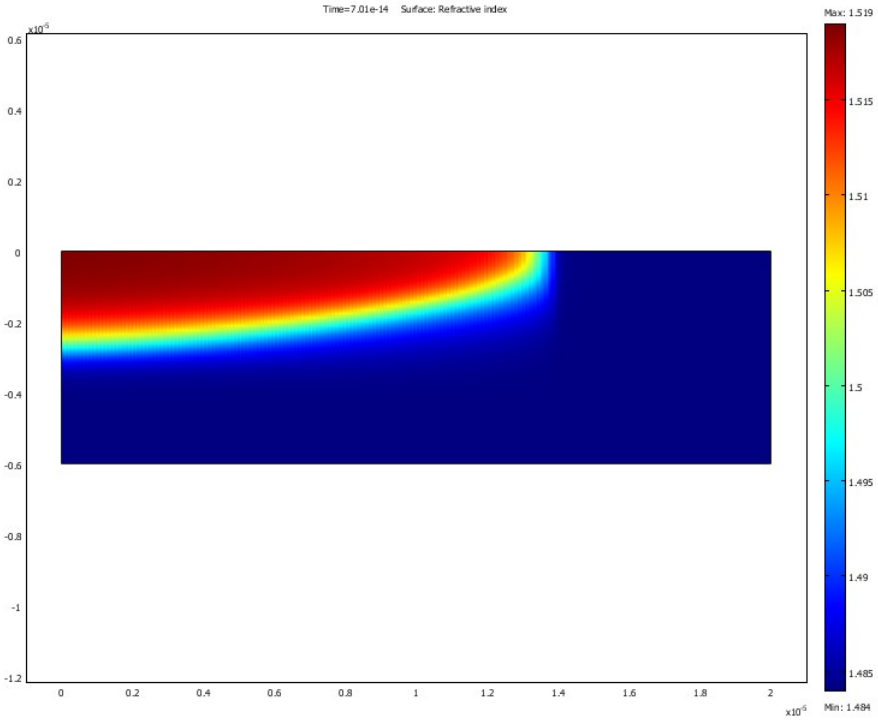

(d) $7\text{x}10^{-14}s$

Figure 4.4: Change in refractive index for saturation Δn.

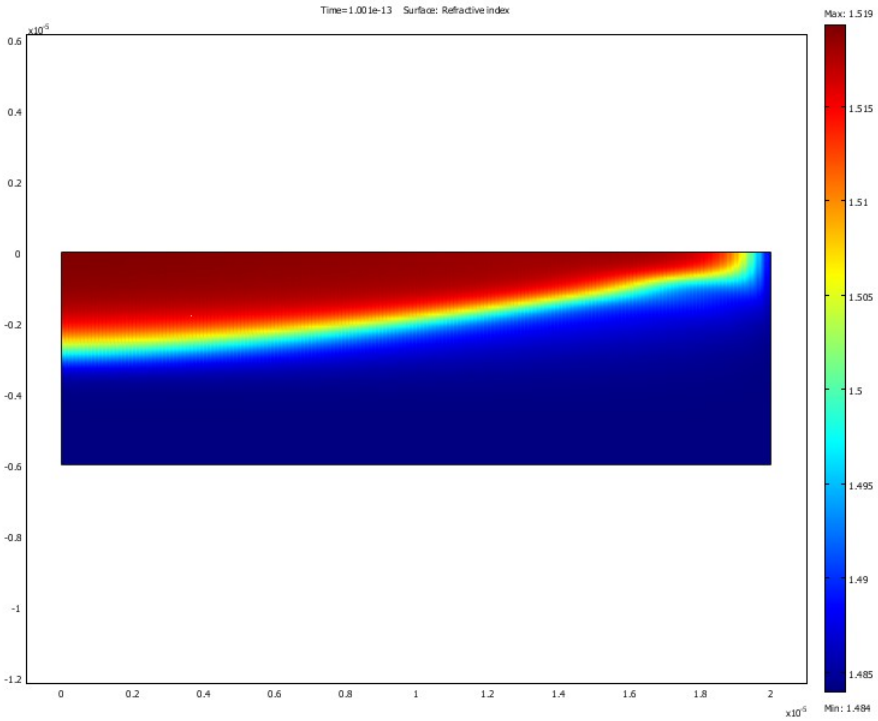

(e) $10\text{x}10^{-14}s$

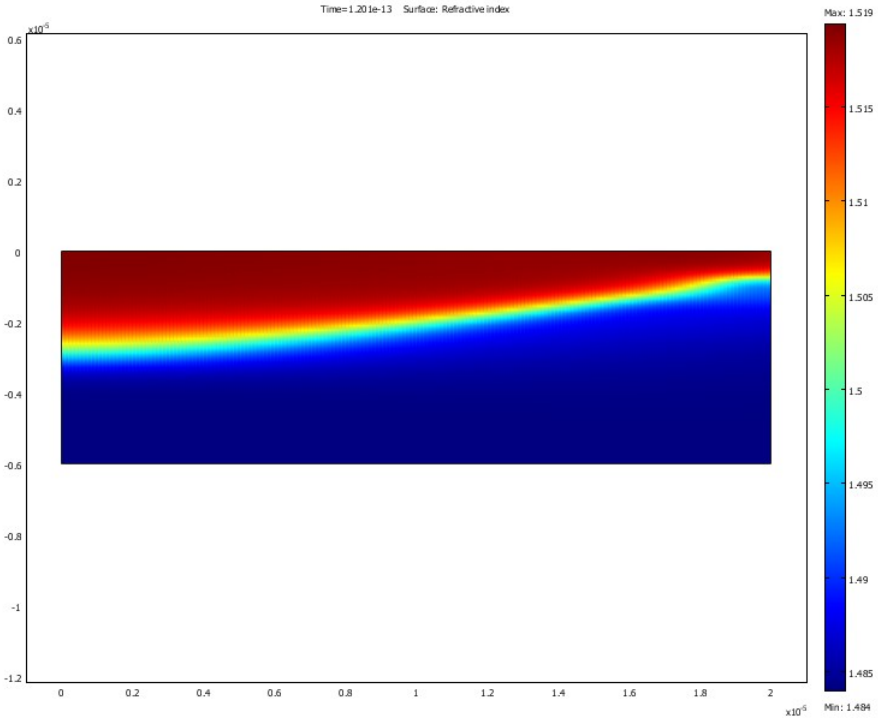

(f) $12\text{x}10^{-14}s$

Figure 4.4: Change in refractive index for saturation Δn.

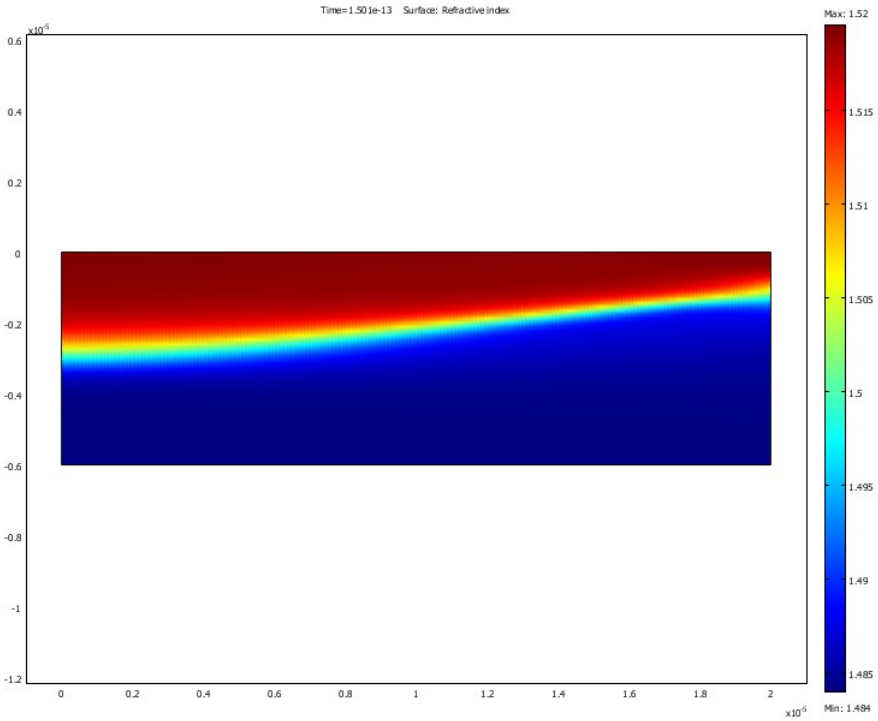

(g) $15\text{x}10^{-14}s$

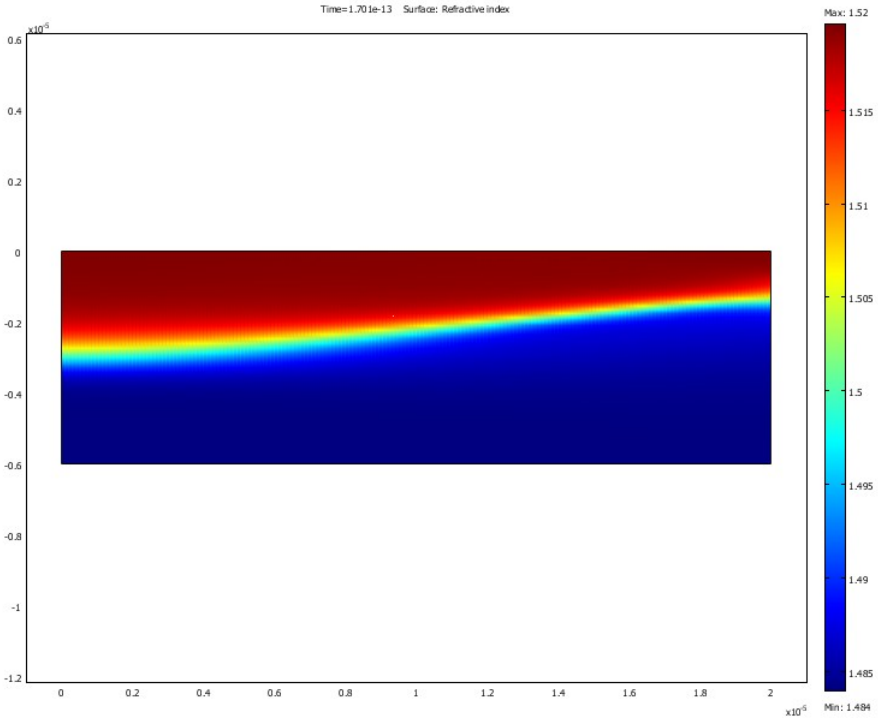

(h) $17\text{x}10^{-14}s$

Figure 4.4: Change in refractive index for saturation Δn.

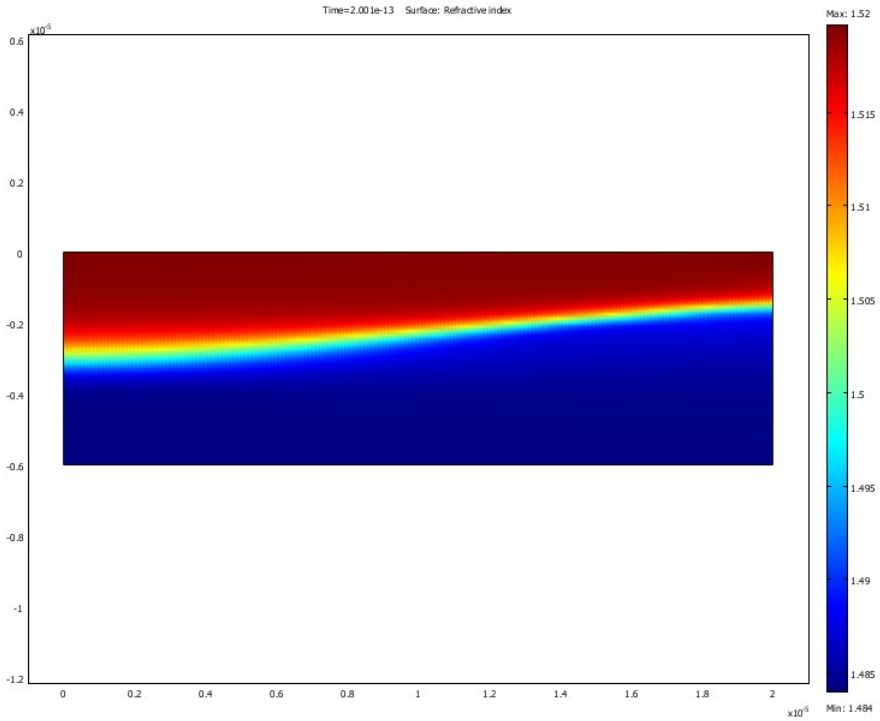

(i) $20\text{x}10^{-14}s$

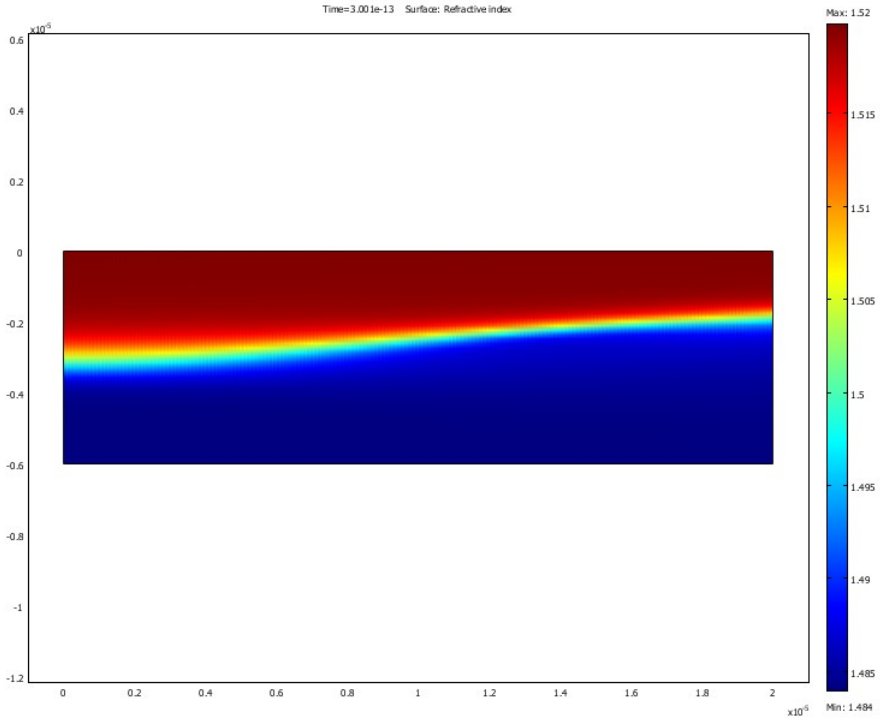

(j) $30\text{x}10^{-14}s$

Figure 4.4: Change in refractive index for saturation Δn.

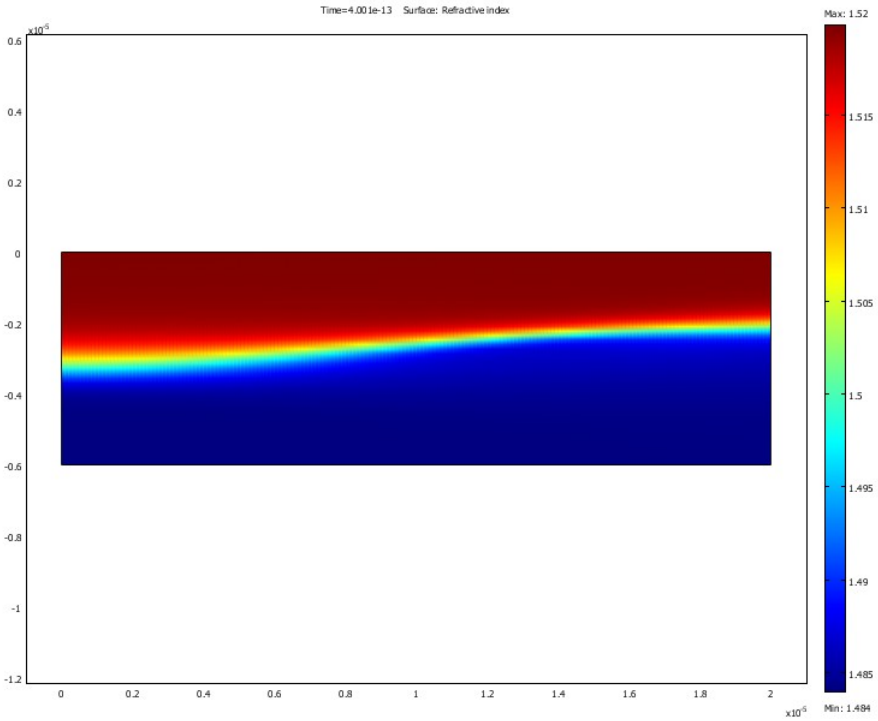

(k) $40\text{x}10^{-14}s$

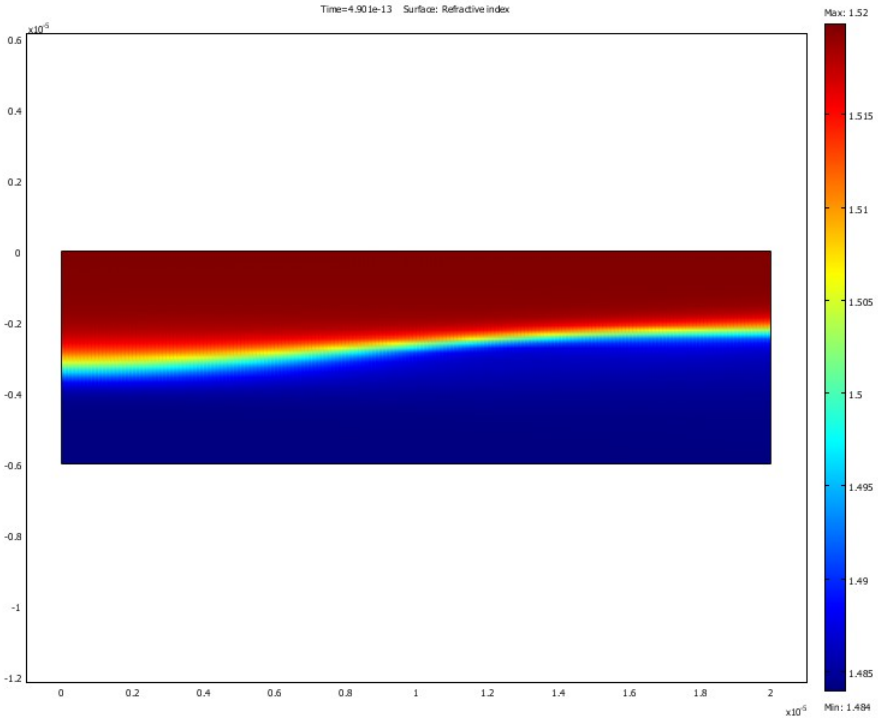

(l) $50\text{x}10^{-14}s$

Figure 4.4: Change in refractive index for saturation Δn.

4.3 Density Results

To simulate the change in density, we added a body force to the previous saturation model by relating it to the polymerization rate equation given by equations (3.17) and (3.21). The parameters defined in table 4.3 were added to those given in table 4.2 to fully define the photopolymerization process. Two separate cases were simulated as explained in section 3.5.

Table 4.3: Parameters for change in density

Variable	**Value**	**Units**
F_0	13x10^9	N
E	1x10^{12}	Pa
ρ	1231	kg/m^3
ν	0	–

4.3.1 Case 1: Single Fiber

For the first case study of a single fiber impinging UV light into an epoxy resin, the boundaries $z = 0$ and $r = 0$ were constrained in the z-direction and the r-direction respectively. Figures 4.5 (a)-(l) plot the results of the power flow for this case. Once again we see the early onset of the self-focusing at time t = 5x10^{-14}s and full propagation by time t = 12x10^{-14}s. However, we have also plotted the change in density by superimposing the power flow on the deformed geometry for each time step. Note that the deformations of the cross-section for each graph in figure 4.5 are not to scale, they are exaggerated to demonstrate the effect. The greatest change in density occurs in the z-direction with the largest deformation occurring along the propagation axis where the resin is being cured. This is the expected result, which is the same effect that has been seen experimentally.

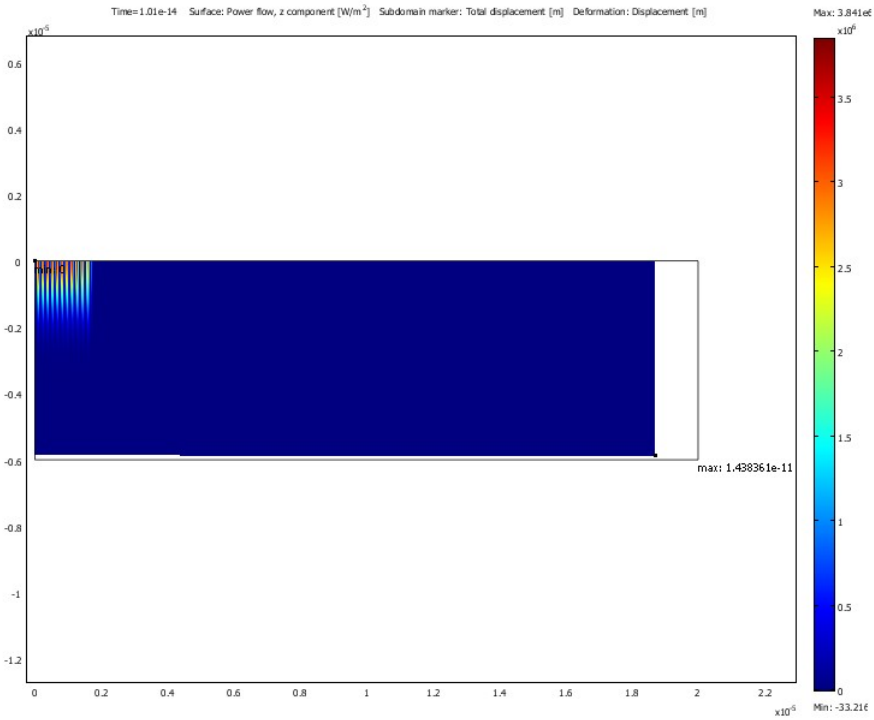

(a) $1\text{x}10^{-14}s$

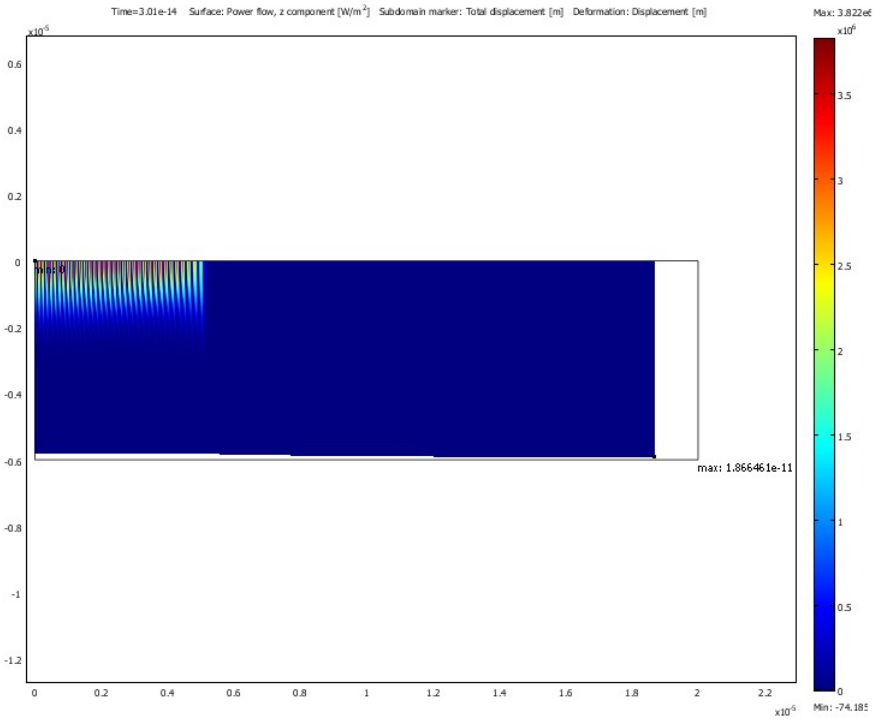

(b) $3\text{x}10^{-14}s$

Figure 4.5: Saturation power flow with change in density for single fiber system.

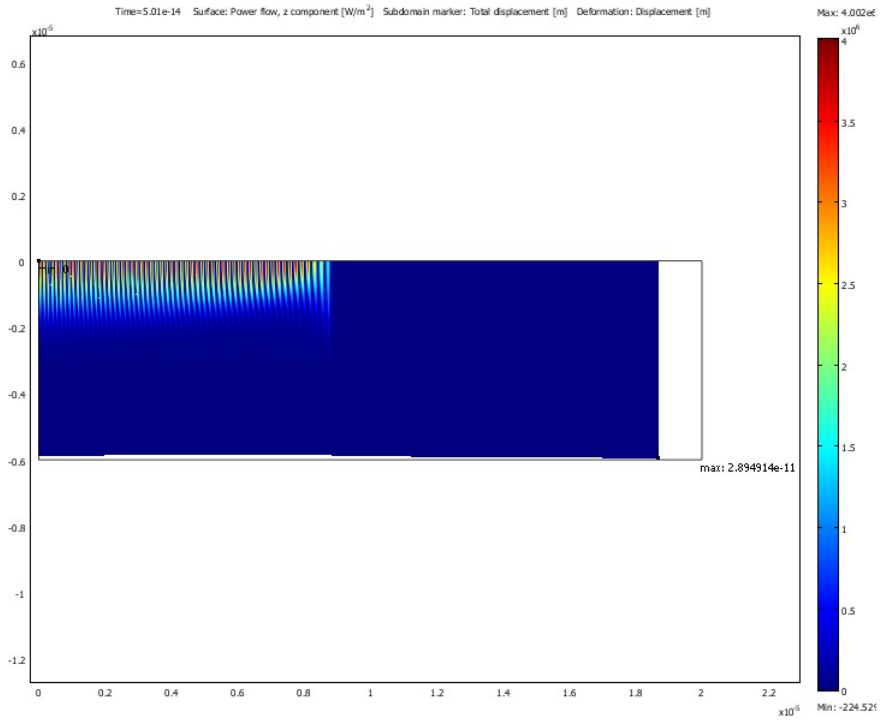

(c) $5\text{x}10^{-14}s$

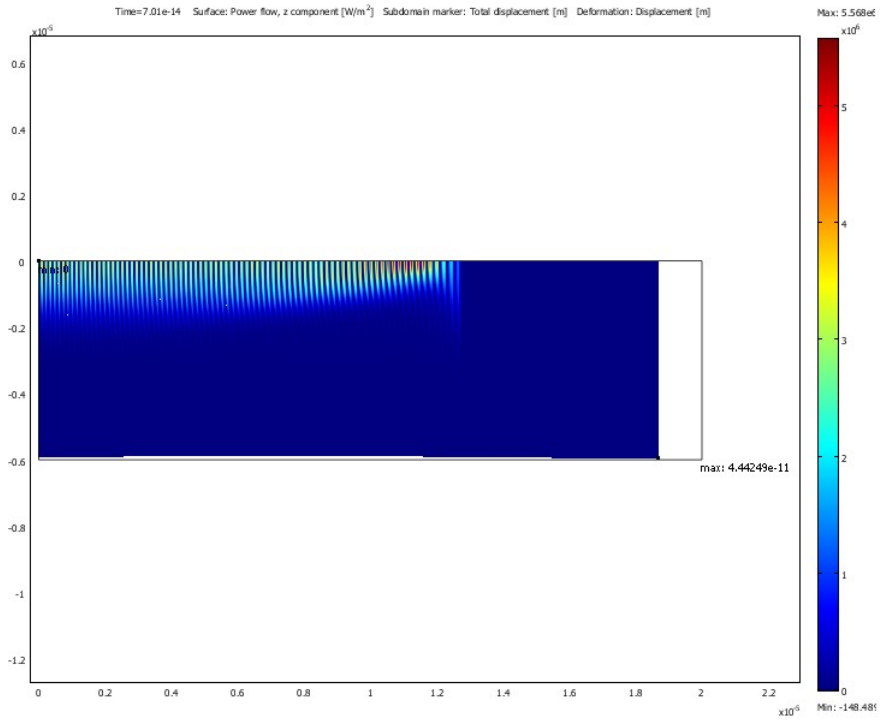

(d) $7\text{x}10^{-14}s$

Figure 4.5: Saturation power flow with change in density for single fiber system.

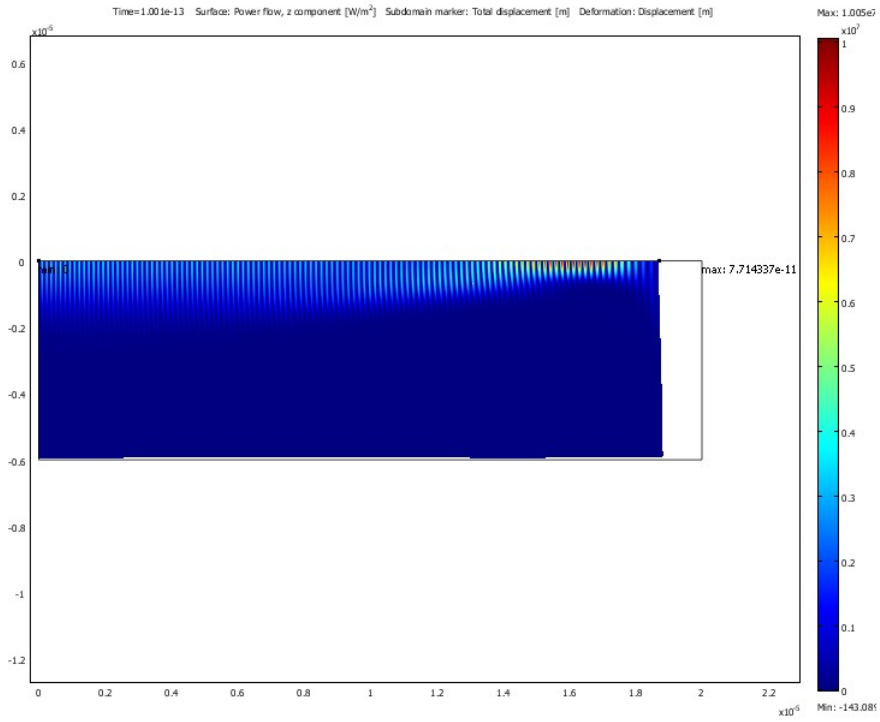

(e) $10\text{x}10^{-14}s$

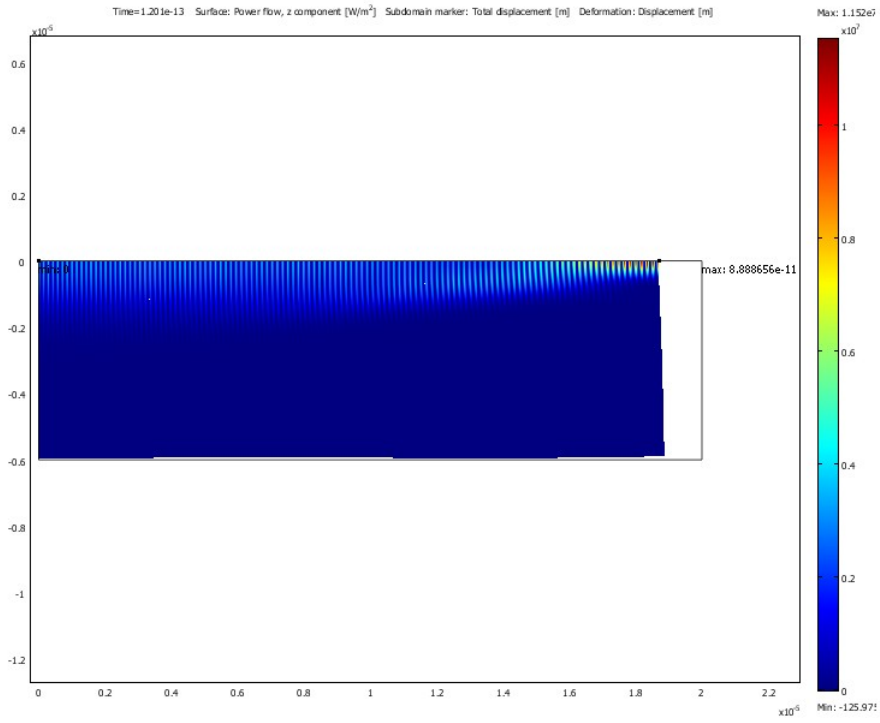

(f) $12\text{x}10^{-14}s$

Figure 4.5: Saturation power flow with change in density for single fiber system.

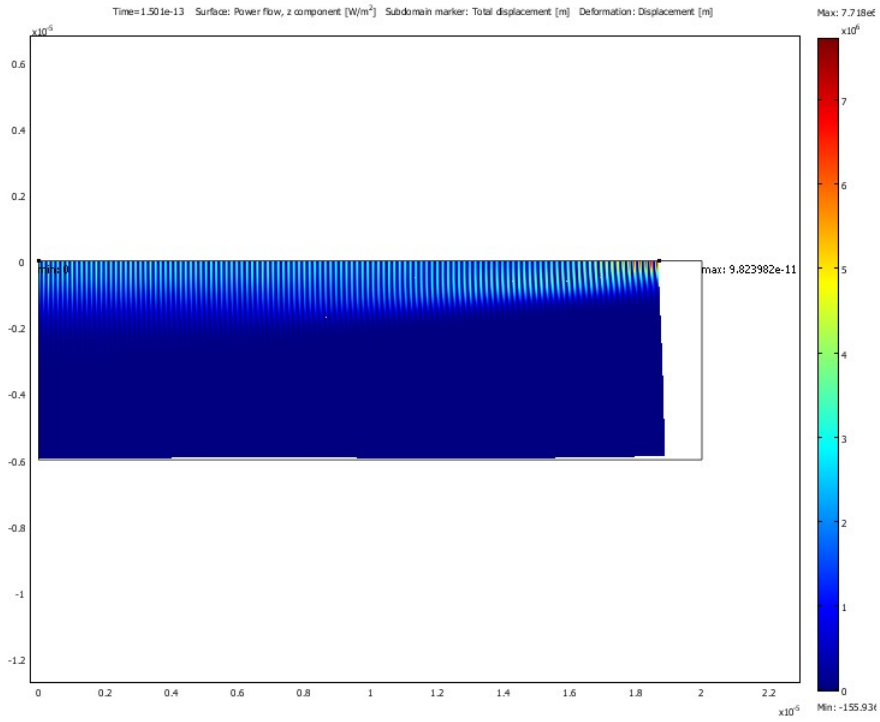

(g) $15\text{x}10^{-14}s$

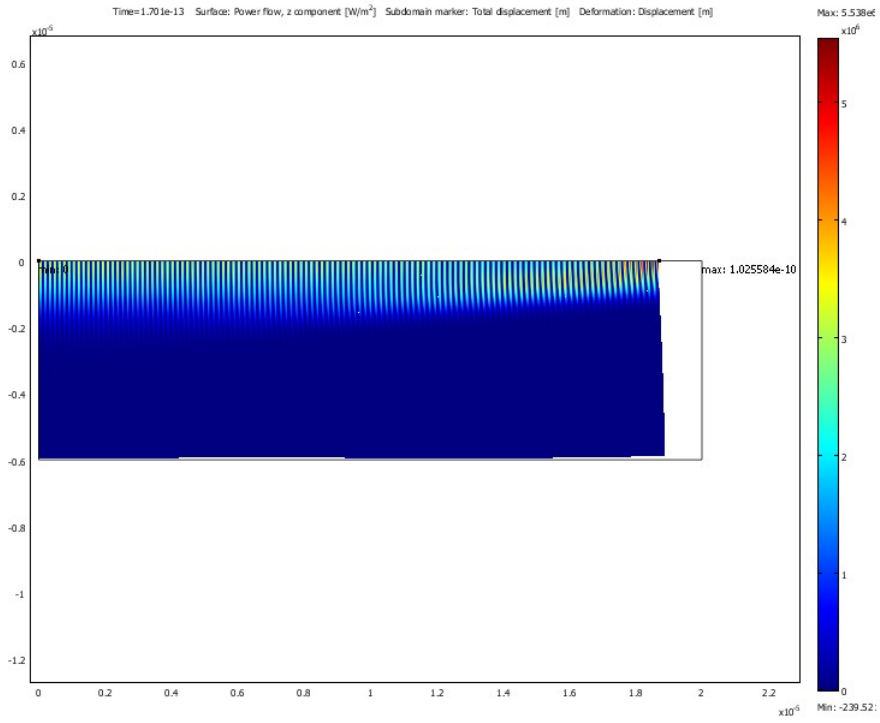

(h) $17\text{x}10^{-14}s$

Figure 4.5: Saturation power flow with change in density for single fiber system.

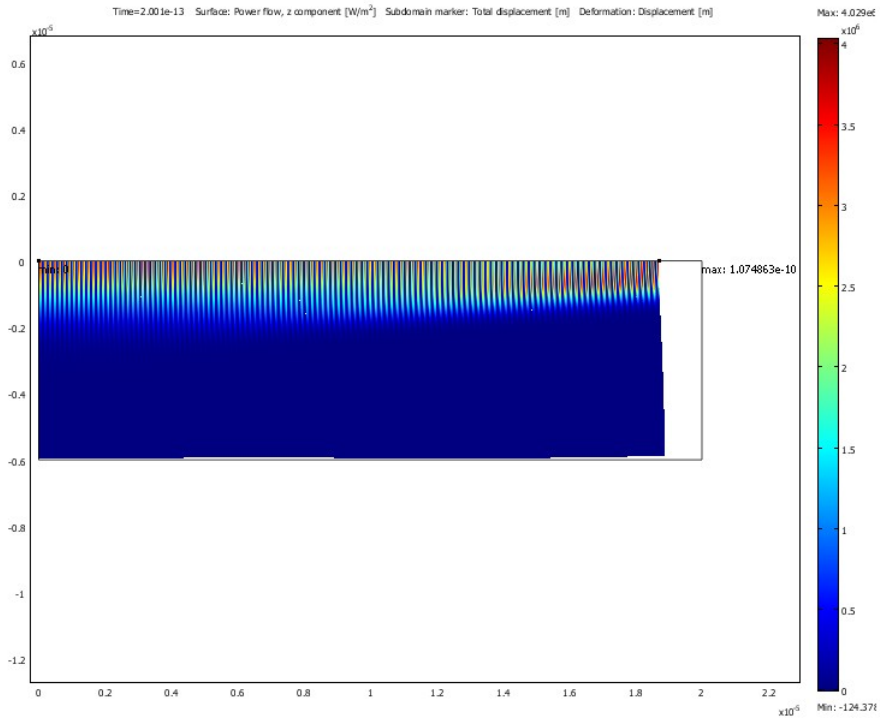

(i) $20\text{x}10^{-14}s$

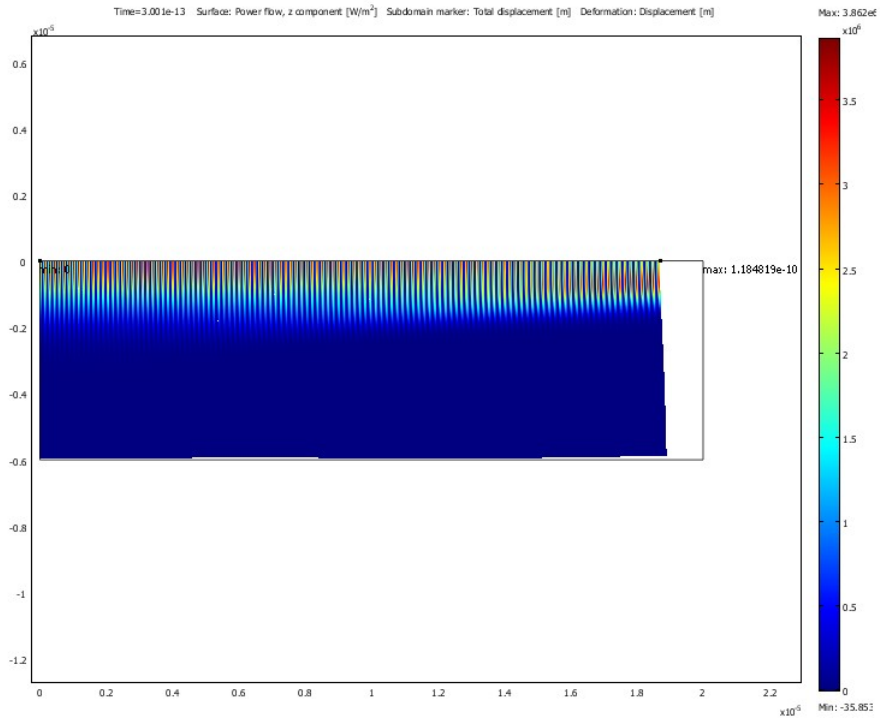

(j) $30\text{x}10^{-14}s$

Figure 4.5: Saturation power flow with change in density for single fiber system.

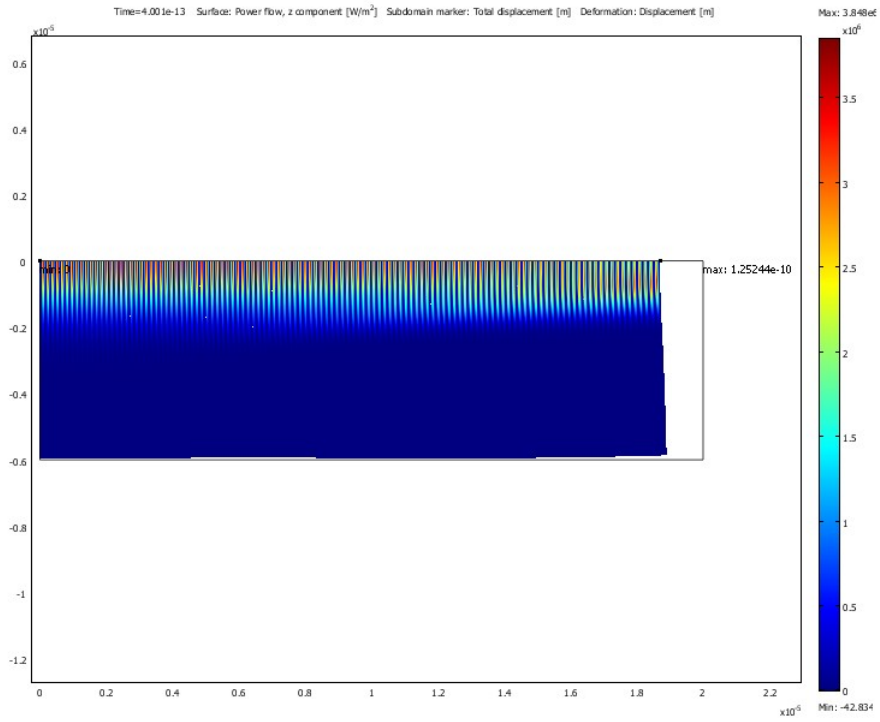

(k) $40\text{x}10^{-14}s$

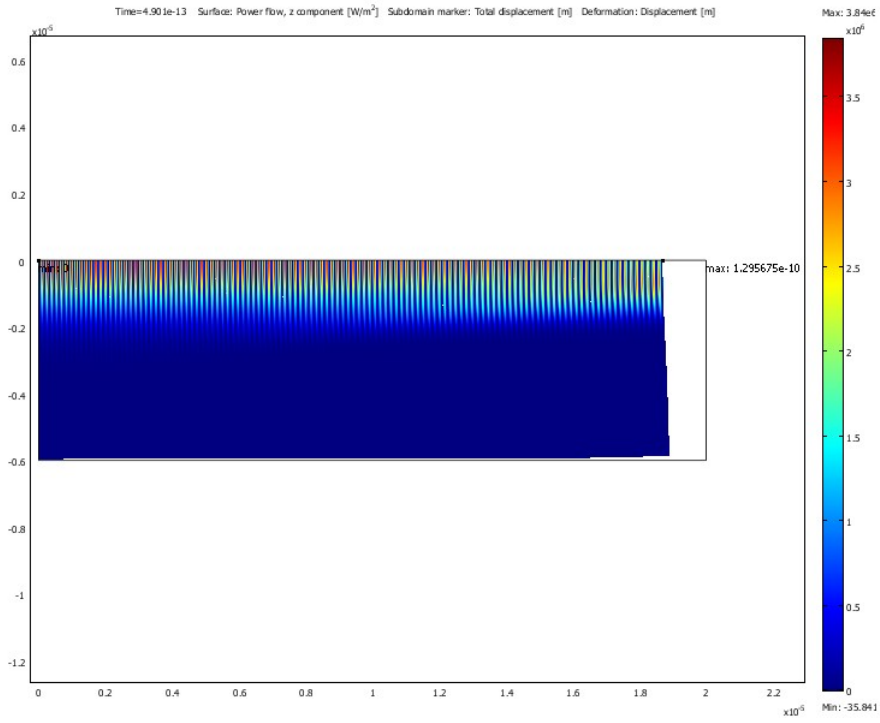

(l) $50\text{x}10^{-14}s$

Figure 4.5: Saturation power flow with change in density for single fiber system.

Figures 4.6 (a)-(l) plot the index of refraction distribution superimposed on the deformed geometry for the same time steps as figure 4.5. Once again we see the saturation effects similar to those of the previous model.

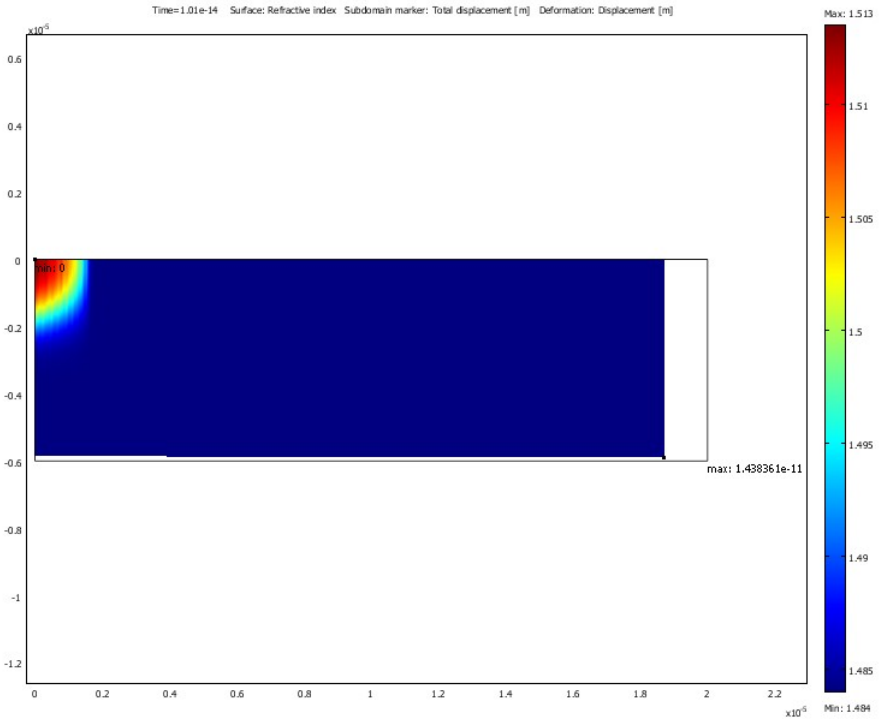

(a) $1\text{x}10^{-14}s$

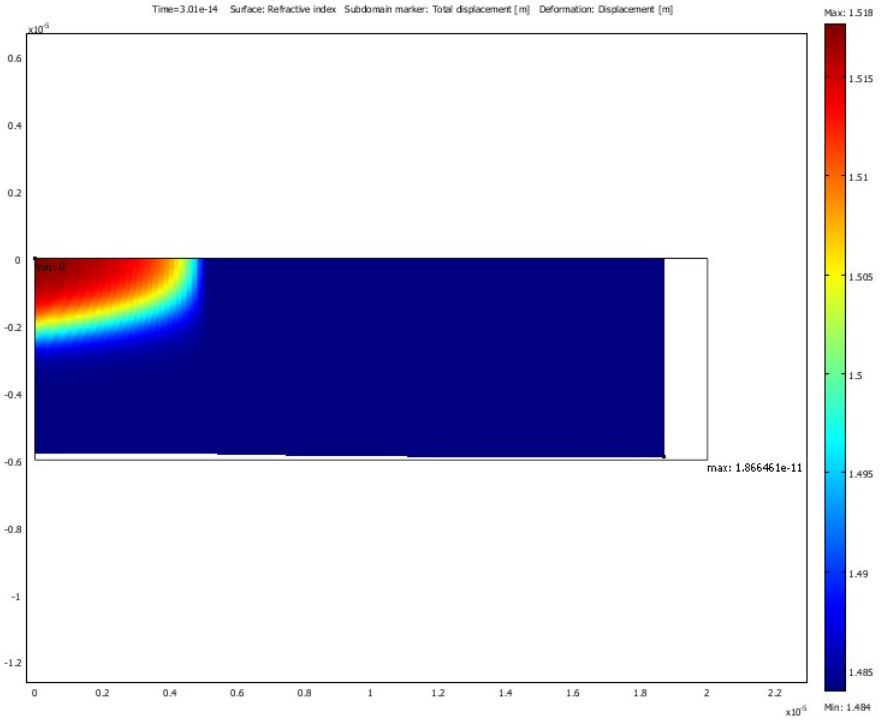

(b) $3\text{x}10^{-14}s$

Figure 4.6: Change in refractive index for saturation Δn with change in density for single fiber system.

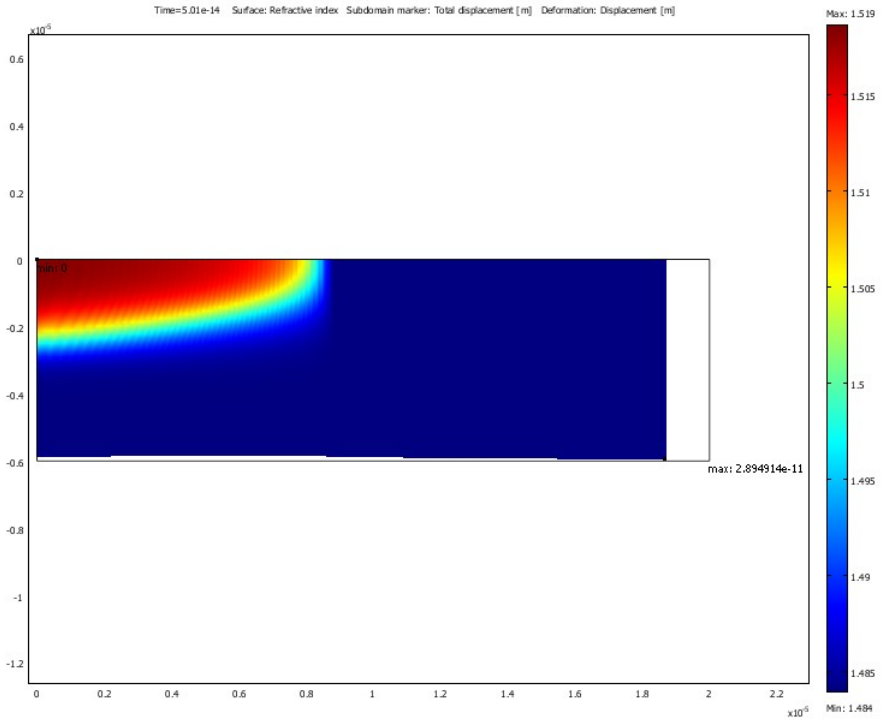

(c) $5\text{x}10^{-14}s$

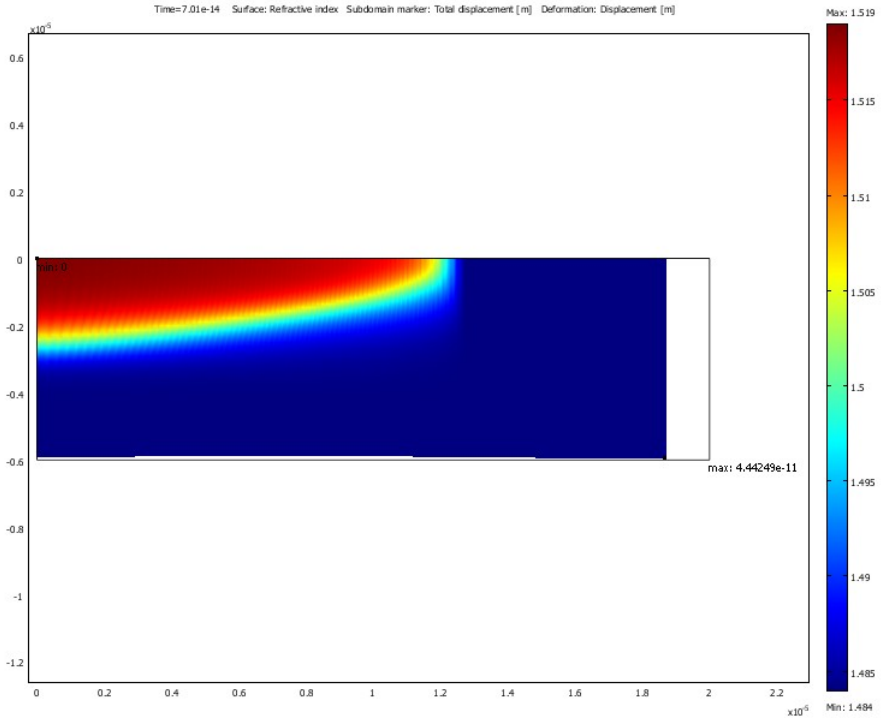

(d) $7\text{x}10^{-14}s$

Figure 4.6: Change in refractive index for saturation Δn with change in density for single fiber system.

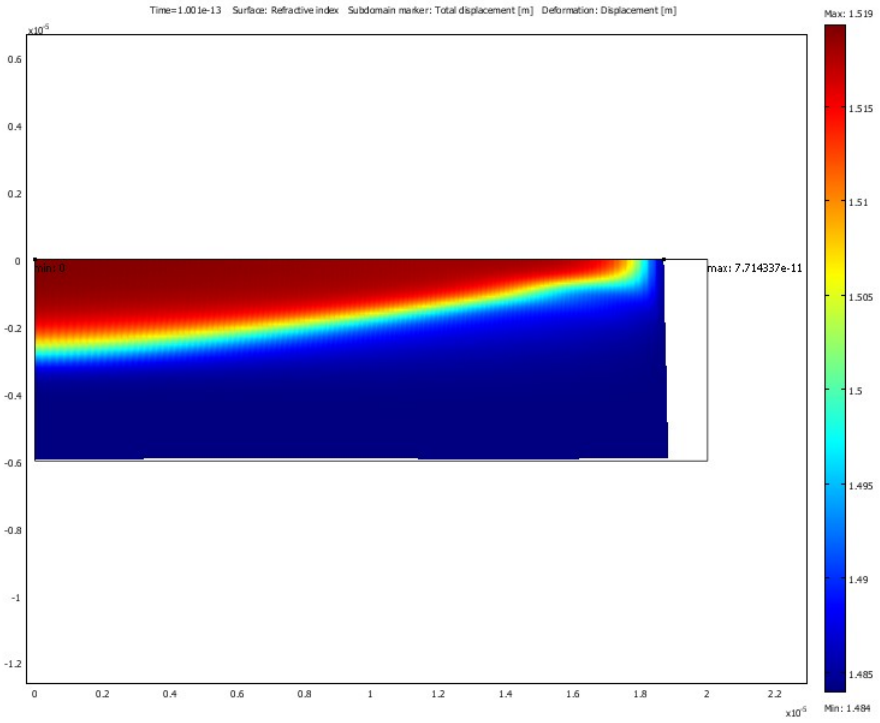

(e) $10\text{x}10^{-14}s$

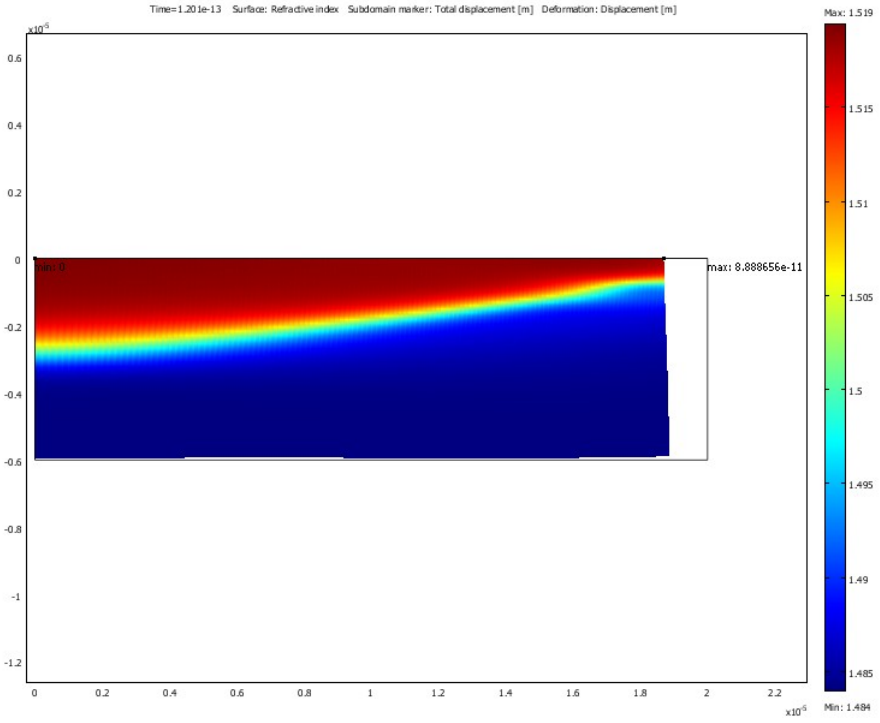

(f) $12\text{x}10^{-14}s$

Figure 4.6: Change in refractive index for saturation Δn with change in density for single fiber system.

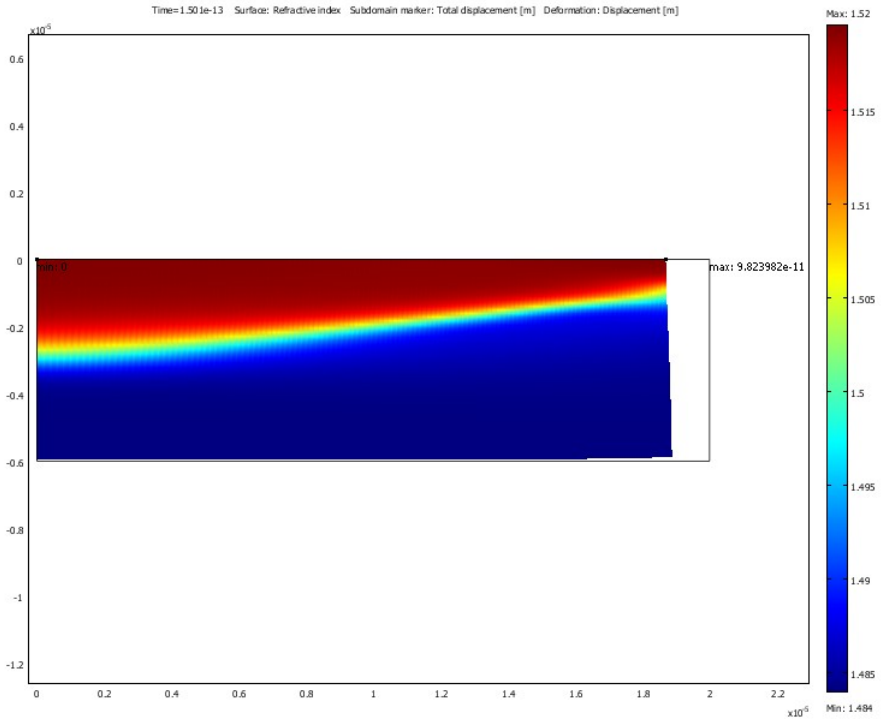

(g) $15\text{x}10^{-14}s$

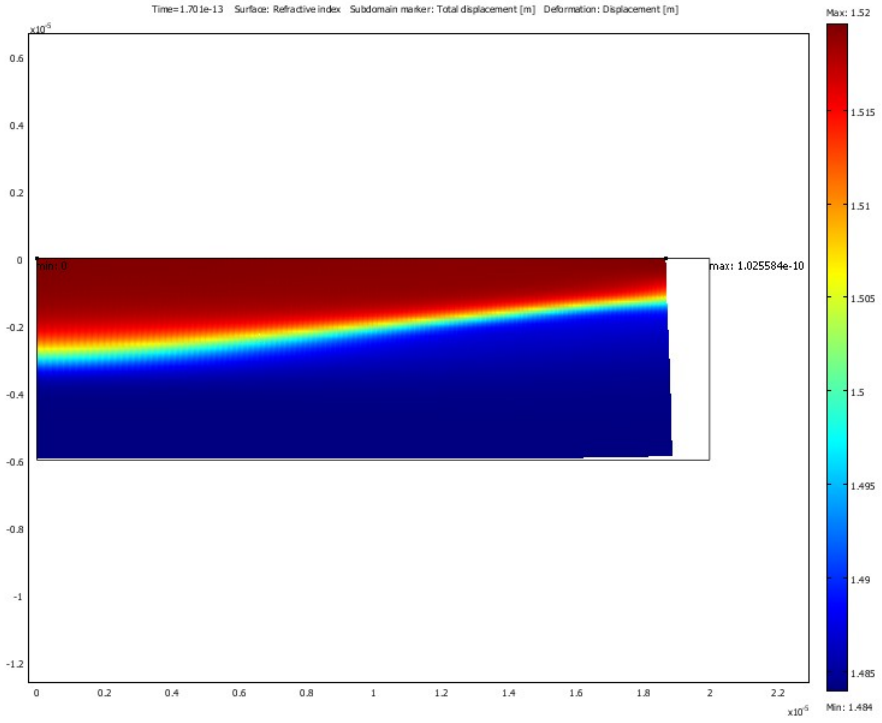

(h) $17\text{x}10^{-14}s$

Figure 4.6: Change in refractive index for saturation Δn with change in density for single fiber system.

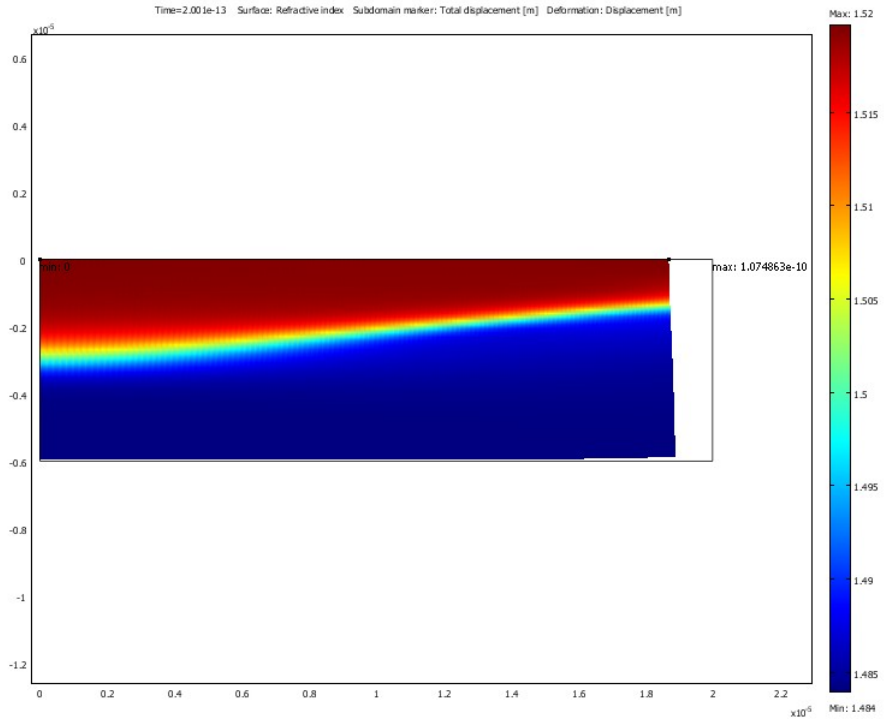

(i) $20\text{x}10^{-14}s$

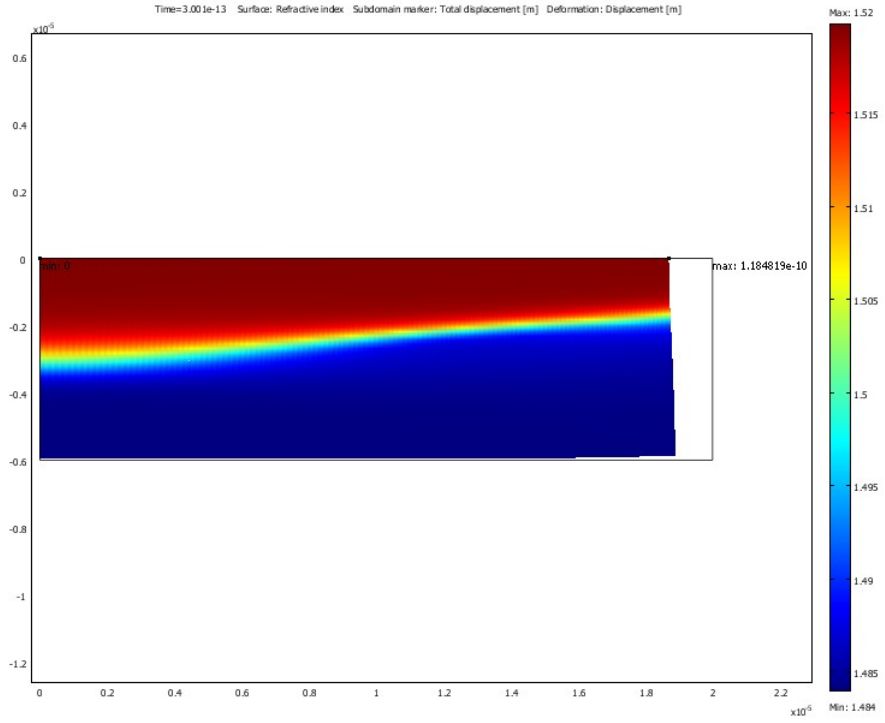

(j) $30\text{x}10^{-14}s$

Figure 4.6: Change in refractive index for saturation Δn with change in density for single fiber system.

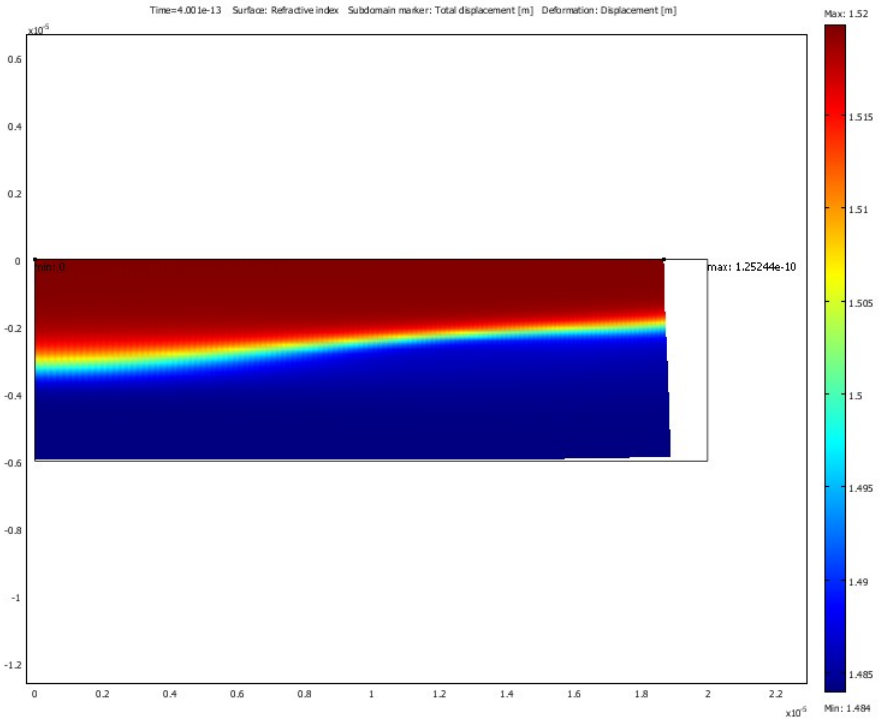

(k) $40\text{x}10^{-14}s$

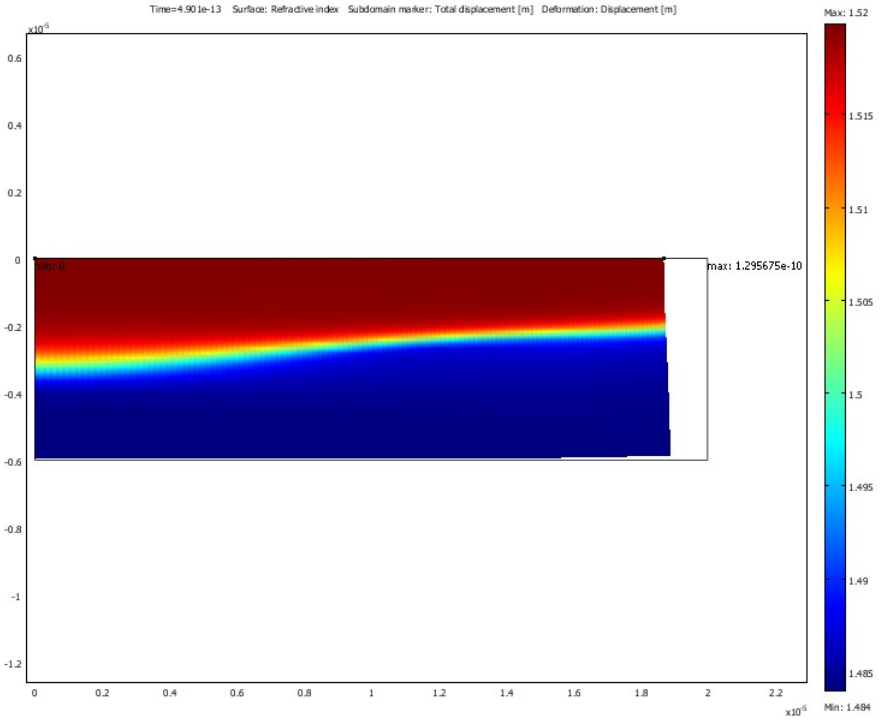

(l) $50\text{x}10^{-14}s$

Figure 4.6: Change in refractive index for saturation Δn with change in density for single fiber system.

4.3.2 Case 2: Double Fiber

The final case study was the case with two fibers aligned with a small gap between them filled with resin. The left and right boundaries were constrained in the z-direction and the top was constrained in the r-direction.

Notice the effect of confining particular boundaries does not change the propagation of the lightwave, so we see the same effects in the power flow in figures 4.7 (a)-(l) as have been seen before. The biggest change with this series of graphs is how the resin is changing shape. Due to three of the four boundaries being constrained, we are seeing a radial contraction at the bottom edge of the sample where the density of the middle of the resin has changed the most causing the most contraction to be seen at the bottom of the sample. This result is coincides with the experimental formation of a polymer sensing element between two fibers as demonstrated by Huang (figure 2.8).

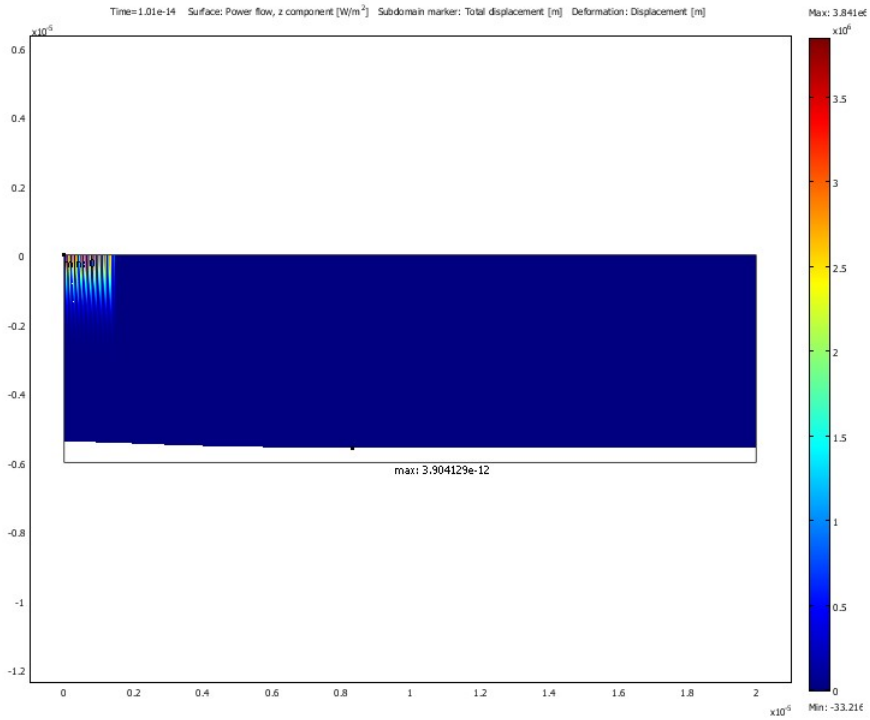

(a) $1x10^{-14}s$

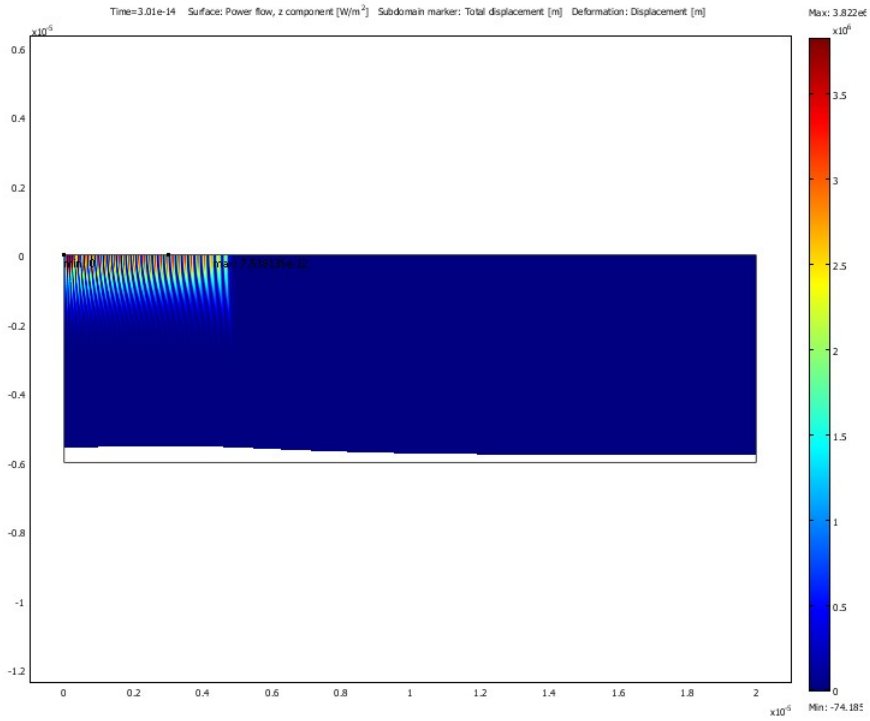

(b) $3x10^{-14}s$

Figure 4.7: Saturation power flow with change in density for double fiber system.

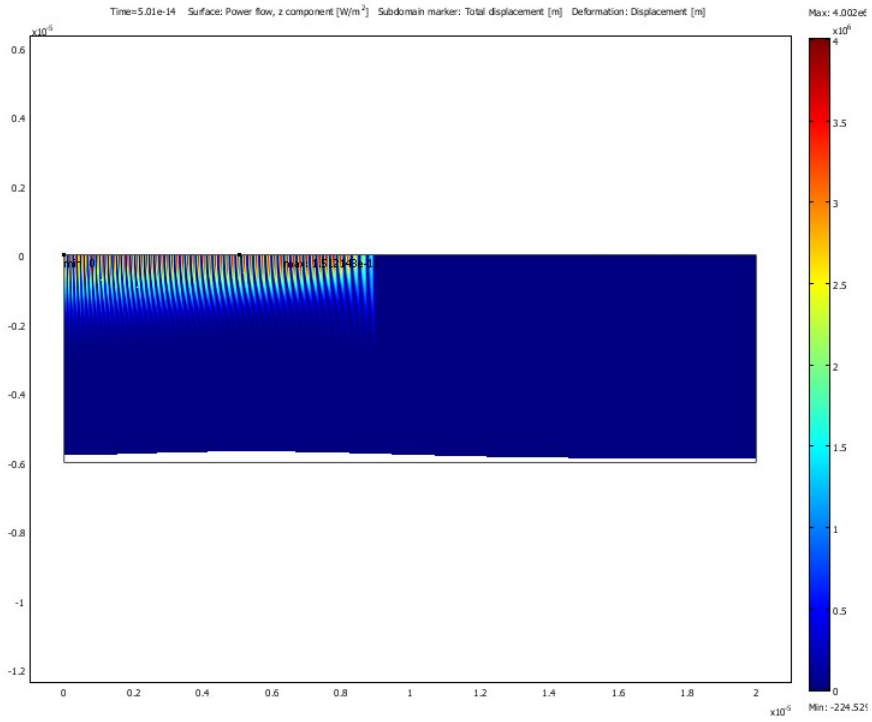

(c) $5\text{x}10^{-14}s$

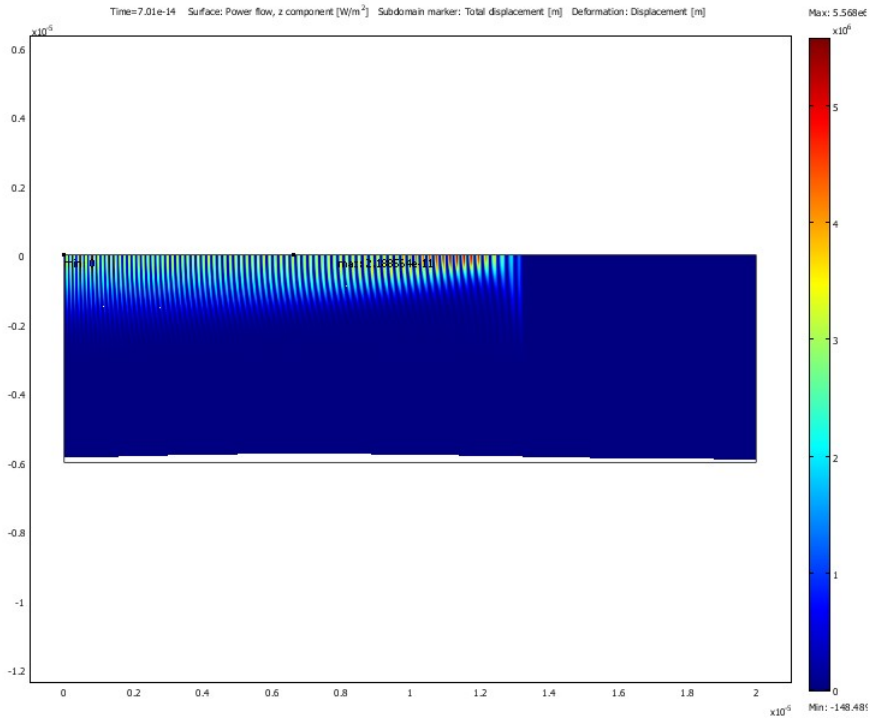

(d) $7\text{x}10^{-14}s$

Figure 4.7: Saturation power flow with change in density for double fiber system.

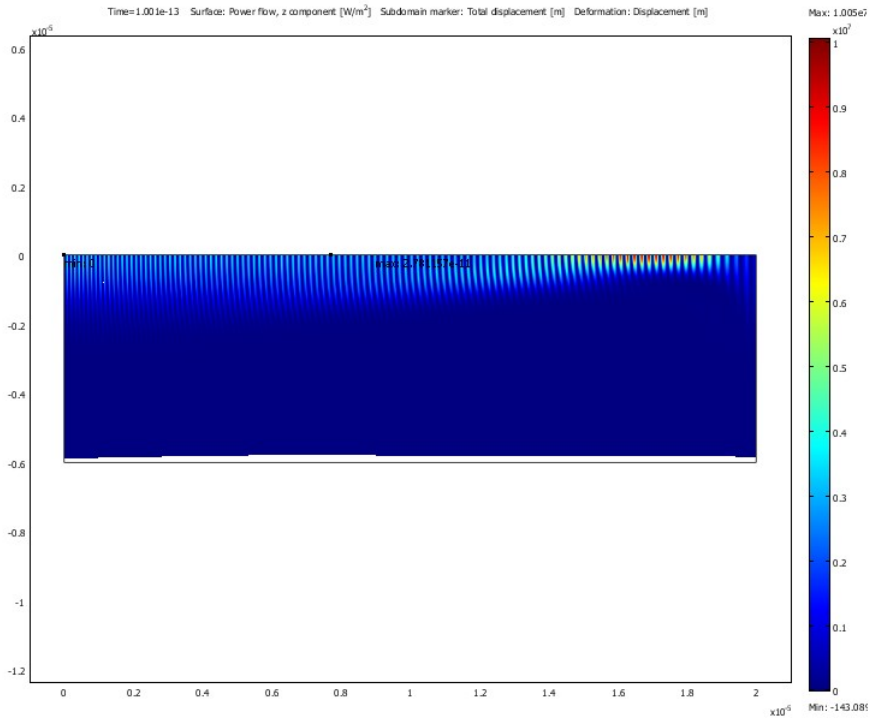

(e) $10\text{x}10^{-14}s$

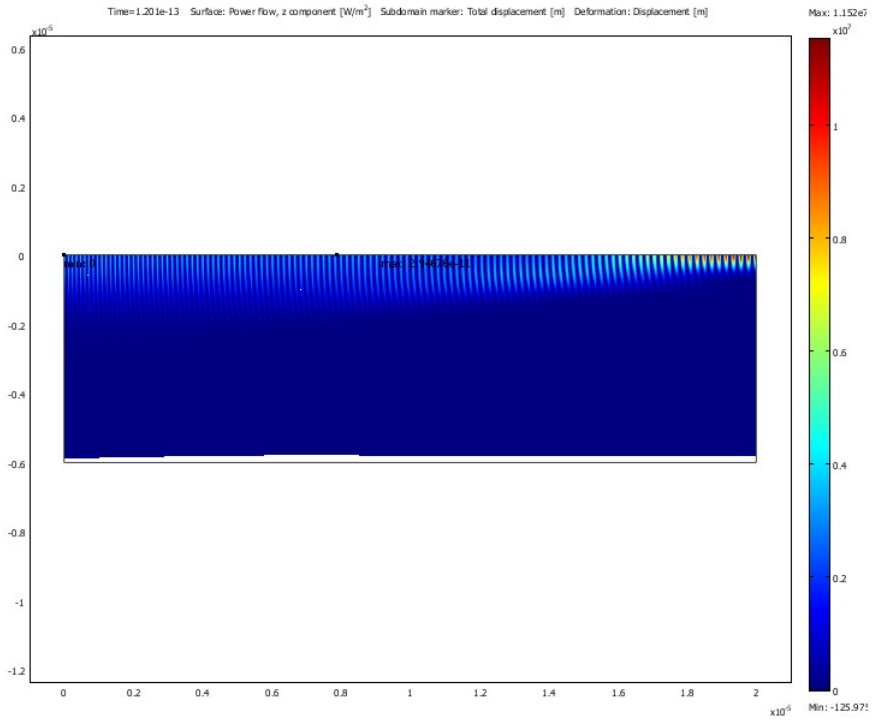

(f) $12\text{x}10^{-14}s$

Figure 4.7: Saturation power flow with change in density for double fiber system.

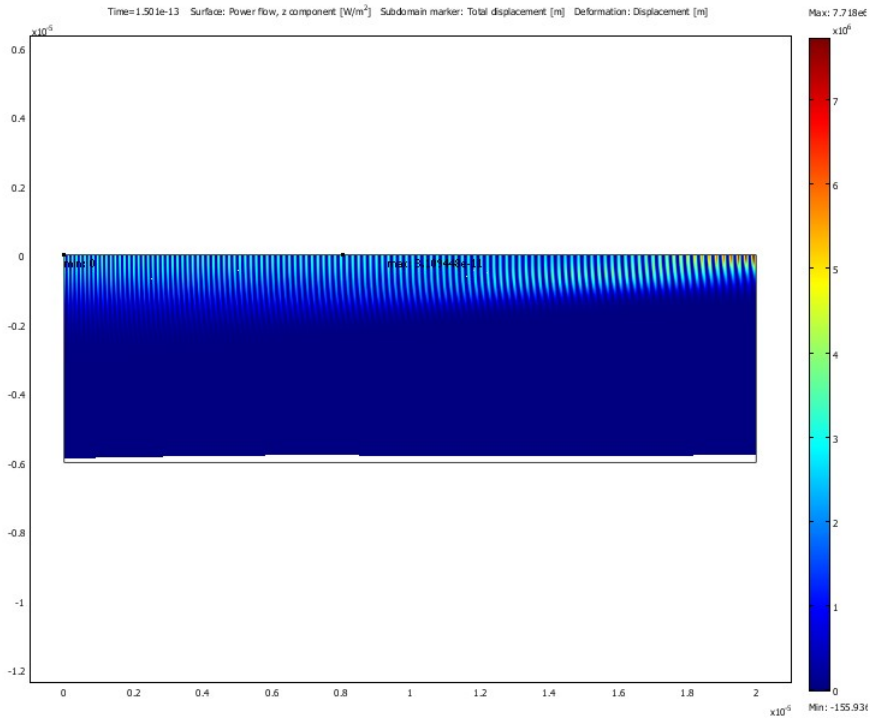

(g) $15\text{x}10^{-14}s$

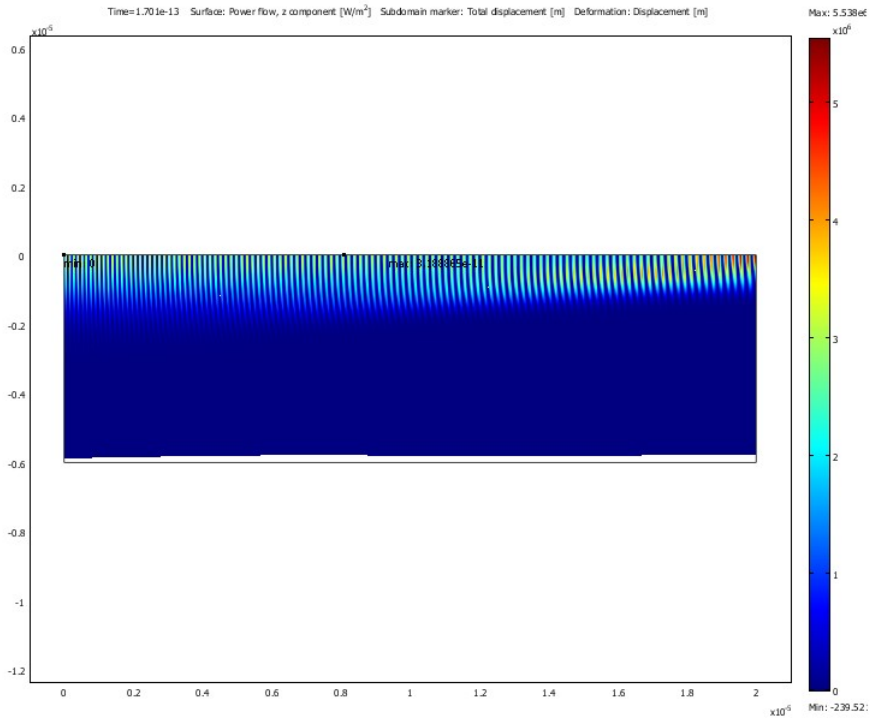

(h) $17\text{x}10^{-14}s$

Figure 4.7: Saturation power flow with change in density for double fiber system.

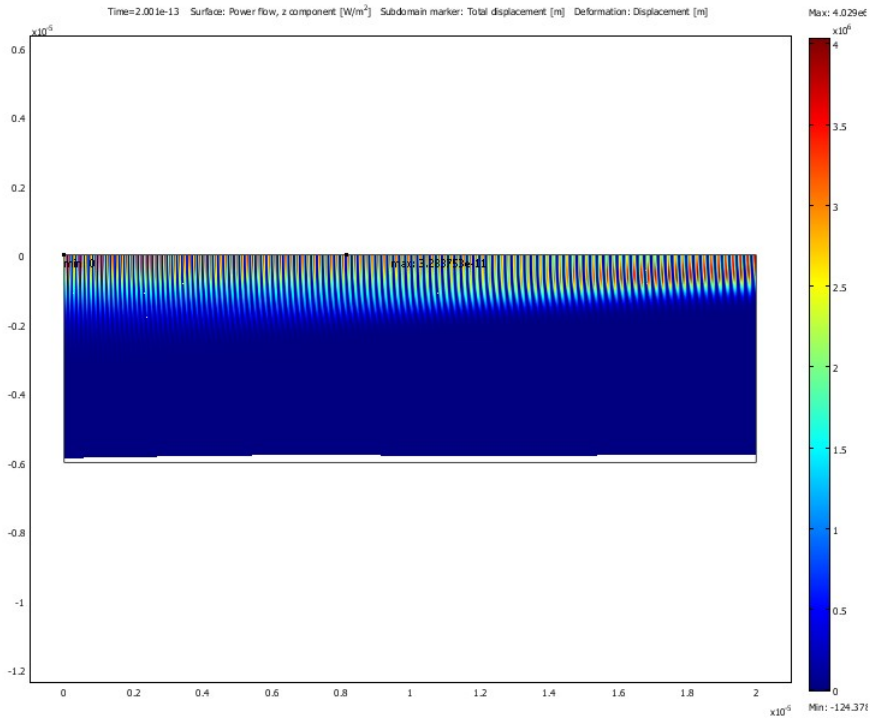

(i) $20\text{x}10^{-14}s$

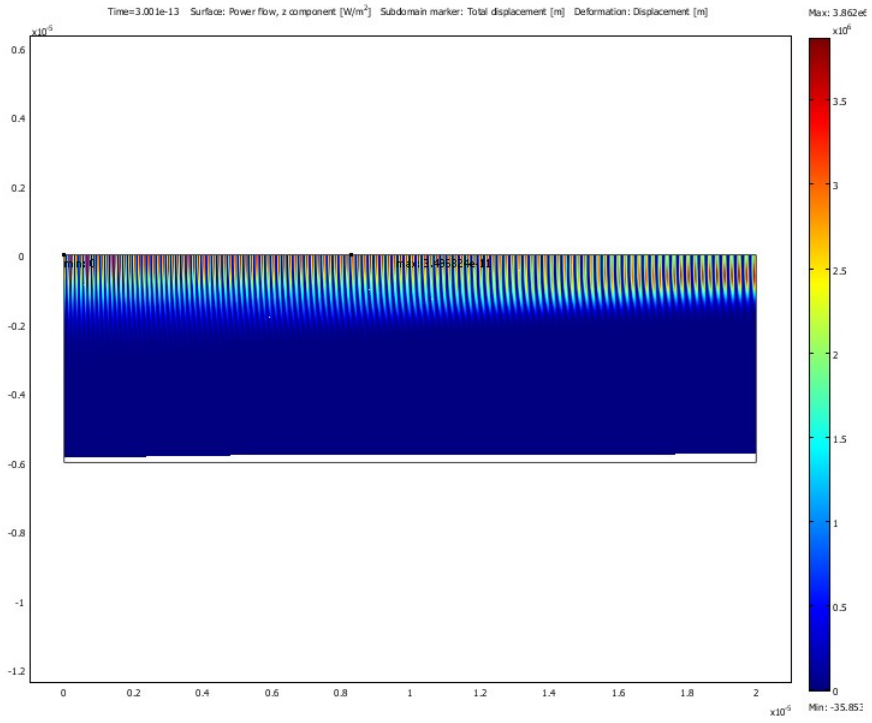

(j) $30\text{x}10^{-14}s$

Figure 4.7: Saturation power flow with change in density for double fiber system.

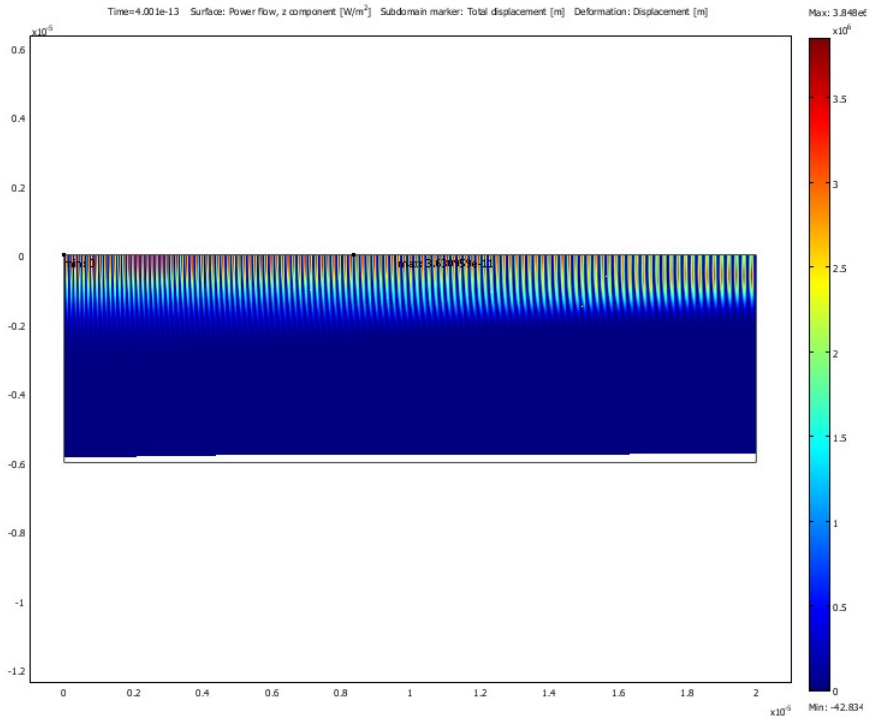

(k) $40\text{x}10^{-14}s$

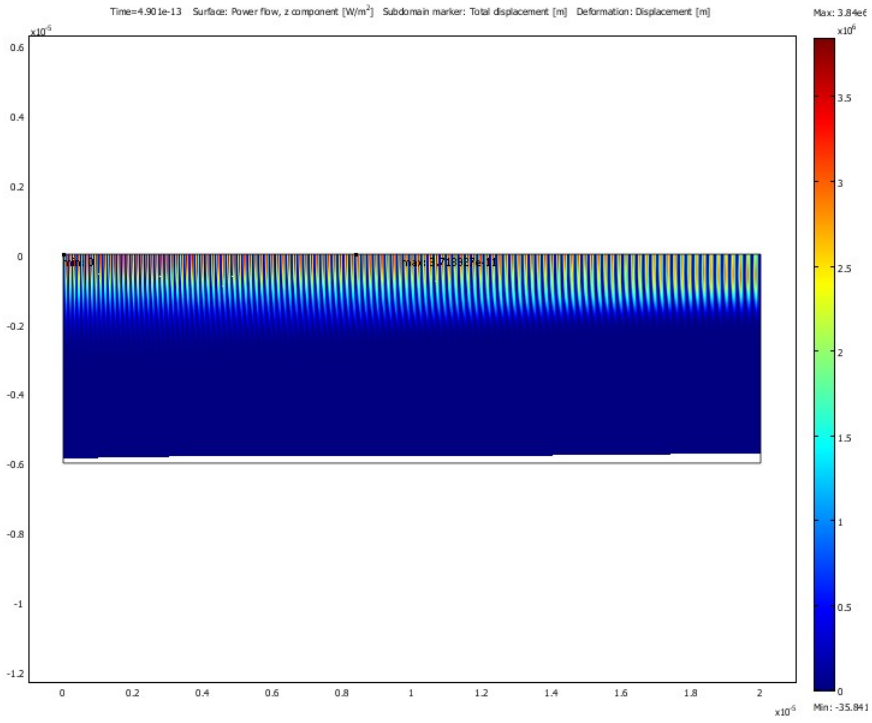

(l) $50\text{x}10^{-14}s$

Figure 4.7: Saturation power flow with change in density for double fiber system.

Figures 4.8 (a)-(l) show the changes in the refractive index and the deformation of the sample with the imposed boundary conditions. Again, the change in the refractive index distribution is similar to those seen previously, however, the correlation between this and the change in the shape of the sample due to densification can be seen through these figures. As the resin is being cured, one can see the corresponding change in density by the deformation shown in each plot. It appears that the smaller the diameter of the cured waveguide is the greater change in density and a greater contraction is seen.

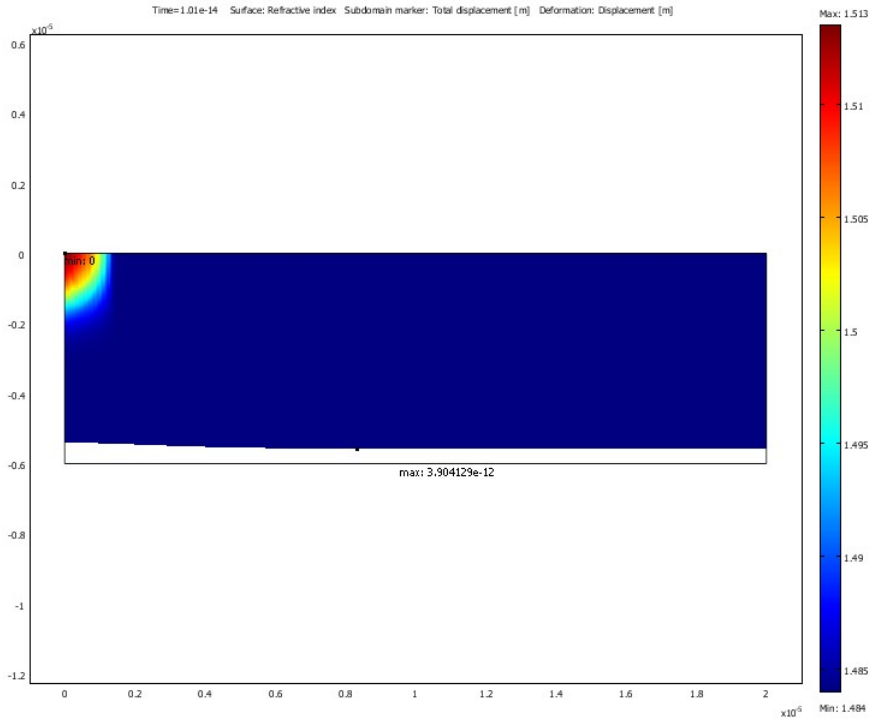

(a) $1\text{x}10^{-14}s$

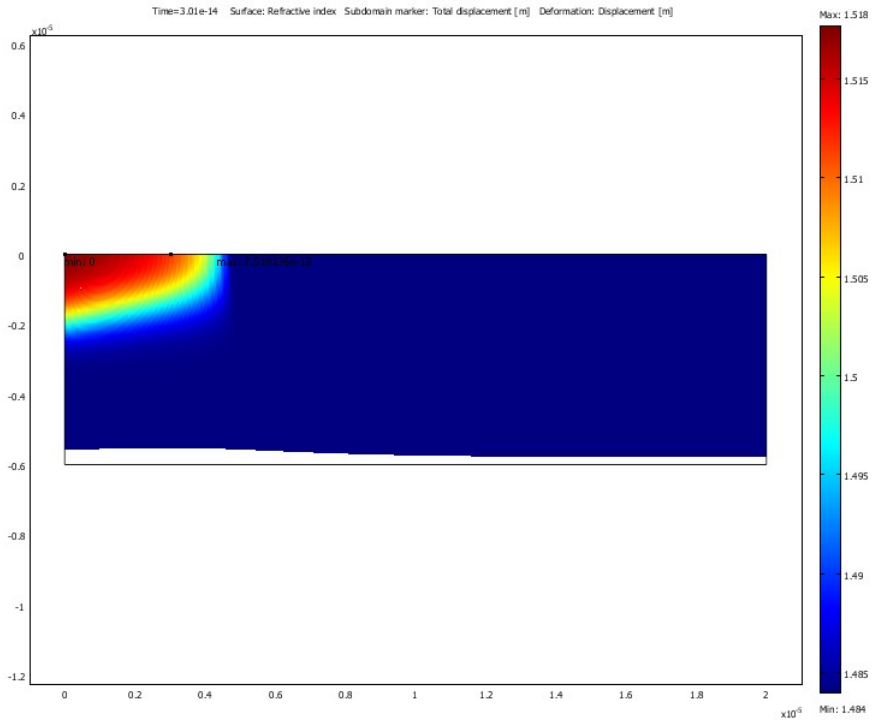

(b) $3\text{x}10^{-14}s$

Figure 4.8: Change in refractive index for saturation Δn with change in density for double fiber system.

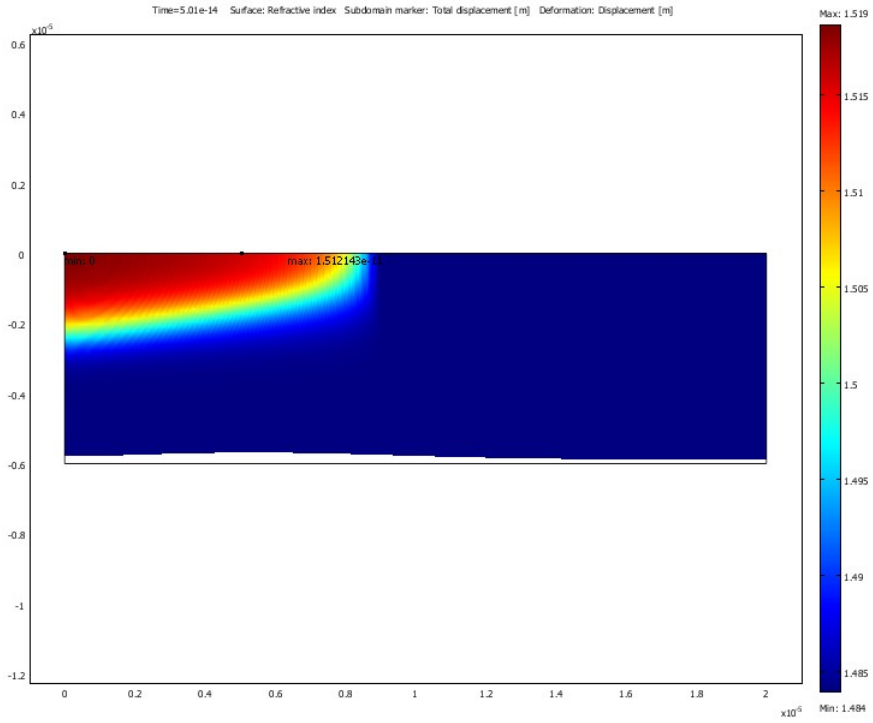

(c) $5\text{x}10^{-14}s$

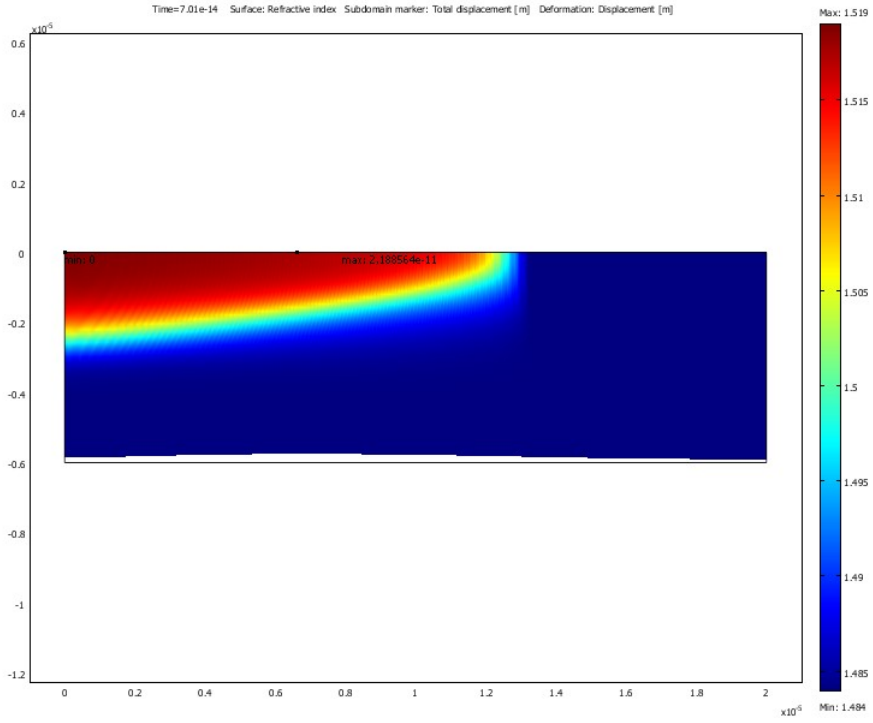

(d) $7\text{x}10^{-14}s$

Figure 4.8: Change in refractive index for saturation Δn with change in density for double fiber system.

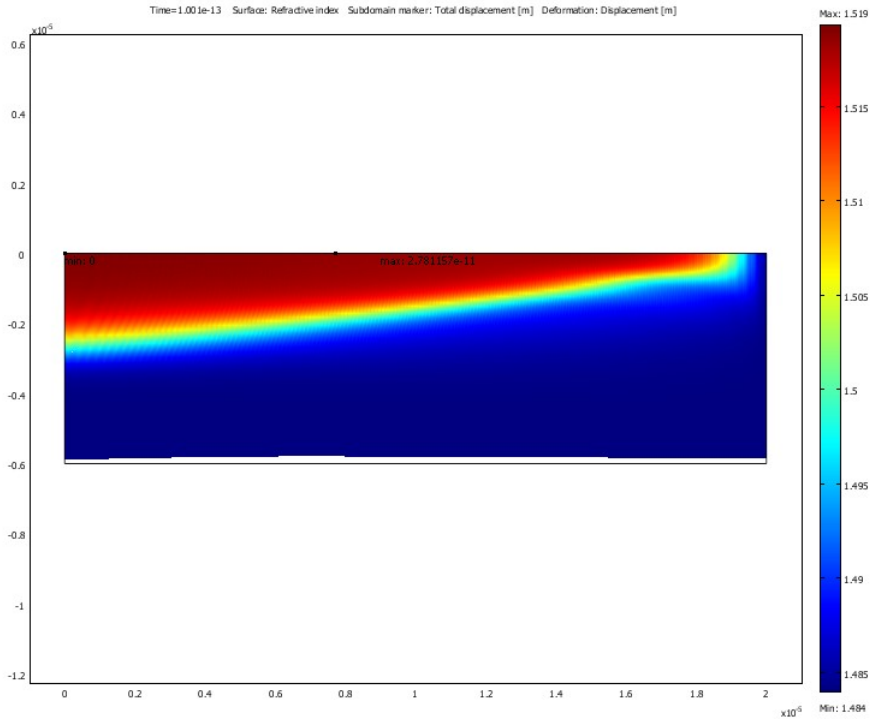

(e) $10\text{x}10^{-14}s$

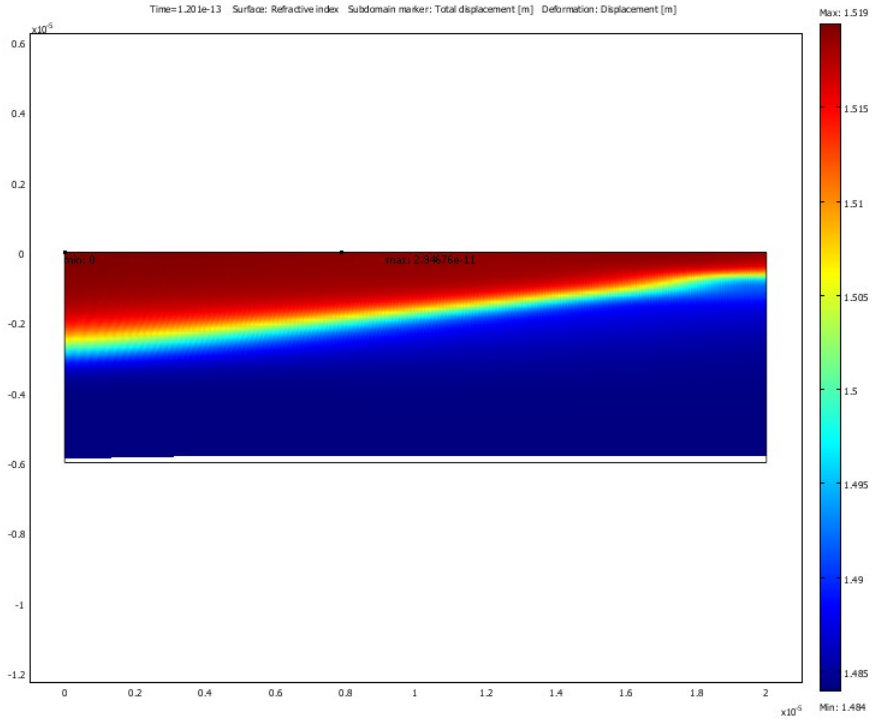

(f) $12\text{x}10^{-14}s$

Figure 4.8: Change in refractive index for saturation Δn with change in density for double fiber system.

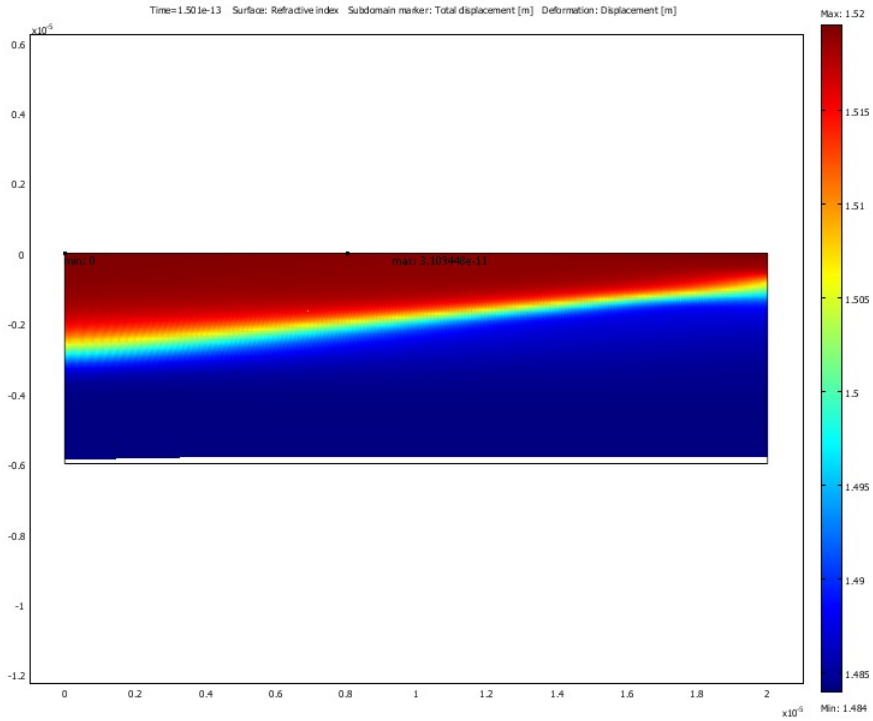

(g) $15\text{x}10^{-14}s$

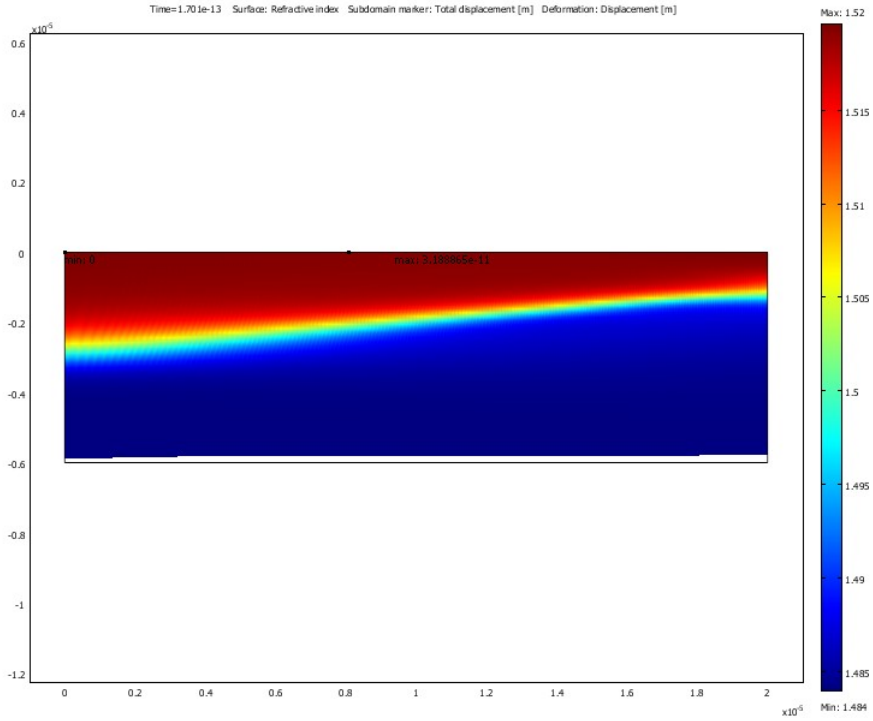

(h) $17\text{x}10^{-14}s$

Figure 4.8: Change in refractive index for saturation Δn with change in density for double fiber system.

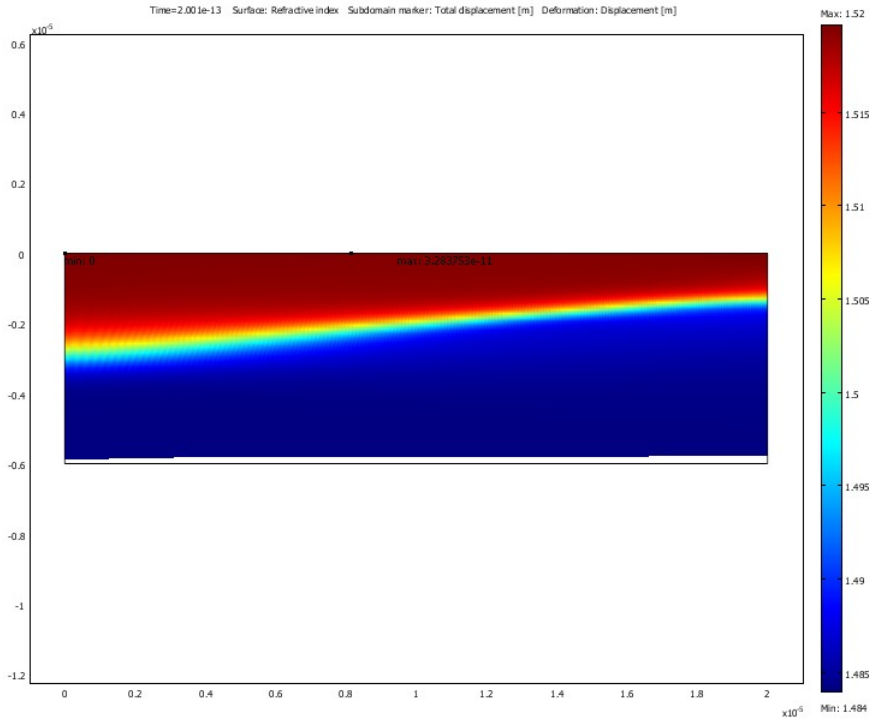

(i) $20\text{x}10^{-14}s$

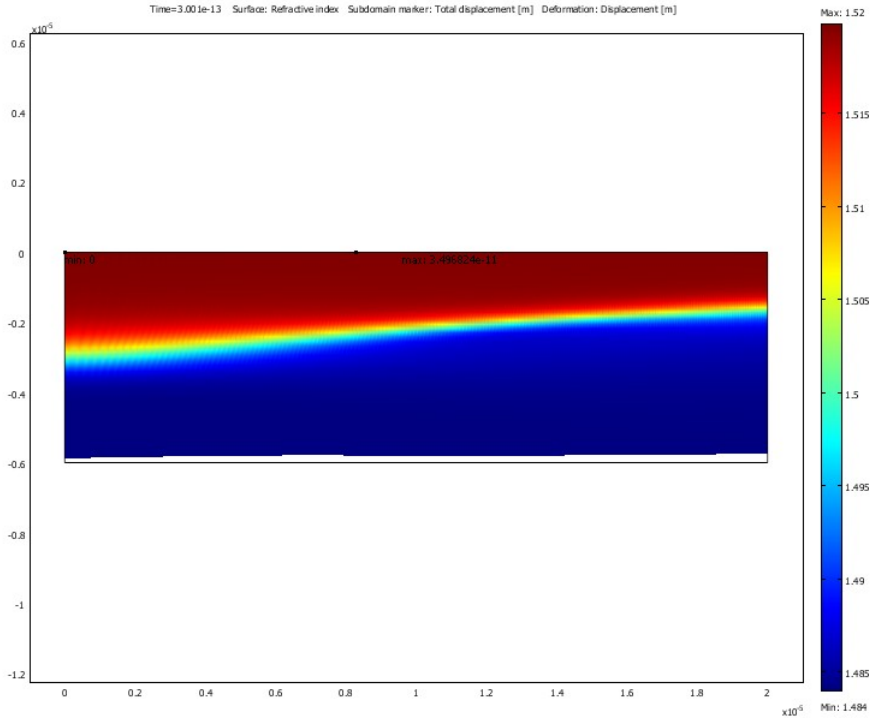

(j) $30\text{x}10^{-14}s$

Figure 4.8: Change in refractive index for saturation Δn with change in density for double fiber system.

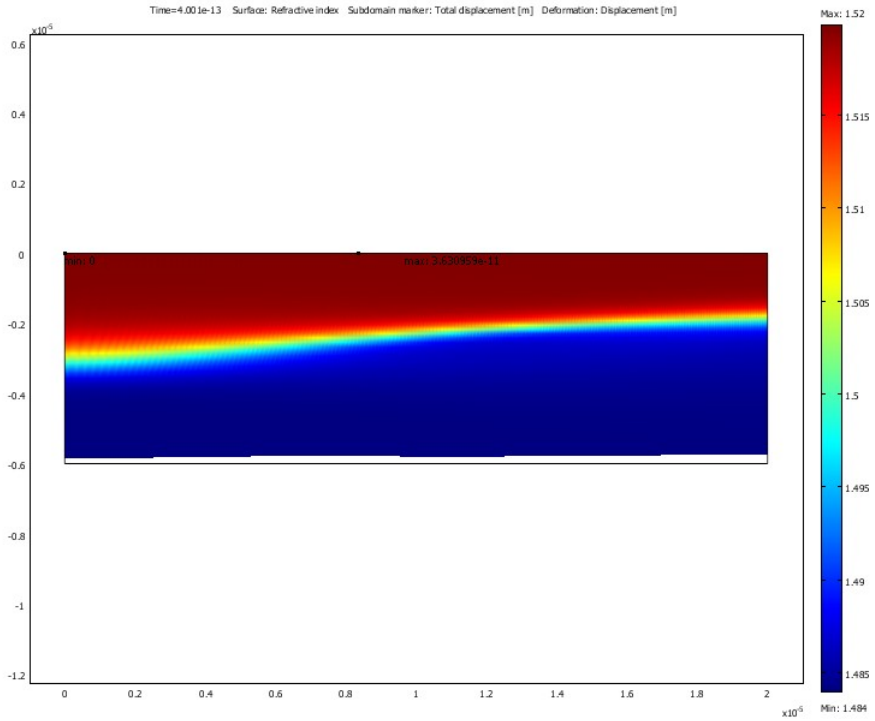

(k) $40\text{x}10^{-14}s$

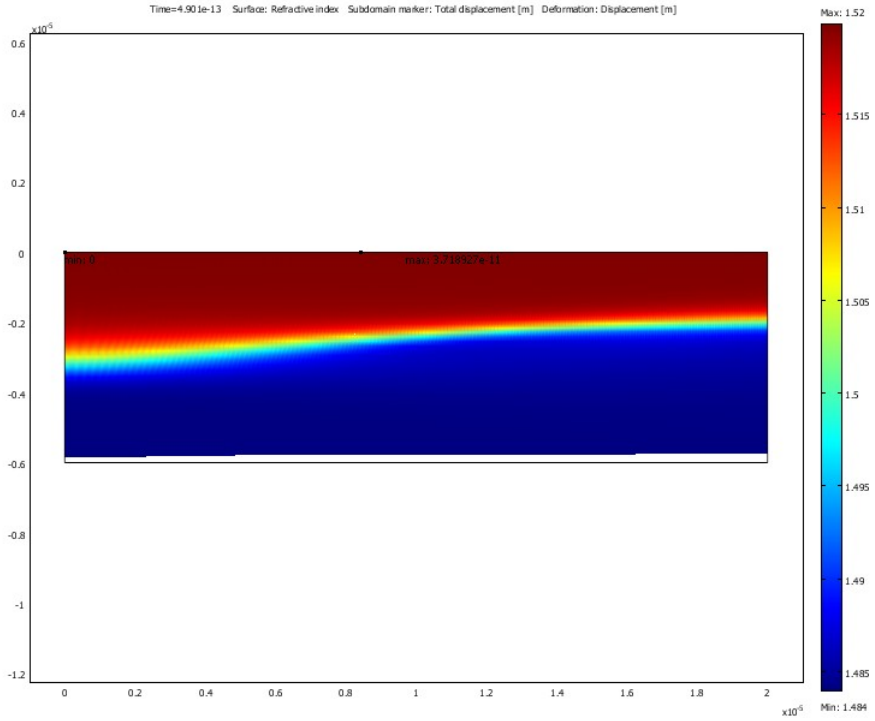

(l) $50\text{x}10^{-14}s$

Figure 4.8: Change in refractive index for saturation Δn with change in density for double fiber system.

4.4 Discussion

There are a number of key aspects of photopolymerization that have been previously experimentally observed: self-focusing/self-trapping, saturation, density change, tapering of the written waveguide and necking in the waveguide. It is these features that we aimed to reproduce in this model. It has been experimentally demonstrated by a number of researchers that the process of photopolymerization exhibits self-focusing and self-trapping behavior [3, 5, 6]. This behavior has been demonstrated in all of the simulations presented in this thesis. In figures 4.1 (j) and (k) for the linear case a focusing effect can be seen; in figures 4.3 (c)-(f) for the saturation model the focusing effect is seen much earlier in the process due to the saturation of the refractive index. This same effect is seen for both the single and double fiber case studies in figures 4.5 (c)-(f) and 4.7 (c)-(f) respectively.

Both the saturation of the index of refraction and the change in density were effects that we incorporated into the model to accurately reflect the interactions occurring in photopolymerization. These effects were demonstrated experimentally by a number of groups [7, 21, 14, 20]. The saturation effects are given in figures 4.4, 4.6 and 4.8 and the density changes for the two different case studies can be seen in figures 4.6 and 4.8. The density changes are highly dependent on the boundary conditions of the model as can be seen in comparing the two case studies. For the first case, with less constraints on the sample, it is apparent that the preferred contraction from densification is along the propagation axis, however, when the movement in the z-direction is constrained there is only contraction in the radial direction. Figure 2.8 demonstrates the confinement of the densification between two fibers experimentally, a similar effect is demonstrated by the results shown in figures 4.7 and 4.8 where the radial deformation follows the polymer growth. Due to tapering effects in this model we do not see quite as symmetric of a result as is found in figure 2.8.

The last two phenomena that have been seen experimentally, but have not been explicitly incorporated into this code are tapering and necking (focusing and refocusing of the wave as it is guided along the cured polymer [10]) effects on the written waveguide. It

was discussed in section 2.2 that it was difficult to get uniform waveguides due to the change in index of refraction and density changes which can cause tapering and necking effects as demonstrated by [18, 10, 22, 20]. This model does not explicitly show the effects of necking, however, if the model geometry were longer it is possible that the tapering effects could lead to necking. The tapering effect has been the most prevalent, which can be seen throughout the simulations in this model. Looking first at the linear case, figures 4.1 (k) and (l) show a tapering effect at rightmost edge of the sample. For the saturation case, tapering is seen throughout the process from figure 4.3 (d) through (l) again on the rightmost side of the sample, which is the same effect seen in both case studies as well. It is possible that with ideal conditions this effect can be eliminated similar to the uniform waveguide formed using a GI-MMF fiber in [5], but the presence of this effect in these simulations further validate this model and its accuracy in computing the photopolymerization process.

Chapter 5

Conclusions and Future Work

5.1 Conclusions

The goal of this work was to create a multi-physics finite element model that can accurately compute the electromagnetic, chemical and mechanical interactions that occur during the process of photopolymerization. This thesis has presented the successful development of the model that can be adapted to various physical situations to compute the reactions of different photosensitive resins undergoing the photopolymerization process.

We have detailed the theoretical background in developing this model including the effects contributed from electromagnetic interactions, the polymer concentration and its dependence on the intensity from the incoming light source, and the mechanical response of the polymerizing resin throughout the curing process. A simplified polymer concentration rate equation was proposed for easier computation that provided a refractive index saturation effect that closely correlates with the saturation seen in experimental studies. The final refractive index change of 2% for the given input values were based off of experimental and material data from [7].

The importance of including the densification effects were also demonstrated by two examples using fiber optics. The first example was a single fiber focused into the resin in which the dominant contraction in the z-direction seen in experimental data was predicted by the finite element simulation. The second example of an epoxy-filled gap

between two fibers demonstrated how the resin contracts when constrained on three of the four boundaries forcing a radial contraction. The results in this case also correlated with previous experimental data with effects similar to those seen by Huang as demonstrated in figure 2.8.

By incorporating all three physical properties occurring in this complex interaction, we have developed a model that defines the photopolymerization process as it applies to self-writing waveguides. By comparison, it was found that this model closely correlates, at least qualitatively, with experimental data from the literature (on an adjusted time scale). The use of a commercially available finite element code also allows for easy access by many users. This thesis has provided an adaptable model that allows for variation in parameters and geometry that can predict the photopolymerization response of different resins under variable loading constraints for extrapolation to many different optical polymerization problems.

5.2 Future Work

Recommended future work on this project would consist of testing this model experimentally using several resins with different refractive indices to see how they react in a laboratory setting for the two case studies computed in sections 4.3.1 and 4.3.2 and comparing the data with model predictions. While single photon absorption has the property that the rate of polymerization is linearly proportional to the intensity, we could also incorporate two photon absorption into the model, where the rate of polymerization is proportional to the square of the intensity. It would also be of interest to include the effects of oxygen on the photopolymerization process into this model as previous research has suggested this could cause changes in the rate of polymerization. Finally it would be interesting to extrapolate our model to include how growth of a polymer sensing element using the SPA and TPA processes would respond under applied strain loading conditions.

Bibliography

[1] E. J. Friebele *et al.* . Optical fiber sensors for spacecraft applications. *Smart Material Structures*, 8:813–838, 1999.

[2] S. J. Frisken. Light-induced optical waveguide uptapers. *Optics Letters*, 18:1035–1037, 1993.

[3] A. S. Kewitsch and A. Yariv. Self-focusing and self-trapping of optical beams upon photopolymerization. *Optics Letters*, 21:24–26, 1996.

[4] S. Shoji and S. Kawata. Optically-induced growth of fiber patterns into a photopolymerizable resin. *Applied Physics Letters*, 75:737–739, 1999.

[5] M. Kagami, T. Yamashita, and H. Ito. Light-induced self-written three-dimensional optical waveguide. *Applied Physics Letters*, 79:1079–1081, 2001.

[6] K. Dorkenoo, O. Crégut, L. Mager, F. Gillot, C. Carre, and A. Fort. Quasi-solitonic behavior of self-written waveguides created by photopolymerization. *Optics Letters*, 27:1782–1784, 2002.

[7] K. Dorkenoo, A. J. van Wonderen, M. Romeo H. Bulou, O. Crégut, and A. Fort. Time-resolved measurement of the refractive index for photopolymerization processes. *Applied Physics Letters*, 83:2474–2476, 2003.

[8] K. D. Belfield and K. J. Shafer. Two-photon photoinitiated polymerization. In Kevin D. Belfield and James V. Crivello, editors, *Photoinitiated Polymerization*, pages 464–481. American Chemical Society, 2003.

[9] S. Maruo, O. Nakamura, and S. Kawata. Three-dimensional microfabrication with two-photon-absorbed photopolymerization. *Optics Letters*, 22:132–134, 1997.

[10] R. Bachelot, C. Ecoffet, D. Deloeil, P. Royer, and D. J. Lougnot. Integration of micrometer-sized polymer elements at the end of optical fibers by free-radical photopolymerization. *Applied Optics*, 40:5860–5871, 2001.

[11] H. Sun, T. Kawakami, Y. Xu, J. Y. Ye, S. Matuso, H. Misawa, M. Miwa, and R. Kaneko. Real three-dimensional microstructures fabricated by photopolymerization of resins through two-photon absorption. *Optics Letters*, 25:1110–1112, 2000.

[12] H. Sun and S. Kawata. Two-photon laser precision microfabrication and its applications to micro-nano devices and systems. *Journal of Lightwave Technology*, 21:624–633, 2003.

[13] I. Wang, M. Bouriau, P. L. Baldeck, C. Martineau, and C. Andraud. Three-dimensional microfabrication by two-photon-initiated polymerization with a low-cost microlaser. *Optics Letters*, 27:1348–1350, 2002.

[14] R. Houbertz. Laser interaction in sol-gel based materials–3-d lithography for photonic applications. *Applied Surface Science*, 247:504–512, 2005.

[15] T. Monro, L. Poladian, and C. Martijn de Sterke. Numerically efficient modal decompostion approach to self-writing process. *J. Opt. Soc. Am. A*, 14:2180–2189, 1997.

[16] T. Monro, L. Poladian, and C. Martijn de Sterke. Analysis of self-written waveguides in photopolymers and photosensitive materials. *Physical Review E*, 57:1104–1113, 1998.

[17] M. Hocine, R. Bachelot, C. Ecoffet, N. Fressengeas, P. Royer, and G. Kugel. End-of-fiber polymer tip: manufacturing and modeling. *Synthetic Metals*, 127:313–318, 2002.

[18] M. Hocine, N. Fressengeas, G. Kugel, C. Carré, D. J. Lougnot, R. Bachelot, and

P. Royer. Modeling the growth of a polymer microtip on an optical fiber end. *J. Opt. Soc. Am. B*, 23:611–620, 2006.

[19] C. Lin, I. Wang, B. Dollet, and P. Baldeck. Velocimetry microsensors driven by linearly polarized optical tweezers. *Optics Letters*, 31:329–331, 2006.

[20] H. Huang. Fabrication and evaluation of hybrid silica/polymer optical fiber sensors for large strain applications. volume 6529 of *Proc. SPIE*, pages 6529–32, 2007.

[21] U. Streppel, P. Dannberg, C. W achter, A. Br auer, and R. Kowarschik. Formation of micro-optical structures by self-writing processes in photosensitive polymers. *Applied Optics*, 42:3570–3579, 2003.

[22] W. Haske *et al.* . 65 nm feature sizes using visible wavelength 3-d multiphoton lithography. *Optics Express*, 15:3426–3436, 2007.